NASA CONTRACTOR REPORT

MODELING OF THREE-DIMENSIONAL MIXING AND REACTING DUCTED FLOWS

S. W. Zelazny, A. J. Baker,
and W. L. Rushmore

Prepared by
BELL AEROSPACE COMPANY
Buffalo, N. Y. 14240
for Langley Research Center

NATIONAL AERONAUTICS AND SPACE ADMINISTRATION • WASHINGTON, D. C. • APRIL 1976

1. Report No.	2. Government Accession No.	3. Recipient's Catalog No.
NASA CR-2661		

4. Title and Subtitle
Modeling of Three-Dimensional Mixing and Reacting Ducted Flows

5. Report Date
April 1976

6. Performing Organization Code

7. Author(s)
S.W. Zelazny, A.J. Baker, W.L. Rushmore

8. Performing Organization Report No.
9225-953002

9. Performing Organization Name and Address
Bell Aerospace Company, Textron Division
P.O. Box One
Buffalo, New York 14240

10. Work Unit No.

11. Contract or Grant No.
NAS1-13165

12. Sponsoring Agency Name and Address
National Aeronautics and Space Administration
Washington, D.C. 20546

13. Type of Report and Period Covered
Contractor Report

14. Sponsoring Agency Code

15. Supplementary Notes
Langley technical monitor: James E. Eggers
Final report.

16. Abstract

A computer code, based upon a finite element solution algorithm, was developed to solve the governing equations for three-dimensional, reacting boundary region, and constant area ducted flow fields. Effective diffusion coefficients are employed to allow analyses of turbulent, transitional or laminar flows. The code was used to investigate mixing and reacting hydrogen jets injected from multiple orifices, transverse and parallel to a supersonic air stream. Computational results provide a three-dimensional description of velocity, temperature, and species-concentration fields downstream of injection.

Experimental data for eight cases covering different injection conditions and geometries were modeled using mixing length theory (MLT). These results were used as a baseline for examining the relative merits of other mixing models. Calculations were made using a two-equation turbulence model (k+d) and comparisons were made between experiment and mixing length theory predictions. The k+d model shows only a slight improvement in predictive capability over MLT. Results of an examination of the effect of tensorial transport coefficients on mass and momentum field distribution are also presented. Solutions demonstrating the ability of the code to model ducted flows and parallel strut injection are presented and discussed.

17. Key Words (Selected by Author(s))	18. Distribution Statement
Three-Dimensional Flow Turbulent, Reacting Ducted Finite Element Method Numerical Solution	Unclassified - Unlimited

19. Security Classif. (of this report)	20. Security Classif. (of this page)	21. No. of Pages	22. Price*
Unclassified	Unclassified	100	$4.75

For sale by the National Technical Information Service, Springfield, Virginia 22161

TABLE OF CONTENTS

TABLE OF CONTENTS (Contd)

ILLUSTRATIONS

TABLES

MODELING OF THREE-DIMENSIONAL MIXING AND REACTING DUCTED FLOWS

By

S. W. Zelazny, A. J. Baker and W. L. Rushmore

Textron's Bell Aerospace

SUMMARY

A computer code, based upon a finite element solution algorithm, was developed to solve the governing equations for three-dimensional, reacting boundary region, and constant area ducted flow fields. Effective diffusion coefficients are employed to allow analyses of turbulent, transitional or laminar flows. The code was used to investigate mixing and reacting hydrogen jets injected from multiple orifices, transverse and parallel to a supersonic air stream. Computational results provide a three-dimensional description of velocity, temperature, and species-concentration fields downstream of injection.

Experimental data for eight cases covering different injection conditions and geometries were modeled using mixing length theory (MLT). These results were used as a baseline for examining the relative merits of other mixing models. Calculations were made using a two-equation turbulence model (k+d) and comparisons were made between experiment and mixing length theory predictions. The k+d model shows only a slight improvement in predictive capability over MLT. Results of an examination of the effect of tensorial transport coefficients on mass and momentum field distribution are also presented. Solutions demonstrating the ability of the code to model ducted flows and parallel strut injection are presented and discussed.

INTRODUCTION

The hydrogen-fueled scramjet engine is a prominent candidate for propulsion of advanced hypersonic cruise vehicles. (See for example, Becker and Kirkham (ref. 1) and Bushnell (ref. 2).) An airframe-integrated underbody engine configuration (figs. 1(a) and (b)) has been suggested (ref. 3), and design considerations are discussed by Henry and Anderson (ref. 4). Many alternative scramjet designs have been proposed by the U.S. Air Force, the U.S. Navy, and NASA. In all cases, however, fuel introduction typically consists of rows of circular, choked-flow fuel injector orifices mounted flush and normal to the combustor wall or in fins spanning the combustor inlet (see fig. 1(c).) The various proposed

component designs have largely emerged from laboratory experimentation wherein empirical relations have established a preliminary configuration. Detailed experimental parametric evaluations are then utilized to optimize design configuration.

The ability to analytically predict turbulent, mixing, and reacting three-dimensional flows, and hence avoid the more costly exclusively experimental approach, has been the long-range goal of rocket and ramjet designers for more than a decade. Three very difficult problems must yield to solution to attain this goal. First, a computational technique for solving the appropriate three-dimensional flow field with a predominant flow direction is required. Second, proper turbulent diffusion models must be selected or developed, since the accuracy of the predictive calculation is strictly dependent upon the adequacy of these models for combined laminar and turbulent diffusion of mass, momentum, and energy. Finally, detailed baseline data characterizing the flow phenomena over a reasonably wide range of flow parameters must be obtained to confirm the validity of flow theoretical modeling.

The objectives of this investigation were to - (1) use the COMOC code developed in earlier studies (refs. 5, 6, and 7) to investigate the accuracy of existing mixing models in characterizing scramjet combustor flow fields, (2) develop a new mixing model if required, and (3) extend the applicability of the COMOC code to consider constant area ducted flow fields. Although this investigation deals primarily with scramjet oriented problems, it is important to note that the analysis may be employed in other problem areas characterized by three-dimensional reacting flows, e.g., chemical lasers, smokestack emission and gas turbine combustior chambers.

Governing conservation equations, effective diffusion coefficient models, and methods used to compute reacting flows and pressure variations along the duct are presented in the METHOD OF ANALYSIS section. Details on the structure and methodology of COMOC are then presented in FINITE ELEMENT SOLUTION ALGORITHM. Current combustor design concepts (ref. 4) for scramjet engines employ fuel injection both from transverse wall injectors and from internal struts containing both parallel and transverse injection orifices. Experimental data characterizing these types of conditions have been reported in references 8, 9, 10, 11 and were modeled using the COMOC computer code. A brief description of these experimental studies and the details of the analytical modeling of this data using COMOC are presented in the NUMERICAL RESULTS section. Key results and recommendations for future efforts are presented in CONCLUDING REMARKS. Finally, an Appendix is included where the required input and output control for the

COMOC code is described in a card by card sequence.

NOMENCLATURE

a	boundary-condition coefficient
A	species; area; Van Driest Damping factor
b	coefficient
B	species
c	coefficient
c_p	specific heat
c_ε	ratio of $\varepsilon_{13}/\varepsilon_{12}$
C	species
C_f	skin friction
C_k	mixing length constant, Eq. (13)
d	differential; orifice diameter; turbulence dissipation, Eq. (16)
f	function of known argument
g	function of known argument
h	static enthalpy; duct height
H	stagnation enthalpy; hydrogen
i	index
$\hat{i},\hat{j},\hat{k}$	unit vectors of rectangular Cartesian coordinate system
k	thermal conductivity; turbulence kinetic energy
K	generalized diffusion coefficient; equilibrium constant
ℓ	differential operator; number; mixing length

L	characteristic length; differential operator
m	number
M	Mach number; number of finite elements
n	unit normal vector; number; nodes per element; dimensionality
N	nitrogen; composition matrix
N_d	dissipation number = $\varepsilon_d/\varepsilon$
N_k	turbulence kinetic energy number = $\varepsilon_k/\varepsilon$
N_{Le}	Lewis number
N_{Pr}	Prandtl number
N_{Re}	Reynolds number
N_{Sc}	Schmidt number
O	oxygen
p	pressure
q	generalized dependent variable
q_r	dynamic pressure ratio
Q	generalized discretized dependent variable
R	domain of elliptic operator; universal gas constant
s	injector spacing
S	mass source term; finite element assembly operator
T	temperature
u_i	velocity component in ith direction
u,U	velocity
$\overline{u_i' u_j'}$	turbulent shear stress component

u^*	friction velocity, $\sqrt{\tau_w/\rho}$
W	molecular weight
x_i	rectangular Cartesian coordinate system
x_2^*	$= u_2^* x_2/\nu$
X	species mole fraction
Y	species mass fraction
α	species identification
β	pressure gradient parameter; elemental species
γ	ratio of specific heats
∂R	closure of elliptically coupled solution domain
δ	boundary-layer thickness
Δ	increment
ε	kinematic eddy viscosity
ε_{12}	kinematic eddy viscosity resulting from $\overline{u_1' u_2'}$
ε_{13}	kinematic eddy viscosity resulting from $\overline{u_1' u_3'}$
ε_d	turbulence dissipation diffusion coefficient
ε_k	turbulence kinetic energy diffusion coefficient
η	mixing efficiency
κ	coefficient
λ	multiplier; turbulence sublayer constant
μ	viscosity
ρ	density
σ	integral kernel

τ integral kernel; wall shear

ϕ equivalence ratio, $\dfrac{(\rho u_1)_{jet}}{0.034(\rho u_1)_{air}}$

Φ functional

χ domain of initial-value operator

ω turbulence damping factor

Ω global solution domain

Superscripts:

e effective value

T matrix transpose

α species identification

$\hat{}$ unit vector

* approximate solution

Subscripts:

∞ global reference condition

e local reference condition

i,j,k tensor indices

m mth subdomain

o initial

t stagnation or total

T turbulent

Notation:

{ } column matrix

[ ] square matrix

$\cup$	union
$\cap$	intersection
$\sum$	summation
ϵ	belongs to

METHOD OF ANALYSIS

Many researchers are now giving attention to numerical solution of three-dimensional parabolic and/or boundary-region flow fields. Most procedures employ a finite difference solution algorithm for variously combined forms of the continuity, momentum and energy equations. Note that the three-dimensional boundary-layer equations result from this parabolic set for flow fields wherein diffusion in one direction only is important and the corresponding pressure gradient is negligible. Several researchers have obtained solutions for the three-dimensional boundary-region flow of single-species fluids. Pal and Rubin (ref. 12) employ asymptotic expansions of the flow variables for laminar incompressible flow after transformation to modified streamfunction and vorticity. Results of extending the theory to a compressible perfect fluid in physical variables are reported by Cresci et al. (ref. 13), who used an extension of the numerical technique common to boundary-layer solutions. Extension to handle streamwise pressure gradients and refinement of the overall method are reported by Rubin and Lin (ref. 14). Caretto et al. (ref. 15) present a finite difference algorithm for solution of three-dimensional boundary-region flows with extension to the "parabolic" Navier-Stokes equations. The results of computations for transitional internal flows in rectangular ducts are presented by Curr et al. (ref. 16). Refinement of the overall procedure with particular attention to solution of the parabolic Navier-Stokes equations is given by Patankar and Spalding (ref. 17). The key feature of their theory is a procedure for splitting the pressure field computation such that a two-dimensional boundary-value problem results for pressure in the transverse plane coupled to an assumed uniform streamwise pressure gradient computed from global continuity. The latter step is similar to methods employed for computations in two-dimensional hydrodynamics (ref. 18).

Characterization of an n-species, three-dimensional boundary-region or parabolic flow field requires solution of (n-1) species-continuity equations in addition to those previously mentioned. Caretto (ref. 15) and Patankar and Spalding (ref. 17) include results of a finite-difference solution of heat, mass, and momentum transfer in three-dimensional parabolic flows. Baker (ref. 19)

presents a finite element solution algorithm for multiple-species diffusion in supersonic, three-dimensional boundary-region flow. However, no general three-dimensional solution algorithm has been published which considers mixing and reacting three-dimensional confined flows.

The system of partial differential equations governing such three-dimensional, confined unidirectional flows of a compressible, reacting fluid is obtained as an approximation to the full three-dimensional Navier-Stokes equations. This approximation, referred to as the "parabolic Navier-Stokes equations," describes steady, confined three-dimensional flows wherein (1) a predominant flow direction is uniformly discernible; (2) diffusion processes in the predominant flow direction are negligible compared with convection; and (3) no disturbances are propagated upstream, e.g., recirculation is not considered.

Presented below and in FINITE-ELEMENT SOLUTION ALGORITHM is a description of the governing equations which are solved in the COMOC computer code. A number of key points should be noted:

(1) Solution of the three-dimensional parabolic Navier-Stokes equations is obtained wherein the streamwise pressure variation is computed using the approach presented in the subsection Pressure Variations In Ducted Flows. This version of the computer code is referred to as COMOC-3DPNS.

(2) If a pressure distribution is known a priori then that section of the code which computes streamwise pressure variations may be bypassed. The resulting equations are herein referred to as the three-dimensional boundary region equations and represent a subset of the 3DPNS system. This variant of the code is referred to as COMOC-3DBR.

(3) The solution algorithm embodied in both the 3DBR and 3DPNS codes is limited to constant area flow domains. To consider variable area flows would require either a coordinate transformation, e.g., streamfunction or a method which would add finite elements to the outer edges of the computational domain. Including this feature into COMOC was considered beyond the scope of this investigation.

The velocity vector lying on a three-dimensional Euclidean space spanned by a rectangular Cartesian coordinate system x_i is identified as

$$u_i \equiv u_1\hat{i} + u_2\hat{j} + u_3\hat{k} \qquad (1)$$

For development of the governing equation system, assume that $\hat{i}$ is parallel to the predominant flow direction. Identify the two-dimensional vector differential operator

$$( )_{,k} \equiv \hat{j}( )_{,2} + \hat{k}( )_{,3} \tag{2}$$

where the comma identifies the gradient operator. In Cartesian tensor notation with summation over 2 and 3 for repeated Latin subscripts, the parabolic Navier-Stokes equation system for a multiple-species, compressible, reacting flow takes the form

$$0 = (\rho u_i)_{,i} + (\rho u_1)_{,1} \tag{3}$$

$$\rho u_1 Y^{\alpha}_{,1} = \left(\frac{\mu^e}{N^e_{Sc} N_{Re}} Y^{\alpha}_{,k} \right)_{,k} - \rho u_k Y^{\alpha}_{,k} + S^{\alpha} \tag{4}$$

$$\rho u_1 u_{j,1} = \left(\frac{\mu^e}{N_{Re}} u_{j,k} \right)_{,k} - \rho u_k u_{j,k} - p_{,j} \tag{5}$$

$$\rho u_1 H_{,1} = \left(\frac{\mu^e}{N^e_{Re} N_{Pr}} H_{,k} \right)_{,k} - \rho u_k H_{,k} - \frac{U^2_{\infty}}{H_{\infty}} \left[\frac{1-N_{Pr}}{N_{Pr}} \frac{\mu^e}{2N_{Re}} \left(u_j u_j \right)_{,k} \right]_{,k}$$

$$- \left(\frac{N_{Sc} - N_{Pr}}{N_{Sc} N_{Pr}} \frac{\mu^e}{N_{Re}} \sum h^{\alpha} Y^{\alpha}_{,k} \right)_{,k} \tag{6}$$

The variables appearing in equations (3) to (6) are non-dimensionalized with respect to μ_{∞}, ρ_{∞}, U_{∞}, H_{∞}, and a length constant L, and have their usual interpretation in fluid mechanics. The Reynolds number N_{Re}, effective Prandtl number N^e_{Pr}, and effective Schmidt number N^e_{Sc} are defined for a combination of laminar and turbulent contributions as,

$$N_{Re} = \frac{\mu_\infty \rho_\infty L}{U_\infty} \tag{7a}$$

$$\frac{\mu^e}{N^e_{Pr}} \equiv \frac{\mu}{N_{Pr}} + \frac{\rho\varepsilon}{(N_{Pr})_T} \tag{7b}$$

$$\frac{\mu^e}{N^e_{Sc}} = \frac{\mu}{N_{Sc}} + \frac{\rho\varepsilon}{(N_{Sc})_T} \tag{7c}$$

In equation (7), μ is the laminar viscosity, ε is the kinematic eddy viscosity, and the subscript T denotes a turbulent reference parameter. The stagnation enthalpy is defined in terms of species static enthalpies as

$$H \equiv \sum_\alpha h^\alpha Y^\alpha + \frac{1}{2} u_k^2 \tag{8}$$

The static enthalpy includes the heat of formation h^α_o of the species in its definition as

$$h^\alpha \equiv \int_{T_o}^{T} c_p^\alpha \, dT + h_o^\alpha \tag{9}$$

An equation of state is required to close the system. Assuming perfect-gas behavior for each species, from Dalton's law,

$$p = \rho R T \sum_\alpha \frac{Y^\alpha}{W^\alpha} \tag{10}$$

where R is the universal gas constant and W^α is the molecular weight of the αth species.

Turbulence Models

Closure of the governing equations requires introducing relationships to define effective viscosity, and turbulent Prandtl and Schmidt numbers. The momentum diffusion (shear stress) in the x_1 direction may be expressed as

$$\left((\mu + \rho\varepsilon_{12})u_{1,2}\right)_{,2} + \left((\mu + \rho\varepsilon_{13})u_{1,3}\right)_{,3} \tag{11}$$

where the boundary layer approximation has been used to justify dropping $(\mu + \rho\varepsilon_{11})u_{1,1})_{,1}$. Three different approaches to modeling ε_{12} and ε_{13} were considered, (1) simple mixing length theory (MLT) where it was assumed $\varepsilon_{12} = \varepsilon_{13} = \varepsilon$, (2) MLT where $\varepsilon_{12} = \varepsilon$ and $\varepsilon_{13} = C_\varepsilon\varepsilon$ where C_ε is a constant, and (3) the two-equation turbulence model reported by Launder and Spalding (ref. 20). For MLT the kinematic eddy viscosity is given by

$$\varepsilon = \ell^2|u_{1,2}| \tag{12}$$

The mixing length is defined as

$$\ell \equiv \begin{cases} C_k x_2 \omega & (0 \leq x_2 \leq \lambda\delta/C_k) \\ \lambda\delta\omega & (x_2 > \lambda\delta/C_k) \end{cases} \tag{13}$$

where

$C_k = 0.435$

$\lambda = 0.09$

δ = boundary-layer thickness

x_2 = coordinate normal to wall

The Van Driest damping coefficient is

$$\omega \equiv 1 - \exp\left(-\frac{x_2^*}{A}\right)$$

where

$$x_2^* \equiv \frac{u^* x_2}{\nu}$$

u^* = friction velocity, $\sqrt{\tau/\rho}$

τ = skin friction

ρ = density at wall

ν = kinematic viscosity

$A \equiv 23.5$

The second type of model considered wherein $\varepsilon_{12} \neq \varepsilon_{13}$ is of interest since the effects of cross flow variations in u_1 on flow field development may be examined. Of particular interest is the case where $\varepsilon_{13} \neq \varepsilon_{12}$ since here the effect of modeling each component of the turbulent shear stress as a tensorial quantity may be examined.

The final model considered, i.e., a two-equation turbulence model, ref. 20, p. 97, requires defining the scalar kinematic viscosity, ε, in terms of a characteristic velocity and length scales as

$$\varepsilon = C_\tau k^{1/2} \ell_d \tag{14}$$

where the velocity scale is related to the turbulence kinetic energy k given by

$$k = \frac{1}{2}\left[\overline{u_1'^2} + \overline{u_2'^2} + \overline{u_3'^2}\right] \tag{15}$$

and the turbulent length scale, ℓ_d, is related algebraically to the turbulent dissipation, d, through equation (16).

$$\ell_d = k^{3/2}/d \tag{16}$$

The turbulent kinetic energy and dissipation are computed from solution of equations (17) and (18)

$$\rho u_1 k_{,1} = \left(\frac{\rho\varepsilon}{N_k N_{Re}} k_{,i}\right)_{,i} - \rho u_i k_{,i} + \frac{\rho\varepsilon}{N_{Re}} (u_{1,2})^2 - \rho d \tag{17}$$

$$\rho u_1 d_{,1} = \left(\frac{\rho\varepsilon}{N_d N_{Re}} d_{,i}\right)_{,i} - \rho u_i d_{,i} + \frac{C_1^d d}{N_{Re} k} (u_{1,2})^2 - C_2^d \rho \frac{d^2}{k} \tag{18}$$

where it was assumed that the production of turbulent kinetic energy is due to the $\overline{u_1' u_2'}$ component of shear stress, i.e., $u_{1,3}$ is negligible with respect to $u_{1,2}$. This assumption is reasonable

for the flow regions examined herein using the k and d model. The constants used in equations (14), (17), and (18) as suggested in ref. 20 are as follows: $C_\tau = 0.09$, $C_1^d = 1.44$, $C_2^d = 1.92$, $N_k = 1.0$, and $N_d = 1.3$.

In addition to having to introduce an expression(s) to compute the effective kinematic viscosity, it is also necessary to define the turbulent Prandtl and Schmidt numbers. In this investigation it was assumed that mass and thermal energy, both scalar quantities, diffuse at the same rate, hence the turbulent Lewis number, $(N_{Le})_T$, is equal to unity. The validity of this assumption is supported by numerous experimental studies and is generally used in most turbulence modeling efforts, e.g., see ref. 21. This assumption requires $(N_{Pr})_T = (N_{Sc})_T$ since $(N_{Le})_T = (N_{Pr}/N_{Sc})_T$, hence the only remaining information required to complete the description of the turbulence parameters is $(N_{Pr})_T$. Generally, it is sufficient to define $(N_{Pr})_T$ equal to a constant in the range from 0.7 to 1.0. The results shown in NUMERICAL RESULTS were obtained with $(N_{Pr})_T = 0.9$, 0.7 or using an empirical correlation.

Pressure Variations in Ducted Flows

For internal flows, characterized by boundary-layer thicknesses which are small in comparison with the overall internal duct dimension, the pressure distribution can be accurately approximated by inviscid flow solutions. However, in the alternate case where the flow is confined in a duct whose lateral dimension is not large with respect to the boundary-layer thickness, this approach is invalid. Here, boundary-layer development directly influences the pressure distribution within the duct, and an axial pressure gradient is induced by viscous effects. For these flows; a quasi-one-dimensional integral treatment of equations (3) and (5) has been suggested (refs. 17 and 21), wherein for steady flows, equations (3) and (5) are integrated across the duct transverse dimensions to obtain an equivalent expression written on mass-averaged dependent variables defined by

$$Q \equiv \frac{1}{\dot{m}A} \int_{A(x_1)} \rho u_1 q \, d\tau \tag{19}$$

In equation (19), $A(x_1)$ is the duct area, which may be a function of axial location* x_1; $\dot{m}$ is the mass flow rate

$$\dot{m} \equiv \rho u_1 A \tag{20}$$

and q represents a generalized dependent variable which may be selectively streamwise velocity u_1, static temperature T, or density ρ. Taking the logarithmic differential of equation (20) gives

$$\frac{dA}{A} = \frac{d\dot{m}}{\dot{m}} - \frac{du_1}{u_1} - \frac{d\rho}{\rho} \tag{21}$$

The integral momentum equation (eq. (5)) implies

$$Adp + Fdx_1 + u_1 d\dot{m} + \dot{m} du_1 = 0 \tag{22}$$

where F is the retarding force per unit length of duct exerted by viscous interaction of the confined flow with the wall. The equation of state for a perfect fluid of constant molecular weight may be logarithmically differentiated to yield

$$\frac{d\rho}{\rho} = \frac{dp}{p} - \frac{dT}{T} \tag{23}$$

Combining equations (19) to (23) yields an explicit relation for axial pressure gradient as

$$p_{,1} = \frac{-\frac{F}{A} - \frac{2u_1}{A}\dot{m}_{,1} + \frac{\dot{m}u}{A^2}A_{,1} - \frac{\dot{m}u_1}{AT}T_{,1}}{1 - \frac{\dot{m}u_1}{Ap}} \tag{24}$$

*Area must be constant in any application of COMOC-3DPNS since the solution algorithm for the governing equations (3,4,5 and 6) is limited to this condition. However, the solution algorithm for streamwise pressure gradient has been formulated such that variable areas may be considered once the constraint on Eqs. (3), (4), (5), and (6) is removed.

If an initial pressure level and the detailed flow field at a given station are known, equation (24) can be evaluated and integrated to yield downstream pressure levels. To achieve this, the friction force per unit duct length is related to the wall shear stress τ_w as

$$F = \int_S \tau_w dL \tag{25}$$

where the line integration is performed about the boundary of the computational domain, e.g., about symmetry planes $\tau_w = 0$, whereas along walls τ_w is finite. For flow fields which may be characterized by two parallel walls separated by distance h and two symmetry planes separated by distance h, the frictional force per unit area would be given by

$$\frac{F}{A} = \left[\int_U \tau_w dL + \int_L \tau_w dL\right]/(Lh) \tag{26}$$

where the integrations are performed over the upper (U) and lower (L) walls and where τ_w is evaluated as a function of the local flow properties near the wall (ref. 21) from the expression

$$\tau_w = C_k^2 \rho \tilde{u}_1^2 \left(R_*^{-1} - 0.156R_*^{0.45} + 0.08723R_*^{0.3} + 0.0371R_*^{-0.18}\right)F_p \tag{27a}$$

where C_k is the same constant (von Karman's) used in defining the mixing length in MLT, $R_* = k^2R$ and $R = \tilde{u}_1\tilde{x}_2/\nu$. The symbol (~) refers to parameters evaluated in the constant shear stress region hence the length scale, $\tilde{x}_2$ represents the distance above the wall where convective flow effects are negligible. Similarly, $\tilde{u}_1$ represents the x_1 velocity component at the edge of the constant shear stress region. The effect of pressure gradient on shear stress is included in equation (27a) by the parameter F_p given by

$$F_p = \left[1 - \frac{4F_*R_*}{(12.8^{2.5} + R_*^{2.5})^{0.4}}\right]^{1.6} ; \quad F_* = \frac{\tilde{x}_2}{\rho\tilde{u}_1^2} p_{,1} \tag{27b}$$

Calculation of the change in mass flow rate with respect to axial distance requires a computational distinction between the actual mass flow $\dot{m}^r$ and the computed mass flow $\dot{m}^f$. The difference between $\dot{m}^r$ and $\dot{m}^f$ provides an estimate of the pressure and pressure gradient to maintain conservation of mass. The rate of change of mass flow with respect to x_1 is defined as

$$\dot{m}_{,1} = \frac{\Delta\dot{m}}{\Delta x_1} \tag{28}$$

where

$$\Delta\dot{m} = \Delta\dot{m}^f - \Delta\dot{m}^r \tag{29}$$

and

$$\Delta\dot{m}^r = \dot{m}^r(x_1 + \Delta x_1) - \dot{m}^r(x_1) \tag{30a}$$

$$\Delta\dot{m}^f = \dot{m}^r(x_1) - \dot{m}^f(x_1) \tag{30b}$$

$$\Delta x_1 = (x_1)_{new} - (x_1)_{old} \tag{31}$$

In equation (30a), $\Delta\dot{m}^r$ represents the mass flow increment which results from the mass addition, whereas $\Delta\dot{m}^f$ (equation (30b)) represents the mass flow error obtained at the upstream station x_1. Examination of equations (24) and (28) to (30) shows that use of equation (28) will always provide a pressure gradient which tends to make the computed and actual mass flow discrepancy decrease and hence model the physical flow.

Reacting Flows

There are two approximate methods which may be effectively used to describe reacting hydrogen-oxygen-air systems. In the first case, assume that prototype scramjet combustors are adequately described by equilibrium combustion. The following reactions are operative:

$$2H + O \rightleftarrows H_2O$$

$$2H \rightleftarrows H_2$$

$$2O \rightleftarrows O_2$$

$$H + O \rightleftarrows OH$$

$$N_2 + 2O \rightleftarrows 2NO \tag{32}$$

The equilibrium composition of the combustion byproducts is determined by applying the law of mass action to each reaction defined in equations (32). This yields definition of a set of equilibrium reaction constants K, which, for the simple reaction $nA + mB \rightleftarrows \ell C$, are expressed in terms of species mole fraction X^{α} as

$$K \equiv \frac{\left[X^A\right]^n \left[X^B\right]^m}{\left[X^C\right]^{\ell}} \tag{33}$$

Solution of equation (32), coupled with equation (33) and conservation of total and elemental mass, yields after linearization algebraic equation system for determination of the equilibrium composition of the system, of the form,

$$\left[N_{\alpha\beta}\right] \{X^{\alpha}\} = \{\text{Constant}\} \tag{34}$$

In equation (34), the elements of the matrix $[N]$ account for the distribution of the particular species mole fraction $\{X^{\alpha}\}$ containing the βth elemental material, for example, O, H, and N. Solution of the equilibrium temperature and species concentration requires an iterative solution to a nonlinear algebraic equation system.

A considerably less expensive method (from the standpoint of computer time) may be employed to obtain an upper limit on the effects of heat release on the flow field development. The mole fractions of the dissociated species O and H are usually small compared with those of O_2 and H_2. Equations (32) may then be considerably simplified by assuming that the complete reaction

$$H_2 + \frac{1}{2} O_2 \rightarrow H_2O \tag{35}$$

is the only reaction that occurs. In this case all the H_2 reacts with the available O_2 to form H_2O. By describing the variation

of specific heats with temperature through a relationship of the form $c_p \equiv a + bT$, the temperature is solved explicitly in terms of the enthalpy and pressure without iteration.

FINITE ELEMENT SOLUTION ALGORITHM

The parabolic Navier-Stokes equation system and the three-dimensional boundary-region equation system excepting global continuity (equation (3)) are uniformly constituted as initial boundary-value problems of mathematical physics. Each of the subject partial differential equations (equations (4) to (6)) is a special case of the general, second-order, nonlinear partial differential equation.

$$L(q) \equiv \kappa\left[K(q)q_{,k}\right]_{,k} + f(q,q_{,i},x_i) + g(q,\chi) = 0 \qquad (36)$$

where q is a generalized dependent variable identifiable with each computational dependent variable. In equation (36), f and g are specified functions of their arguments, χ is identified with x_1 for parabolic flows, and x_i are the coordinates for which second-order derivatives exist in the lead term. The finite-element element solution algorithm is based upon the assumption that L(q) is uniformly parabolic within a bounded open domain Ω; that is, the lead term in equation (36) is uniformly elliptic within its domain R, with closure ∂R, where

$$\Omega = R \times [\chi_o,\chi) \qquad (37)$$

and $\chi_o \leq \chi$, is the range of the initial value operator.

Equation Development

If equation (36) is uniformly parabolic, unique solutions for q are obtained upon specification of functional constraints on $\partial\Omega = \partial R \times [\chi_o,\chi)$ and an initial-condition specification on $R \cup \partial R \times \chi_o$. For constraints on $\partial\Omega$, the general form relates the function and its normal derivative everywhere on the closure ∂R as

$$\ell(q) \equiv a^{(1)}q(\bar{x}_i,\chi) + a^{(2)}Kq(\bar{x}_i,\chi)_{,k}n_k - a^{(3)} \equiv 0 \qquad (38)$$

In equation (38), the $a^{(i)}(\bar{x}_i,\chi)$ are user-specified coefficients, the superscript bar notation constrains x_i to ∂R, and n_k is the local outward-pointing unit normal vector. For an initial distribution, assume that

$$q(x_i,\chi_o) \equiv q_o(x_i) \tag{39}$$

is given throughout $R \cup \partial R \times \chi_o$.

The finite-element solution algorithm is established for the equation system (28) to (39) by using the method of weighted residuals (MWR) formulated on a local basis. Since equation (36) is valid throughout Ω, it is valid within disjoint interior subdomains Ω_m described by $(x_i,\chi)\varepsilon R_m \times [\chi_o,\chi)$, called finite elements, wherein $\cup R_m = R$. An approximate solution for q within $R_m \times [\chi_o,\chi)$, called $q_m^*(x_i,\chi)$, is formed by expansion into a series solution of the form

$$q_m^*(x_i,\chi) \equiv \{\Phi(x_i)\}^T\{Q(\chi)\}_m \tag{40}$$

In equation (40), the functionals $\Phi_k(x_i)$ are subsets of a function set that is complete on R_m. The expansion coefficients $Q_k(\chi)$ represent the unknown χ-dependent values of $q_m^*(x_i,\chi)$ at specific locations interior to R_m and on the closure ∂R_m, called nodes of the finite-element discretization of R.

To establish the values taken by the expansion coefficients in equation (40), requires that the local error in the approximate solution to both the differential equation $L(q_m^*)$ and the boundary-condition statement $\ell(q_m^*)$, for $\partial R_m \cap \partial R \neq 0$, be rendered orthogonal to the space of the approximation functions. By employing an algebraic multiplier λ the resultant equation sets can be combined as

$$\underset{m}{S}\left[\int_{R_m}\{\Phi(x_i)\}L(q_m^*)d\tau - \lambda\int_{\partial R_m\cap\partial R}\{\Phi(x_i)\}\ell(q_m^*)d\sigma\right] \equiv \{0\} \tag{41}$$

where S_m is the mapping function from the finite-element subspace R_m to the global domain R, commonly termed the assembly operator. The number of equations (41) prior to assembly is identical with the number of node points of the finite element R_m.

Equation (41) forms the basic operation of the finite element solution algorithm and of the COMOC computer program. The lead term can be rearranged, and λ determined by means of a Green-Gauss theorem:

$$\int_{R_m} \{\Phi(x_i)\}\kappa\left[Kq^*_{m,k}\right]_{,k} d\tau = \kappa \oint_{\partial R_m} \{\Phi(x_i)\}Kq^*_{m,k}n_k d\sigma$$

$$- \kappa \int_{R_m} \{\Phi(x_i)\}_{,k} Kq^*_{m,k} d\tau \qquad (42)$$

For $\partial R \cap \partial R_m$ nonvanishing (equation (42)), the corresponding segment of the closed-surface integral will cancel the boundary-condition contribution (equation (41)) by identifying $\lambda a^{(2)}$ with κ of equation (36). The contributions to the closed-surface integral (equation (42)), where $\partial R_m \cap \partial R = 0$, can be made to vanish (ref. 6). When equations (38) to (42) are combined, the globally assembled finite-element solution algorithm for the representative partial differential equation system becomes

$$\underset{m}{S}\left[- \kappa \int_{R_m} \{\Phi\}_{,k} Kq^*_{m,k} d\tau + \int_R \{\Phi\}(f^*_m + g^*_m) d\tau \right.$$

$$\left. - \kappa \int_{\partial R_m \cap \partial R} \{\Phi\}\left(a^{(1)}_m q^*_m - a^{(3)}_m\right) d\sigma \right] = \{0\} \qquad (43)$$

The rank of the global equation system (equation (43)) is identical with the total number of node points on $R \cup \partial R$ for which the dependent variable requires solution. Equation (43) is a first-order, ordinary differential system, and the matrix structure is sparse and banded. Solution of the ordinary differential equation system is obtained by using a predictor-corrector finite difference numerical integration algorithm (ref. 6).

A solution algorithm is required for the continuity equation, which is retained as equation (3) for boundary-region flows. Since equation (3) is an initial-value problem on ρu_2 as a function of x_2, with x_1 and x_3 appearing as parameters, the approximation function need span only the transverse coordinate direction as

$$(\rho u_2)^*_m = \{\Phi(x_2)\}^T \{\rho V(x_1, x_3)\}_m \tag{44}$$

The matrix elements of ρV are nodal values of ρu_2^*; their functional dependence requires solution of equation (3) along lines (x_1, x_3) equal a constant. Since equation (3) exists in standard form as an ordinary differential equation, direct numerical quadrature yields the required solution at node points of the discretization.

Structure of the COMOC Code

The COMOC computer program system is being developed to transmit the rapid theoretical progress in finite element solution methodology into a viable numerical solution capability. In the course of generating this general-purpose system, several variants of COMOC have been developed for specific problem classes, including transient thermal analysis and the two-dimensional Navier-Stokes equations as well as the three-dimensional boundary-region equations. The present operational variant of COMOC is capable of solving each of these problem classes and has been extended to include the parabolic Navier-Stokes equation system. An on-line restart feature allows the user to switch between boundary-region and parabolic Navier-Stokes systems according to the requirements of the problem at hand.

The finite element solution algorithm is utilized to cast the original initial-valued, elliptic boundary-value problems into large-order systems of purely initial-value problems. The program then integrates the discretized equivalent of the governing equation system in the direction parallel to the predominant flow. Initial distributions of all dependent variables may be arbitrarily specified, and boundary constraints for each can be specified by the user on arbitrarily disjoint segments of the solution domain closure. The solutions for each dependent variable, and all computed parameters, are established at node points lying on a specifiably nonregular, computational lattice formed by plane triangulation of the elliptic portion of the solution domain. Each of the computational triangles is spanned by a linear approximation function used for all independent and dependent variables as well as each solution parameter.

The COMOC system is built upon the macrostructure illustrated in figure 3. The main executive routine allocates core by means of a variable dimensioning scheme based upon the total degrees of freedom of the global problem. The size of the largest problems that can be solved is thus limited by only the available core of the computer in use. The precise mix between the number of dependent variables (and parameters) and fineness of the discretization is user-specifiable and widely variable. The input module serves its standard function for all arrays of dependent variables, parameters, and geometric coordinates. The discretization module forms the finite element discretization of the elliptic solution domain and evaluates all required finite-element nonstandard matrices and standard-matrix multipliers. The initialization module computes the remaining initial parametric data required to start the solution. The integration module constitutes the primary execution sequence of problem solution. It utilizes a highly stable, predictor-corrector integration algorithm for the column vector of unknowns of the solution. Calls to auxiliary routines for parameter evaluation (viscosity, Prandtl number, source terms, combustion parameters, etc.) as specified functions of dependent and/or independent variables are governed by the integration module. The user has considerable latitude to adapt COMOC to the specifics of his particular problem by directly inserting readily written subroutines to compute special forms of these parameters. The output module is similarly addressed from the integration sequence and serves its standard function via a highly automated array display algorithm. COMOC can execute distinct problems in sequence and contains an automatic restart capability to continue solutions.

Accuracy and Convergence

The three-dimensional boundary region equation system solved using COMOC may be routinely employed to consider two-dimensional problems as a special case. This feature is important since the COMOC generated results may then be evaluated for accuracy and convergence by comparison with solutions produced by finite-difference techniques and with a similarity solution for constant specific heat. With this point in mind, three check cases were considered and are presented below.

Compressible Boundary Layer - Consider a nominal Mach 5, laminar, two-dimensional, air boundary-layer flow over an adiabatic wall in a favorable pressure gradient. With the assumption of constant specific heat, the flow is isoenergetic and it is necessary only to solve the x_1 momentum equation and the continuity equation. The initial distribution for longitudinal velocity u_1 is established from the similar solution for $\beta = 0.5$ and $S = 0$ of reference

24. The initial distribution for u_2 is obtained iteratively, and Sutherland's law is employed to compute viscosity.

The test case is initialized at $x_1 = 0.03$ m downstream from the leading edge. The boundary-layer thickness at this station, δ_o, is 0.0039 m, the local Mach number, M_e, is 3.77, the Reynolds number per unit length, N_{Re}/x_1, is 0.83×10^5 per meter, and the adiabatic wall temperature, T_w, is 1000°K. Shown in figure 4 are the COMOC computed distributions of skin friction, local free-stream Mach number, and boundary-layer thickness for the case of constant specific heat. These were obtained with two uniform finite-element discretizations corresponding to four and eight elements spanning the initial boundary-layer thickness. The input static pressure distribution $p_e(x_1)$ is also presented for reference. Only small differences, on the order of about 2 percent, exist between the two solutions, the finer discretization producing a slightly larger skin friction and smaller local Mach number. Superimposed in figure 4 for comparison purposes are the results for the similar solution (ref. 26) and a 20-zone finite-difference solution obtained with the Von Mises coordinate transformation. Agreement among the four solutions is excellent (within 2 percent) for skin friction. The similar solution for M_e lies between the COMOC and finite difference solutions, and overall agreement is within ±3 percent

Shown in figure 5 are computed velocity profiles at $x_1/\delta_o = 22.7$, which is about midway through the presented solution domain. Shown for reference is the initial longitudinal velocity profile with the node locations of the four-element discretization superimposed. Both COMOC solutions produce u_1 distributions that are slightly more concave upward in the midregion in comparison with the similar or finite difference solution. The eight-element COMOC solution lies closer to the similar solution in the region where the two finite element solutions differ. The finite difference solution lies appreciably below both the COMOC and similar solutions near the freestream. The computed transverse velocities, which are also plotted in figure 5, show only slight differences between the two discretization solutions. The trends of the COMOC solutions are in excellent agreement with the established procedures. This check case result establishes an accuracy assessment of the solution algorithm for the three-dimensional boundary-region equations.

Developing and Developed Channel Flow - Other check cases used in the evaluation of the parabolic Navier-Stokes equation system have been examined for three different channel flow configurations.

Figure 6 summarizes the results for a nonreacting subsonic flow to evaluate the ability of the pressure solution algorithm (equation (24)) to compute a constant streamwise gradient. For the fully developed channel flow, streamwise velocity and the pressure gradient are computationally maintained to within ± 2.5 percent of their initial values. The computations for developing channel flow correctly predicted the downstream distance required to attain fully developed flow; that is, COMOC predicted that the flow was fully developed at $x_1/h = 33$ compared with $x_1/h = 30$ reported in ref. 25.

Mixing and Reacting Channel Flow - An evaluation similar to that described above was performed to assess channel flow computations with heat addition. Conditions were selected such that in the initial portion of the flow, reaction of hot air with cold hydrogen induces a favorable pressure gradient (heat addition in subsonic flow). However, after the available oxygen supply is exhausted, the continued mixing of the cold hydrogen with the heated combustion produces an overall temperature drop, and hence, an adverse pressure gradient. The computational results are summarized in figure 7; the trends are observed to have been correctly predicted by COMOC while maintaining conservation of mass to within ± 1.0 percent, i.e., the correct increase and then decrease in velocity as the gas initially heats and then cools.

NUMERICAL RESULTS

The objective of this study is to provide a theoretical model describing the three-dimensional mixing and reacting flow fields which characterize scramjet combustors. Theoretical predictions will prove useful in providing guidance in selecting fuel injection/strut geometry and estimating combustor size and performance requirements. Before any theoretical model is used to provide design criteria, it is essential to test the ability of the model to determine its reliability of predictions, i.e., how close are the predictions to experimentally observed trends and are predictions generally above or below experiment. With this point in mind the COMOC code was exercised to: (1) examine the sensitivity of predictions to a number of key parameters, (2) determine the accuracy of predictions for a different nonreacting flow condition, and (3) model reacting flows.

Sensitivity Study

The sensitivity of the predicted flow field solution to a number of key parameters was studied and results presented below. Specifically, those parameters examined were discretization, eddy viscosity model, tensorial character of eddy viscosity, turbulent Prandtl number, transverse velocity. The detailed experimental results of Rogers (refs. 8 and 9) for the configuration illustrated in figure 8 provide the necessary

data base for comparison of predictions. Initial conditions for the predictions were established from these data, and the downstream station at $x_1/d = 30$ was selected as the initialization station. The original raw data consist of a single vertical traverse and three lateral traverses on the transverse plane at several x_1 stations. The measured hydrogen mass fraction distributions appear of Gaussian shape; however, the symmetry plane of the data was variously displaced from the geometric symmetry plane. Although the entire flow field could be computed numerically, the strong appearance of a data symmetry plane suggested establishment of a corresponding computational solution domain. Therefore, a cubic spline interpolation program was applied to the raw data program to establish the x_3/d location of the data symmetry plane via a minimization criteria on the wings of the Gaussian-type distributions. The spline package then interpolated the raw data for hydrogen mass fraction and u_1 and output the evaluation of the interpolation polynomials at node points of the finite-element discretization of the transverse plane. A representative case of the spline-computed distributions of hydrogen mass fraction is shown in figure 9 in comparison with the spread and context of the experimental data.

Although plots of the form of figure 9 are geometrically aesthetic, the transition from the initial distributions and significant detail on solution accuracy and trends are better obtained by plotting concentration profiles (x_2/d against Y^H) along planes x_3/d = constant at each longitudinal station for which data measurements exist, or simply examining variations along the centerplane in the normal direction and along the wall (Y^H against x_3/d at $x_2/d = 0$ and fixed x_1/d). Both of these methods of comparing predictions with data were used and examples for case 1 of Table 1 are shown in figures 10 and 11 (the solid curves shown in figure 11 represent a best fit to the data; wall values were obtained by extrapolation).

Turbulent mixing length theory has been very successful in modeling various types of flow fields as shown by Launder and Spalding, ref. 20. Therefore, before considering more complex turbulence models, the MLT given by equations (12) and (13) was used to establish a basis for comparison. As shown in figures 10 and 11, MLT and the assumption of $N^e_{Pr} = 0.90$, $N^e_{Le} = 1.0$ results in predicted H_2 mass fractions in good agreement with the data towards the outer edge of the mixing boundaries. All dependent variable boundary conditions were taken to be zero gradient at both the freestream and wall except for the velocity

components which were specified to be zero along the wall. Predicted H_2 mass fractions near the wall are greater (4.4% against 3.2% at $x_1/d = 60$, $x_3/d = 0$) than the experimental values. As will be shown below, this trend carried over for most of the other flow conditions studied (Table 2). Possible explanations for this discrepancy may be: (1) inaccuracies in the data in the vicinity of the wall, (2) inadequacies of the mixing model, and (3) specifying $u_3 = 0.0$ due to lack of experimental data for this velocity component (see discussion of case 1-4 below).

As with any multidimensional computations in compressible viscous fluid mechanics, it is important to establish a quantitative accuracy assessment. For the cold-flow configuration studied and reported herein, an accuracy measure of the adequacy of the employed discretization is possible by determining the conservation properties of the solution. For the cold mixing case, the species-continuity equation for hydrogen mass fraction can be written in explicit conservation form. Integrating this equation over a three-dimensional control volume and using Gauss' theorem (ref. 5) determines that the total hydrogen mass flow, that is, $\int \rho u_1 Y^H dA$, would be rigorously conserved by an analytic solution. COMOC evaluates this parameter at each output station by using linear finite element approximation functionals for each variable and performing the integrations analytically. (Thus, the order of the evaluation is consistent with that of the solution of the partial differential equations.)

For case 1-1 of Table 1, a monotonically increasing loss of hydrogen mass flow with increasing distance downstream was computed; at $x_1/d = 120$, the computed loss equaled 8.8 percent of the mass flow computed at station $x_1/d = 30$. The 100-element standard nonuniform discretization was refined by a factor of 2 in each coordinate direction to produce 400 finite elements spanning R (see fig. 12, diagonals omitted), and the computation was repeated on $30 \leq x_1/d \leq 60$. Over this interval, the coarse discretization yielded a computed 5 percent loss in hydrogen mass flow. The fine discretization produced a modest variation in computed hydrogen mass flow over the initial interval, with a 1 1/2-percent net loss computed by $x_1/d = 60$. The resulting detailed differences in computed distributions of hydrogen mass fraction are shown in figure 13. Above the peak and outside the near wall region, differences are undiscernible on the scale of the plots. Within the near wall region, the maximum difference in computed hydrogen levels is less than 8-percent, which compares favorably with the 10 to 20 percent spread of the "best symmetry" data. The computational expense of these comparison solutions

differed by over an order of magnitude. On an IBM 360/65, using no out-of-core devices for either case, the CPU time of the 100-element solution was about 250 seconds; on the same interval, the 400-element solution required 2600 seconds. Two parts constitute this increase (see ref. 6): a factor of about 4, due to the fact that the element DO loops in COMOC were 4 times longer, and a multiplicative factor of about 2, due to increased solution stiffness resulting from the refined grid itself. The ability of coarse finite-element discretizations, using low-order functionals, to preserve adequate engineering solution accuracy appears a distinct feature of the algorithm.

It is of interest to examine the sensitivity of predictions to variations in the empirical constants used in the mixing model. Case 1-3 of table 1 was used to examine the effect of decreasing the mixing length constant λ from 0.09 to 0.07 while reducing the effective Prandtl number from 0.9 to 0.7. In the outer region of the boundary layer $\varepsilon \propto \lambda$, hence decreasing λ will slow the momentum mixing since ε is initially decreased by 40%. Similarly, the mass diffusion coefficient is also decreased by 22 percent. As shown in figure 14, the direct effect on mass diffusion by these changes in λ and N_{Pr}^{e} are to slow the mixing rate of H_2 such that the wall concentration is lower than case 1-1 by 10 percent (4.4% vs 4.0% at the wall and 4.5% vs 4.9% at the peak).

The correlation between predictions and data for the test case shown in figures 10 and 11 is good except in the near wall region. For good agreement in the centroidal region of the hydrogen jet, it is necessary that the maximum hydrogen concentration remain off the wall. Therefore, either from three-dimensional effects or a complex turbulence interaction between the jet and the wall, there may be mechanisms in play capable of resisting the unidirectional trend of maximum diffusion to the wall. It has been hypothesized, as a result of the initial studies (ref. 5), that the existence of a mass flux transverse to the main flow direction and along the plate surface might account for the experimentally measured centroidal peak. Such a transverse mass flux could be initiated by the displacement effect of the sonic hydrogen jet issuing transverse to the main flow, since in such an interaction problem, the jet appears to the mainstream flow in many ways similar to an impervious body. Consequently, immediately downstream of the transverse jet, there must exist an approximately spheroidal fixed recirculation region near the wall, and a transverse mass flux would be required to alleviate a localized low-pressure area just downstream of this bubble.

This hypothesis was computationally evaluated in test case 1-4 by imposition of a small negative, transverse velocity distribution beneath the measured hydrogen concentration maximum

at $x_1/d = 30$. All other conditions were the same as those used in case 1-1. The magnitude and vertical extent of the imposed transverse velocity on the symmetry center plane $(x_3/d) = 0$ are shown in figure 15a. Figure 15b illustrates the lateral spread of the imposed transverse velocity distribution along a specific (x_1, x_2) plane, i.e., $x_2/d = 1.0$. As shown (figures 15a and b), the u_3 velocity component is less than one tenth its peak value for $x_1/d \geq 60$.

The influence of the imposed transverse velocity on the predicted distributions of hydrogen mass fraction at the two downstream data stations is shown in figure 16. The selected u_3 velocity distribution is observed to not significantly alter the mass fraction distributions above the peak but does substantially promote the existence of a local off-plate maximum in the centroidal region at $x_1/d = 60$. However, by the time the last data station is reached $(x_1/d = 120)$, the imposed transverse velocity distribution has been essentially dissipated, and the computed distributions of hydrogen mass fraction in the centroidal region are noted to revert to the form of the maximum existing at the plate surface. It can be concluded, therefore, that transverse mass flow is probably of influence in the near region downstream of the point of injection. However, there is as yet some undetermined mechanism for maintaining the off-axis peak in the mass fraction distribution at stations far downstream. This undoubtedly points to some deficiency in the turbulent mixing model for this configuration and/or the experimental wall values.

As recently pointed out by Launder, Reece, and Rodi (ref. 28) while effective viscosity models have led to satisfactory predictions in two-dimensional flows, their use in three-dimensional flows with more than one significant mean velocity gradient has achieved only moderate success. Considering a Reynolds-stress closure model for the problem of interest herein would be premature due to overall complexity of the flow field (compressible, variable molecular weight, not well defined initial conditions and in particular lack of turbulence measurements). However, the tensorial character of the turbulent shear stress may be examined using the COMOC code by characterizing the eddy viscosity as a tensorial quantity. Shown in figure 17a and 17b are the predicted H_2 concentrations obtained by assuming that the eddy viscosity characterizing diffusion in one of the directions normal to the main flow coordinate is twice that of the eddy viscosity in the other direction, i.e., in figure 17a, $\varepsilon_{12} = \varepsilon$ and $\varepsilon_{13} = 2\varepsilon$, whereas in figure 17b, $\varepsilon_{12} = 2\varepsilon$ and $\varepsilon_{13} = \varepsilon$. As seen from the results shown in figure 17a or 17b, it would not be possible to

improve the level of agreement between data and theory by a simple adjustment (change in a single constant) in the eddy viscosity since neither case gave any significant improvement in the predicted H_2 concentration distribution. These results suggest that direct modeling of each shear stress component may be required but further comparisons with other data are required before any definite conclusions may be drawn.

The two-equation turbulence model (k+d) of Launder and Spalding (ref. 29) has enjoyed considerable success in modeling two-dimensional turbulent flows. In this study initial values for k and d were obtained by computing an eddy viscosity from MLT, equation (12), mixing length from equation (13), and using the relationship between k, d, ℓ, and ε given by equations (14) and (16). As shown in figure 18, a modest improvement in the correlation between theory and experiment was obtained using the k+d model of ref. 29 to predict the H_2 concentrations. To be noted, however, is that the introduction of two additional equations increased computer run time by approximately 30 percent and leads us to conclude that use of higher order turbulence models for the problem of interest herein are somewhat premature at this time.

Computations for cases 1-1 and 1-6 were made assuming a constant effective Prandtl number. However, a number of studies, e.g., ref. 30, have shown that $N_{Pr)_T}$, and hence, N^e_{Pr} vary considerably across the boundary layer. Case 1-7 was considered to examine the effect of considering Prandtl number variations. Following Wassel and Catton (ref. 30), the expression given by equation (45) for the turbulent Prandtl number was used to model conditions corresponding to $q_r = 1.0$, $s/d = 12.5$.

$$N_{Pr)_T} = \frac{C_3}{C_1 N_{Pr}} \frac{1 - \exp\left[-\dfrac{C_4}{(\mu_T/\mu)}\right]}{1 - \exp\left[-\dfrac{C_2}{N_{Pr}(\mu_T/\mu)}\right]} \tag{45}$$

where $C_1 = 0.21$, $C_2 = 5.25$, $C_3 = 0.20$, $C_4 = 5.0$, and the laminar values of viscosity and Prandtl number were assumed constant, i.e., $\mu = 0.000018$ N-sec/m^2 and $N_{Pr} = 0.69$. The effective Prandtl number is obtained from equation 7b and is given by

$$N_{Pr}^{e} = \frac{\mu^{e}}{\frac{\mu}{N_{Pr}} + \frac{\rho\varepsilon}{(N_{Pr})_{T}}} \qquad (46)$$

Predictions of the H_2 concentrations obtained using this model are shown in figure 19 where it is noted that by considering a variable Prandtl number the rate of H_2 diffusion to the near wall region is decreased in agreement with the experimentally observed trends. This result suggests that the optimum mixing model for the flow field of interest would be MLT coupled with the variable Prandtl number expression given by equations (45) and (46).

Modeling Flows with Various Values of q_r and s/d

It is essential that a number of different flow conditions be examined when evaluating any empirical model before drawing any conclusions about its ability to model a class or classes of flows. Table 2 lists eight cases modeled using MLT and a constant effective Prandtl number; results are shown in figures 20 to 26. The performance of the k+d and variable N_{Pr}^{e} models for these cases may be estimated by examining predictions obtained using these models for case 2-1 (figures 17 and 18). In general, the level of agreement between predictions and experiment for these seven cases (2-2 to 2-8) are similar to those obtained in modeling case 2-1. Specifically, the predicted H_2 mass fractions were greater than the experimental values in five of the seven cases. To be noted is that mixing was predicted to be faster than observed for the three $q_r = 0.5$ cases. A means for accounting for this effect through the mixing model would be to employ the k+d turbulence equations and relate the initial turbulence kinetic energy to the H_2 injection parameter, q_r, i.e., as q_r increases the turbulence level in the boundary layer increases. The computer code was not exercised to further explore this concept since the results would represent only a data fit and not provide any new information. Detailed turbulence data would be required to test the ability of the k+d model to characterize the dominant turbulent mixing processes. However, from the comparisons between data and theory, it is concluded that the COMOC code even with the simplest turbulence model considered (MLT and $N_{Pr}^{e} = 0.9$) gives correlation with experimental data with sufficient accuracy to provide useful engineering design guidance. In the following subsections, we present results obtained using COMOC to characterize a number of scramjet injection modes.

Simulation of the Near Injection Region

A distinct feature of the three-dimensional boundary-region and parabolic Navier-Stokes equation systems is the capability to obtain a three-dimensional solution while marching in one coordinate direction. Elimination of the requirement for a downstream boundary condition is particularly important. For the subject mixing and combustion studies, however, the corresponding penalty is that an accurate initial condition is required to model adequately the complex near-injection flow field under study. In the previous section, the computations took advantage of detailed experimental profiles for the establishment of initial conditions. In the more general case, and in particular for hot-flow cases with combustion, detailed distributions of initial conditions are specifically unavailable, and a theoretical device for establishing the starting point of the solutions is required. Flow fields involving the parallel injection of dissimilar fluids present no difficulty, since smooth transitions occur and boundary-layer and shear-layer concepts are appropriate. However, for transverse injection, this is not the case, and some alternative means is required.

In anticipation of this need, a task in the early phases of the study was to evaluate the concept of a numerical "virtual source" as a means for eliminating the requirement for detailed initial conditions (ref. 5). Injection of a jet from an orifice in a plate transverse to a supersonic airstream has been the subject of a number of investigations. The important correlating parameter appears to be dynamic pressure ratio q_r. Most experimental data are for large values of q_r, for which the jet has sufficient momentum to penetrate the boundary layer and produce a complicated separation region and bow shock ahead of the jet. However, for the present cases, q_r ranges between 0.5 and 1.5, and a significant part of the jet remains within the turbulent boundary layer. Hence, mixing is initiated immediately downstream of injection. From these considerations, a theoretical model was proposed for establishing a barrel-shock - Mach disk hypothesis for turning of the transverse jet parallel to the main flow (see fig. 27). An analysis based on one-dimensional considerations was developed to characterize the jet turning. The important parameters in the model are dynamic pressure ratio q_r and free-stream Mach number M_∞, and the output is injectant momentum and flow area. Details of the model are presented in reference 5.

The validation of the concept of the virtual source as an initial-condition generator was accomplished by using the detailed cold-flow experimental data discussed in the previous section.

The detailed predicted distribution of hydrogen mass fraction are shown in figures 28 and 29 for the virtual-source simulation of the standard test case (q_r = 1.0 and s/d = 12.5). For these computations, transverse velocity u_3 was assumed zero, N^e_{Pr} = 0.9 and MLT was employed. Even after marching only 30 diameters downstream from the point of injection, agreement between the predictions and the data (fig. 28) is admirable, especially in the centroidal region, where there is an excellent prediction of an off-plate peak. At the final station x_1/d = 120 (fig. 29), agreement between the virtual-source simulation and data is excellent, being essentially identical with the results starting with data at x_1/d = 30 (fig. 10).

Reacting Flows

Three different reacting flow configurations were considered in this investigation: (1) perpendicular injection of H_2 into a supersonic stream (either air or vitiated air) from a row of circular orifices aligned across a flat plate, (2) perpendicular injection of H_2 from a circular orifice positioned on a strut in a scramjet combustor, and (3) tangential injection of H_2 also positioned on a strut in a scramjet combustor. The first case considered, referred to as case 3-1 in table 3, corresponds to case 2-1 using the virtual source simulation with the exception that here the flow is allowed to react. The conditions for this reacting flow case are not significantly different from those reported by Rogers and Eggers (ref. 10) who have experimentally investigated the reaction of hydrogen in a hot supersonic test gas flowing through a two-dimensional duct. (Data point 4 of reference 10 corresponds most closely to the conditions of case 3-1.) Case 3-1 has been introduced to examine the effects of heat release on the predicted flow field. Case 3-2 is identical to case 3-1 except the air stream has been replaced by a vitiated air stream.

Reacting flow data for the strut injection geometries have been reported by Anderson and Gooderum (ref. 11). These data (two cases) were simulated using the COMOC code, cases 3-3 and 3-4 of table 3. The perpendicular injection condition was simulated using the virtual source concept and the effects of shocks were neglected in each case except through imposition of the reported static pressure variations with distance downstream. Cases 3-5 to 3-7 examine the effect of modeling reacting flows using the k+d model, and, in particular, the effect of turbulence on reaction. Cases 3-8 and 3-9 consider the effect of ducting the flow on the mixing.

H_2 Injection from a Flat Plate - Shown in figure 30 is an alternative method for presenting these data which was extended to reacting flow comparisons. This figure presents the peak hydrogen concentration as a function of distance downstream. The agreement with data is excellent in the range $30 \leq x_1/d \leq 120$. The disagreement at $x_1/d = 7$ is not serious in light of the further downstream agreement; the indicated data point may well be significantly in error. Shown also in figure 30 are the trajectories of the peak hydrogen concentration above the plate x_2/d and the lateral spread of the jet determined at the x_3/d coordinate where the local hydrogen concentration equals 10 percent of the local maximum. Observe that the local peak of the elevation trajectory sinks to the plate surface downstream of $x_1/d = 60$, as was observed for the eight cold-flow data cases. The plotted spread of computations in this region indicates the span of x_2/d for which the predicted hydrogen concentration varies by 10 percent. The agreement of lateral spreading rate with data is excellent.

At the lower right in figure 30 is a computation of mixing efficiency η, defined as the fraction of hydrogen, integrated over the flow cross-sectional area at a given station, that would react if complete reaction with the available oxygen were to occur. This parameter has been used for correlating cold-flow data (ref. 9) and is readily computed by COMOC as an output parameter by means of the integration techniques utilized for measuring hydrogen mass flow. Hence, figures 28 to 30 demonstrate that the virtual-source concept of transverse hydrogen injection for the cold-flow configuration effectively simulates the injection phenomenon.

It is therefore hypothesized that the virtual-source concept is appropriate for combustion studies as well, and the experimental verification of this hypothesis is sought. As a first step, it is appropriate to measure the influence of combustion on the virtual-source cold-flow configuration. Shown also in figure 30 are computations carried out to $x_1/d = 30$ for the cold-flow simulation, where combustion of the hydrogen is allowed to occur according to the complete-reaction hypothesis (equation (35)). Note that the trajectory of maximum hydrogen mass fraction lies considerably above that for the cold-flow, non-reacting configuration. However, on the basis of mixing efficiency η, there is very little difference in overall mixing between the cold reacting and non-reacting cases.

The cold-flow problem is of marginal interest, however, since the average equivalence ratio of the cold-flow configuration ($\phi = 0.04$) lies well below the design level for a practical

combustor. Note that equivalence ratio is defined (ref. 11) strictly in terms of the global mass flows of hydrogen and air. For stoichiometric combustion, $\phi = 1$; for fuel-lean operation, ϕ is less than 1. It is coincidental that the cold-flow virtual-source configuration can be thermodynamically altered (only) to correspond to conditions similar to test point 4 of reference 10. To simulate the test configuration, the cold flow was computationally vitiated by imposing an arbitrary uniform background hydrogen concentration (of 1 percent) and augmenting the oxygen level of the base flow such that the corresponding composition of the computational test gas simulates the hot (wet) air used for the experiment. The total temperature of the computational simulation was approximately 2000 K; the corresponding mass flow of cold hydrogen for the vitiated virtual source yielded $\phi = 0.5$ for the simulation. Shown in figure 30 are the trajectory of maximum hydrogen mass fraction, the elevation trajectory, and the lateral spreading rate for the vitiated virtual-source simulation of the test configuration. Note that the elevation trajectory of the hot-flow configuration follows very closely the cold-flow data, a result possibly of the cold-wall ($T_w \equiv 0.5T_t$) boundary condition used for the computational simulation. It may also reflect the somewhat lessened lateral spreading rate for the vitiated reacting case, as shown in figure 30. Mixing efficiency was not computed for this vitiated combustion case. However, equivalence ratio, as a node point parameter, can be computed at any point in the solution domain. At the far right of the mixing-efficiency curve in figure 30, the experimentally determined range of equivalence ratio for test point 4 (ref. 10) is compared with the computed values. The presented computational values are in qualitative agreement with the experimental extremums on the center plane at the duct exit. Analysis of the specific conditions studied in reference 10 were beyond the scope of the current investigation. It is suggested that future efforts with the COMOC code be directed in this area.

H_2 Injection from Struts - Recent thinking on design of scramjet combustors indicate that, depending upon flight Mach number, two fuel injection modes will be required. For example, an experimental model of a strut injector system (fig. 31) is currently under construction at Langley Research Center for evaluation of combustor performance as a function of injection mode. Design of this device was augmented by an earlier experimental program intended to evaluate the essential character of the two distinctly different injection modes proposed for this type of combustor (ref. 11). Schematics of the perpendicular and parallel injection struts that are associated with current design technology are shown in figures 32a and 32b for cases 3-3 and 3-4 of table 3. Also shown are the virtual-source simulations of the proposed injection mode showing the location of the discrete injectors as

well as the orientation of the virtual-source within the computational domain. Figures 32c and 32d represent an exploded view of the virtual source simulation for each injection mode. The flux of enthalpy, mass and momentum was taken to be zero across each symmetry plane (see figures 32c and 32d). At the wall boundary, the no slip boundary condition was imposed on the velocity components; heat flux and mass transfer were assumed to be zero. Other wall boundary conditions could have been employed for the enthalpy, e.g., specified wall temperature. However, in this series of computations, our prime interest was to compare the mixing between two different strut geometries since the wall temperature effects are of lower order. Obviously, this would not be the case if heat loads transmitted to the wall were of interest. The experimentally reported pressure distributions were used to obtain the required pressure gradient distribution. At this time the analysis is limited to constant area ducts (combustors), hence, area changes with distance downstream had to be neglected. However, the major effect of the area changes were implicitly considered by use of the experimental pressure field.

Shown in figure 33 is the trajectory of the maximum hydrogen concentration as a function of injection mode for the experimental results reported in reference 11. Note indeed that the perpendicular injection mode promotes much stronger mixing and hence produces a combustion process that proceeds considerably more rapidly than that corresponding to the parallel injection mode. Also plotted in figure 33 are the pressure distributions used for the computations, as well as the computer distribution of equivalence ratio on the center plane at $x_1/d = 150$ across one-half of a jet. Note that for the parallel injection mode, the range of computed equivalence ratio is twice that of the perpendicular case, in qualitative agreement with the data ranges from reference 11. Furthermore, the experimental evaluation of the differences in the flame shape for the two injection modes (ref. 11) with respect to apparent mixing rate is in agreement with the maximum hydrogen trajectories by the virtual-source solution.

Effects of Turbulence and Area Constraints - A number of investigators have shown that it is often important to consider the interaction between the turbulent and reacting flow, e.g., ref. 31. Mixing on the molecular scale is required for a chemical reaction to occur, hence, although the fuel and oxidizer may be mixed in the turbulent sense, i.e., on the macroscale, only a fraction of the fuel-oxidizer is available for reaction. Chung, ref. 31, has proposed a simple model to consider this reaction limiting phenomena wherein the rate at which the reaction is allowed to occur is limited by the rate of turbulence dissipation. The effect of the turbulence-chemistry interaction on the predicted flow field was analyzed using the virtual-source concept, the k+d turbulence model, and the reaction-rate limiting model of ref. 31.

Case 3-5 represents a case where the flow does not react, i.e., H_2 and O_2 mix on the microscopic scale and does not react. For this case the wall temperature was assumed constant at 296.0°K, hence, there is a negligible amount of heat flux between the gas stream and wall. In cases 3-6 and 3-7 the H_2/O_2 mixed on the molecular scale are assumed to autoignite. Table 4 shows the predicted surface heat flux at $x_1/d = 30$ across the flow field for cases 3-6 and 3-7 where it is seen that including the turbulence-chemistry interaction in the model has reduced the peak flux by approximately 36 percent. Results of the nonreacting case (3-5, flow conditions identical to case 2-1) were used to examine the effect of the reaction on H_2 mixing. It was noted that the mixing efficiency η for case 3-5 was 76 percent, whereas when considering complete reaction (case 3-6) η = 81 percent. This result suggests that for these conditions reaction does not have a significant effect on the mixing efficiency which is in agreement with observations reported in reference 10.

Three final cases (3-8a, 3-8b, and 3-9) were considered to examine the effect of including the fact that the flow field is ducted, and hence, generates a longitudinal pressure gradient due to boundary layer displacement effects, heat release, and friction losses. Rogers (ref. 10) performed his experimental studies in a 23 cm square test section divided by a splitter plate from which H_2 was injected from a row of orifices. Since reacting flow was not of interest in these (ref. 10) studies, the equivalence ratio was very low, i.e., approximately 0.04. Therefore, it is not surprising that the primary result from these cases was that considering the ducting of the flow had no significant effect on the velocity, temperature, and H_2 concentrations for physically reasonable duct heights. Specifically, the pressure increased by approximately 25 percent in cases 3-8a and 3-9 with a slight drop in the maximum velocity (~ 2 percent). However, the reacting flow could be forced to thermally choke by continually decreasing the duct height (increasing mixture ratio to 0.50) to very small values, e.g., case 3-9 where $x_2 \approx 2.0$ cm. (compared to 13.5 cm which is the half height of the wind tunnel section used in reference 10).

The results presented for the cases of table 3 show that the analytical predictions are in general agreement with experimentally observed trends. Further use of the theoretical model is definitely required, in particular in modeling data for other flow conditions, e.g., refs. 26, 27, 32. Areas of particular interest which have not been considered in any significant detail are comparing model predictions with wall heat flux/temperature data, combustor pressure distributions, and combustor exit conditions. The utility of the COMOC code as a design tool will be significantly enhanced as the data base of flow conditions modeled using the code expands.

CONCLUDING REMARKS

An analytical investigation has been presented on the turbulent mixing and reaction of hydrogen jets injected from multiple orifices transverse and parallel to a supersonic airstream. The primary conclusions of this study are:

(1) The analysis has immediate utility in evaluating the mixing effectiveness of transverse H_2 injection data since it has been tested in its ability to model this type of data.

(2) Turbulent mixing length theory, constant effective Prandtl number, and a Lewis number of unity provide reasonable agreement with transverse H_2 injection data downstream of the near injection region. Improvements in the correlation between predictions and experiment were obtained using a turbulent Prandtl number model and a two-equation turbulence model.

(3) The effect of turbulence-chemistry interaction could reduce the wall heat flux by as much as 36 percent. Comparisons with data are required to substantiate this predicted result.

(4) Results demonstrate that the theoretical model embodied in the COMOC code has the potential for providing useful engineering design guidance for data covering a broad range of flow conditions, combustor geometries, and injection models.

(5) As with all complex turbulent flows, reliable theoretical predictions are only attainable upon testing a model's ability to accurately characterize the class of flows of interest. Future efforts should be directed toward using the code in modeling data for a wide range of flow conditions.

Although efforts herein were primarily directed toward comparing predicted and experimental H_2 mass fractions, other types of data are available, e.g., wall temperature and heat flux data, nozzle exit conditions, combustor pressure variations. The potential of developing COMOC as a design tool will be significantly enhanced as the data base of flow conditions modeled expands. In addition, areas for improvement in the model will become apparent. Ultimately, the code may well both supplement and in some cases replace the costly experimental evaluation of prototype designs.

APPENDIX

DATA DECK PREPARATION

A description of how to prepare a data deck for the 3DBR variant of COMOC was reported in reference 5. In that version of the code, flows were considered where the pressure field was given and no area constraints imposed on the flow. In modifying the code to consider constant area ducted flows (3DPNS-COMOC) some minor modifications to the data input procedure were required. Table A-1 is a listing of the data deck used to run case 3-8b which is a reacting, ducted flow. Other problems with different geometries or flow conditions can be treated using this data check as a starting point since approximately one-third of the COMOC data deck is associated with standard call sequences as well as output format specifications and arrangement instructions. If only scramjet combustors were to be analyzed then these standard data cards could be incorporated into the main program, and hence, removed from the data deck. They have been retained in order to allow for future modifications and additions for those interested in expanding the analysis capability of the code. It is suggested, however, that the standard data not be altered without consulting reference 7. Details on data deck preparation are presented below. The input may be conveniently divided into four distinct data sets. Input data set 1 deals with the definition of reference conditions, number of dependent variables, type of flow (reacting or non-reacting), etc. Input data set 2 deals with the finite element discretization, wherein the number of nodes and finite element sizes and location are defined. Input data set 3 defines the type and format of the output, whereas data set 4 prescribes the initial conditions, pressure field and boundary conditions. The user of COMOC does not require becoming familiar with input data set 3 unless the code is modified to consider dependent variables other than u_1, u_2, u_3, H, Y_{H_2}, Y_{O_2}, and Y_{N_2}. In order to make such a modification, a familiarity with details of the codes internal structure is required and the Programmer's manual should be consulted (reference 7).

Data Set 1

Cards 1 to 4 of Table A1 Represent Input Data Set 1.

Card 1.1 Starting in Column 1 FEBL used to start execution of COMOC

Card 2.1 Starting in Column 1 include 3DPNS if a constant area duct is to be considered and hence pressure will be

computed internally. If the static pressure field is to be given then starting in Column 1 include 3DBR

Card 3.1-3.n Namelist NAME01. A complete list of all NAME01 variables and their default values is listed in subroutine FENAME. As seen from Table A1 of the one-hundred and sixty-seven parameters which can be read in NAME01, only eight need be considered for scramjet problems of interest. The remaining parameters have been retained to facilitate future expansion and modification of the code. The seven integer variables, which are required, are defined as follows. Note that in inputting in namelist form there is no designated column or order for each variable. The only requirement is that a comma follow immediately after each integer value.

NEQKNN		Number of dependent variables to be integrated in X1 direction
IGAS	0	Isoenergetic flow with constant c_p
	1	General flows
IFR	0	Equilibrium composition or complete reaction (determined by version of subroutine GAS used in COMOC)
	1	Frozen composition
KDUMP	0	Suppress debug output in gas subroutine
	1	Print debug output
NPVSX		No. of entries in pressure table
NSCX	0	Uniform X3 interval in discretization
	1	Non-uniform X3 interval in discretization
NSCY	0	Uniform X2 interval in discretization
	1	Non-uniform X2 interval in discretization
NE1E2	0	Laminar Flow
	1	Mixing length theory

Cards 4.1-4.n Namelist NAME02. A complete list of all NAME02 variables and their default values is given in Subroutine FENAME. As seen from Table A1 of the one-hundred and seventy-four parameters which can be read in NAME02 only fifteen need be considered and are defined below. The input mode is identical to NAME01.

UINF	Reference (freestream) velocity (F/S)
TØFINF	Reference stagnation temperature (^{o}R)
REFL	Reference length (F)
TØ	Initial X1 station (F)
TD	Length of X1 solution, starting at TØ(F)

DELP	Percent increment of TD at which output is desired
VSTART	Percent of TD at which transverse velocity (U2) computation starts - Default = 100%.
XSCALE	Multiplier on x_3 to convert discretization to feet as input under Mode 2 (see lines 7.1-7.n)
YSCALE	Multiplier on x_2 to convert discretization to feet as input under Mode 2 (see lines 7.1-7.n)
CON	Constant in mixing length theory
XLAM	Constant in mixing length theory
PR	Effective Prandtl number
SCT	Effective Schmidt number
CVU	Equal to 0.009659 if simplified GPAHFT subroutine is employed, i.e., where simple reaction model is used. If equilibrium composition is employed use default value (do not input CVU).

Data Set 2

Cards 5 to 7 of Table A1 represent input data set 2

Card 5.1 Starting in column 1, FEDIMN calls the subroutine to generate vector lengths and array entry points. This card and its position cannot be altered by the user.

Card 6.1 Starting in column 1 LINK1 - then after leaving a blank in column 6 - place a 1 in any column from 7 to 72. This card instructs the program to call subroutine LINK1 to read the finite element discretization in the (X2, X3) plane.

Cards 7.1-7.n This set of cards can be input in one of two modes depending on the integer values of NSCX and NSCY read in NAME01. Their function is to define the discretization. In either mode, the input card format is free - meaning no specific column has to be filled. A blank field indicates that a value has been read and the code search for the next value, which can be on the source card or the next card. A "T" represents the end of the data set. The two possible input modes are as follows.

Mode 1: Automatic Uniform Discretization
Occurs for NSCX = NSCY = 0 (in NAME01) where user set XSCALE = desired element width in the X3 direction and YSCALE = desired element height in the X2 direction (in NAME02). On card 7.5 in any column indicate the number of the first node

(always 1). Skip one or more places and add the last node number in the X2 direction. Place a comma immediately after the last X2 node number. Repeat for X3 direction, e.g., if YSCALE = 0.004 and XSCALE = 0.002 and we desired 21 × 2 nodes and 2 columns then card 7.5 would appear as

```
 1  21, 1  2,
```

The sequence would be completed by placing a "T" either on this card or on a following card in any column from 1-72. The elements would be 0.004F high by 0.002F wide.

Mode 2: Automatic Non-Uniform Discretization

Occurs for NSCX = 1 and NSCY = 1. Set X3 discretization first, X2 discretization second. Data are used in sets of 3 integers at a time. First integer identifies finite element interval concerned, next two indicate element width (or height) as a dimensionless ratio, e.g., 3 1200 ≡ 3/1200

e.g.,
```
1  3  1200,2  1  600,3  5 1200,...
T
1  1  600,7  1 600,8  7 1200,...
T
1  11, 1  4,
T
```

This generates a finite element discretization of 11 node rows × 4 node columns. The element widths (intervals between node columns) are respectively 3/1200, 1/600, ... The height of the first 7 element rows is uniformly 1/600, eighth is 7/1200, etc. These dimensionless intervals are converted to feet by being multiplied by XSCALE and YSCALE (Cards 4.1-4.9)

Data Set 3

Cards 8 to 29 of Table A1 represent input data set 3

Card 8.1 Starting in column 1 COMTITLE, which designates that the following card will be a title card.

Card 9.1 Title card (columns 1-80) which is printed on cover page of output.

Card 9.2 Starting in column 1 DONE indicating that this sequence is complete.

Card 10.1 Starting in column 1 DESCRIPT - then in column 11 or more - 204 followed by one or more spaces and a "T" designating the end of this card. Note that any message can be placed after the "T" without affecting the data.

Cards 11.1-11.n — Up to ten title cards can be input which will be printed at each output station (X1) (hence n $\leq$ 10). These titles will head the generated output sequence.

Card 12.1 — Starting in column 1 DONE

Cards 13.1-27.1 — These cards should not be changed without consulting the programmer's manual (reference 7). Only a very brief description of their function is given below.

Cards 13.1-17.1 — Provide the output data heading descriptors.

Cards 18.1-19.21 — Designate what multiplying factor should be used to convert each output variable to units compatible with the headings given by cards 13.1 to 13.12.

Cards 20.1-21.7 — Designate vector location of variables to be printed per headings given by cards 13.1 to 13.12 after being multiplied by factors designated by cards 18.1 to 19.21.

Cards 22.1-23.4 — Designates what variables are to be printed out at all node point locations. Any variable ending with the numerals 248 represents an dependent variable. The numerals preceding the 248 designate what dependent variable is to be printed. For Table A1 conditions the following number-parameter relations hold. The variable location contains the dimensionless value and is printed as such. Free format is used.

Location	Variable
1248	u_1
285	static temperature
320	static enthalpy
284	density
10248	N_2 elemental mass fraction
3248	u_3
278	c_p
1248	stagnation enthalpy
9248	H_2 elemental mass fraction
8248	O_2 elemental mass fraction

1247	μ_{eff}
334	$Pr)_{eff}$
292	μ (laminar)
314	$Sc)_{eff}$

Cards 24.1-25.2 — Indicates the multiplier to be used on the variables designated by cards 22.1 to 23.4 prior to print out. Here all fourteen variables are scaled by unity, i.e., they retain their dimensionless form.

Card 26.1 — Starting in column 1 COMOC to key code that the problem description is to be provided on the following cards.

Cards 28.1-28.4 — Problem description on four cards columns 1-80. This description is printed once at start of run.

Card 29.1 — Starting in column 1 DONE

Data Set 4

Card 30.1 — Starting in column 1 VX3ST designating that the next card will give the X1 locations at which pressure will be input - X1 in feet and pressure in PSFA. If 3DBR option is used this pressure profile will be used for the complete calculation. If 3DPNS is used this pressure profile is used to specify the initial pressure and to compute the initial pressure gradient.

Card 31.1 — Starting in any column, the X1 locations for pressure data. Each value must be separated by one or more spaces. No integer value indicating the number of points to be read is required. The code counts the values on the card. Data set is complete by placing a "T" after the last value. Any number of cards may be used.

Card 32.1 — Starting in column 1 VPVSX

Card 32.2 — Pressure points in PSFA. Same format as card 31.1.

Card 33.1 — Starting in column 1 IPINT and in any column after 10 include -1. This card designates that the integer array numbers of the dependent variables will follow on card 34.1. The program will integrate the first NEQKNN of these values and also u_2.

Card 34.1 Starting in any column list the integer values of the dependent variables which correspond to the following key:

Integer	Variable
1	u_1
2	u_2
3	u_3
4	H
5	Open
6	Open
7	Open
8	Y^{O_2}
9	Y^{H_2}
10	Y^{N_2}

A free format is used, hence, the sequence is terminated with a "T." The open integers 5, 6, and 7 have been retained to accommodate the introduction of additional variables such as turbulence kinetic energy.

Card 35.1 Boundary conditions are required at each boundary node point for each dependent variable. The following input instructions refer to any dependent variable. The data cards defining boundary conditions for other variables follow the preceding boundary condition data cards, i.e., cards 35.1 and 36.1 are repeated for each dependent variable.

There are three modes under which boundary conditions at each boundary node may be defined: (1) zero normal gradient, (2) value fixed to its initial value, and (3) normal gradient defined as a finite value, Eq. A1.

$$\frac{\partial f}{\partial n} = a \qquad \text{(A1)}$$

Mode 1: Zero Gradient Boundary Condition
This represents the default boundary condition hence any node whose boundary condition is not defined will automatically be given a zero

gradient boundary condition, e.g., $\frac{\partial Y_{H_2}}{\partial n} = 0$ is generally valid on all boundaries, hence cards 35.1 and 36.1 are not input for this variable.

Mode 2: Boundary Node Fixed to its Initial Value
Starting in column 1 KBNO and after column 10 the number of the dependent variable whose boundary condition will be defined on card 36.1.

Mode 3: Boundary Node with Defined Normal Gradient, Eq. A1
Starting in column 1 KBNO, in column 11 the number of the dependent variable, and in column 21 the integer 1 which indicates that mode 3 boundary condition will be imposed.

Card 36.1

Mode 1: Card 36.1 not used for this mode

Mode 2: At each station the cross-sectional computational domain corresponds to a rectangular shape. Herein we define, for future reference, the boundaries as TOP, BOTTOM, LEFT, and RIGHT. The code has been programmed so that nodes along a given boundary are not required to have the same boundary condition.

To fix values along the boundary, the general card image is as follows:

Column =	1	11	21	31	41	51	61	71
Card =	BOTTOM	NB	TOP	NT	RIGHT	NR	LEFT	NL

This card designates that the first NB, BOTTOM, NT, TOP, NR, RIGHT, and NR, LEFT boundary nodes will be held constant. By leaving any of the integers (NB, NT, NR, or NL) out all nodes are held constant. If only TOP and LEFT nodes are to be held constant, the card image would contain the word TOP in column 1 and LEFT in column 21. For those nodes not defined the default boundary condition (mode 1) applies.

Mode 3: As in mode 2 we make use of the TOP, BOTTOM, LEFT and RIGHT designation of the boundaries. However, unlike mode 2 all nodes along a given boundary must be treated the same. Starting in column 1 the descriptor of the boundary is given followed

by the value of A starting in column 21 and followed by a blank space and then the integer 2, e.g., if A = .342

```
Column = 1.       21
Card   = BOTTOM   .342 2
```

Similarly, conditions for TOP, LEFT, and RIGHT may be employed. The 2 following the value instructs the code that the input boundary condition will be input in dimensionless form, e.g., if $f \equiv u_1$ then A must be defined consistent with the velocity non-dimensionalized by u_{ref} and the length scale normalized by L_{ref}.

Card 37.1 — Starting in column 1 PRINT which designates that the message appearing on the following card will be printed before execution of the run.

Card 38.1 — Anywhere in columns 1-80 a message which is printed before execution which has generally been used to describe the type of boundary conditions employed.

Card 39.1 — Starting in column 1 LINK3 then in any column after 11 the integer 4, which instructs the program to call subroutine LINK3. The integer 4 instructs the code to execute the DIMEN section of LINK3 (see reference 7).

Card 40.1 — Starting in column 1 LINK1 then in any column after 11 the integer 3 which instructs the program to call subroutine LINK1. The integer 3 instructs the code to execute the GEOMFL section of LINK1 (see reference 7).

Card 41.1 — Starting in column 1 VTEMP - then in any column after 11 - the integer -58. VTEMP designates that the stagnation temperatures at each node point will be input on the following cards. The integer -58 instructs the code to put the temperatures (input in ^{o}R) into dimensionless form by dividing by variable number 58.

Cards 42.1-42.n — Starting in any column the stagnation temperatures at each node point. The order that the values appear on the card(s) correspond to the node number. The nodes are numbered as follows. Consider a problem with n rows and m columns. Node 1 corresponds to the lower left corner node and nodes 1 to m designate the nodes along the bottom. The second row from the bottom is

numbered from m+1 to 2m and so on with the upper right node number being n×m. If N successive values x are identical then these values may be input as N*X rather than X space X space ... X. The end of data is designated by a "T" after the last entry.

Card 43.1 — Cards 43, 44, and 45 are used to input one of the velocity components in ft/s. These three cards must be repeated for each of the three velocity components u_1, u_2, and u_3. If a velocity is not defined, it is set equal to zero.

Starting in column 1 VYY then in any column after 11 the integer -27. VYY designates that one of the dependent variables to be integrated forward will be input on the following cards. The integer -27 instructs the code to divide the input variable by the value stored in RARRAY(27) which is the reference velocity.

Cards 44.1-44.n — Value of the u_1 velocities in ft/sec using same free format mode as used in cards 42.1-42.n.

Card 45.1 — Starting in column 1 VYYEND - then in any column after 11 - the integer 1. This card indicates that the variable input above (cards 44.1-44.n) correspond to values of dependent variable 1 (u_1). Repeat cards 43-45 for u_2 and u_3 and designate what velocity component is being input by the integer on card 45.1.

Card 46.1 — Starting in column 1 VYY. Note the absence of any integer indicates that the variables are in the proper dimensionless form.

Cards 47.1-47.n — Values of dependent variable at each node point.

Card 48.1* — Starting in column 1 VYYEND then in any column after 11 the integer 9. This card indicates that the variable input above (cards 47.1-47.n)$_{H_2}$ correspond to values of dependent variable 9 (Y^{H_2}).

Cards 49.1-56.1 — These cards are not to be altered. They direct the code to the integration loop and control the printout of reference values which appear at the end of the output description.

*Initial total enthalpy is obtained from stagnation temperature. If initial values of O_2 and N_2 are not input, they are computed internally using the assumption that the mass other than H_2 is 23.2% O_2 and 76.8% N_2, i.e., air.

TABLE A1

COMOC SAMPLE INPUT DATA DECK

Data Set 1 (1.1 to 4.6)

```
1.1 FEBL
2.1 3DPNS
3.1 FENAME
3.2  &NAME01
3.3            NPVSX=2,            NSCX=1,             NSCY=1,
3.4     NE1E2=1,
3.5            NEQKNN=3,           IGAS=1,             IFR=1,              KDUMP=1,
3.6  &END
4.1  &NAME02
4.2            UINF=2272.,         TOFINF=533.0,       REFL=.003333333,
4.3            XSCALE=0.003333333, YSCALE=0.003333333, VSTART=101.0,
4.4            TO=0.0,             TD=0.1,             DELP=05.0,
4.5   CON=0.435,  XLAM=0.07,  PR=0.7,  SCT=0.7,  CVU=C.009659,
4.6  &END
```

Data Set 2 (5.1 to 7.6)

```
5.1 FEDIMN
6.1 LINK1    1                                                              SETUP
7.1     1 75  100, 2  50  100, 3  125  100, 4  150  100, 5  225  100,
7.2 T   INCREMENTS BETWEEN X3, NODE-NUMERATCR-DENOMINATOR
7.3  1 1 4, 2 1 4, 3 1 2, 8 1 2, 9 1 1, 10 9 2, 11 27 2, 12 55 2,
7.4 T   INCREMENTS BETWEEN X2
7.5   1 13, 1 6,
7.6 T   13 ROWS AND 6 COLUMNS NORMALIZED BY LREF,HENCE X-Y SCALES =LREF
```

TABLE A1 (Contd)

Data Set 3 (8.1 to 29.1)

```
 8.1 COMTITLE
 9.1   VIRTUAL SOURCE - 3DPNS - MLT  -  COMPLETE REACTION
 9.2 DONE
10.1 DESCRIPT  204       T  DESCRIPTIVE TITLE AT BEGINING OF OUTPUT.
11.1   VIRTUAL SOURCE - 3DPNS - MLT  -  COMPLETE REACTION
11.2
12.1 DONE
13.1 DESCRIPT  332       T  IOPAR  PARAMETER TITLES FOR OUTPUT.
13.2  REFERENCE     ENGLISH-FT      ENGLISH-IN        M-K-S            C-G-S
13.4  LENGTH.....    .FT.....     .IN.....     .M.....     .CM.....
13.4  VELOCITY.....  .FT/S.....   .N.A.....    .M/S.....   .CM/S.....
13.5  DENSITY.....   .LBM/FT3.... .N.A.....    .KG/M3.....  .G/CC.....
13.6  TEMPERATURE....  .RANKINE.... .N.A.....  .KELVIN.....  .N.A.....
13.7  ENTHALPY.....  .BTU/LBM....  .N.A.....   .KJ/KG.....  .N.A.....
13.8  FROZ.SPEC. HEAT  .BTU/LBM-R..  .N.A.....  .KJ/KG-K....  .N.A.....
13.9  VISCOSITY.....  .LBM/FT-S...  .N.A.....  .NT-S/M2....  .POISE.....
13.10 LOCAL PRESSURE    .PSF.....   .PSI.....   .NT/M2.....   .TORR.....
13.11 LOCAL SOLUTION     MACH NO.    DPDX1(LBF/FT3) MAX. H2 CONC.  MIX EFF.(ETA)
13.12 X1/LREF           DX1/LREF       EPSILON     DX1MIN/LREF
14.1 DONE
15.1 DESCRIPT  203       T  IFMTHD TITLES FOR OUTPUT DEPENDENT VARIABLES.
16.1 U1/UREF          T/TREF          HSTAT/HREF      RHO/RHOREF      ELEM.N2 MAS.FRAC
16.2 U3/UREF          CPF/CPFREF      HTOT/HREF       ELEM.H2 MAS.FRACELEM.O2 MAS.FRAC
16.3 EFF.MU/MUREF     EFF. PRANDTL NO.MU/MUREF        EFF.SCHMIDT NO. TKE/EKNINF
16.4 DISS/EPSINF
17 1 DONE
```

TABLE A1 (Contd)

```
18.1 MPARA   -1
19.1   5*2
19.2    2     2     162     164     163
19.3    2     2      2      164     163
19.4    2     2      2      170     174
19.5    2     2      2      165      2
19.6    2   -175     2       2       2
19.7    2     2      2       176     2
19.8    2     2      2      177      178
19.9    2     2     169     168     167
19.10   2     2       2       2      2
19.20   2     2     2    2
19.21
20.1 IONUMB  -1
21.1 999
21.2 5*200 999
21.3          200 4*43  200 27 200 2*27 200 1C 200 2*1C 200 58 200 58 200
21.4  200 97 200 97 200  200 30 200 30 200 200 38 200 2*38
21.5  999
21.6   39 4*36 200 61 100 134 122 11 12 14 85
21.7
22.1IOSAVE  -1
23.1 1248  285  320  284  10248
23.2 3248  278  4248  9248   8248
23.3 1247  334   292  314
23.4 T U,T,HS,RHO,N2,V,CP,HTOT,H2,O2,DIFU,PR NO.,LAM.VISC.,SCT.NO.
24.1IOMULT  -1
25.1 14*2
25.2 T U,T,HS,RHO,N2,V,CP,HTOT,H2,O2,DIFU,PR NO.,LAM.VISC.,SCT.NO.
26.1COMOC
27.1DESCRIPT
28.1  VIRTUAL SOURCE - 3DPNS - MLT  -  COMPLETE REACTION
28.2  TURBULENCE MODEL EMPLOYED IS DESCRIBED IN USER S MANUAL NASA CR-132450,1974.
28.3  CALCULATIONS ARE STARTED USING VIRTUAL SOURCE CONCEPT TO REPLACE
28.4  COMPLEX NEAR INJECTION FLOW FIELD.
29.1DONE
```

TABLE A1 (Contd)

Data Set 4 (30.1 to 56.1)

```
30.1VX3ST
31.1   0.0      100.      T X1 TABLE FCR PRESSURE
32.1VPVSX
32.1   193.     193.      T PRESSURE  TABLE PSF
33.1IPINT   -1
34.1  1 4 9 8 10 2 3       T
35.1KBNO     1
36.1BOTTOM                DONE
37.1PRINT
38.1          FIXES U1 (VARIABLE NO. 1) ALONG WALL TO INITIAL VALUE
39.1LINK3    4                                                          DIMEN
40.1LINK1    3                                                          GEOMFL
41.1VTEMP                          -58
42.1  78*533.0    T
43.1VYY                       -27
44.1     6*0.0
44.2    6*795.0
44.3     6*1503.
44.4     6*1660.      6*1759.
44.5     2*1550.    4*1833.
44.6     3*1550.    3*1892.
44.7     2*1550.0   4*1942.
44.8  1550.0  2*2272.0  3*1985.0
44.9  3*2272.0 3*2068.0 12*2272.0
44.10 6*2272.0
44.11T  INITIAL U1 PROFILE
45.1VYYEND   1
```

TABLE A1 (Contd)

```
46.1VYY
47.1 30*0.0 2*1.0 4*0.0 3*1.0 3*0.0 2*1.0 4*0.0 1.0 23*0.0
47.2  6*0.0
47.3 T INITIAL H2 MASS FRACTION PROFILE
48.1VYYEND   9
49.1QKNINT
50.1DESCRIPT
51.1DONE
52.1DESCRIPT 3
53.1 REFERENCE LENGTH,LREF                              43 FT.
53.2 REFERENCE VISCOSITY.LAMINAR VALUE
53.3 EVALUATED AT REF. TEMPERATURE.                     38 LBM/FT-S
53.4 FREESTREAM VELOCITY AT XO(=UREF)                   27 FT/S


53.5 STAGNATION TEMPERATURE (CONSTANT,=TREF)            58 DEG R
53.6 FREESTREAM DENSITY AT XO(=RHOREF)                  10 LBM/FT3
53.7 FREESTREAM MACH NUMBER AT XO                      154
53.8 STATIC PRESSURE AT XO                               9 PSF
53.9 NUMBER OF NODES                                   -16
53.10NUMBER OF FINITE ELEMENTS                         -14
54.1DONE
55.1END
56.1EXIT
```

REFERENCES

1. Becker, J. V. and Kirkham, F. S., "Hypersonic Transports. Vehicle Technology for Civil Aviation - The Seventies and Beyond," NASA SP-292, 1971, pp. 429-445.

2. Bushnell, D. M., "Hypersonic Airplane Aerodynamic Technology. Vehicle Technology for Civil Aviation - The Seventies and Beyond," NASA SP-292, 1971, pp. 63-84.

3. Henry, J. R. and Beach, H. L., "Hypersonic Air-Breathing Propulsion Systems. Vehicle Technology for Civil Aviation - The Seventies and Beyond," NASA SP-292, 1971, pp. 157-177.

4. Henry, J. R. and Anderson, G. Y., "Design Considerations for the Airframe-Integrated Scramjet," NASA TM X-2895, 1973.

5. Baker, A. J. and Zelazny, S. W., "A Theoretical Study of Mixing Downstream of Transverse Injection Into a Supersonic Boundary Layer," NASA CR-112254, 1972.

6. Baker, A. J. and Zelazny, S. W., "COMOC: Three-Dimensional Boundary Region Variant. Theoretical Manual and User's Guide," NASA CR-132450, 1974.

7. Orzechowski, J. A. and Baker, A. J., "COMOC: Three-Dimensional Boundary Region Variant. Programmer's Manual," NASA CR-132449, 1974.

8. Rogers, R. C., "A Study of the Mixing of Hydrogen Injected Normal to a Supersonic Airstream," NASA TN D-6114, 1971.

9. Rogers, R. C., "Mixing of Hydrogen Injected From Multiple Injectors Normal to a Supersonic Airstream," NASA TN D-6476, 1971.

10. Rogers, R. C. and Eggers, J. M., "Supersonic Combustion of Hydrogen Injected Perpendicular to a Ducted Vitiated Airstream," AIAA Paper No. 73-1322, November 1973.

11. Anderson, G. Y. and Gooderum, P. B., "Exploratory Tests of Two Strut Fuel Injectors for Supersonic Combustion," NASA TN D-7581, 1974.

12. Pal, A. and Rubin, S. G., "Viscous Flow Along a Corner. Part I. Asymptotic Features of the Corner Layer Equations," AFOSR-69-1225TR, U.S. Air Force, May 1969. (Available from DDC as AD 693 630.)

13. Cresci, R. J., Rubin, S. G., Nardo, C. T., and Lin, T. C., "Hypersonic Interaction Along a Rectangular Corner," AIAA J., 7, No. 12, 1969, 2241-2246.

14. Rubin, S. G. and Lin, T. C., "A Numerical Method for Three-Dimensional Viscous Flow. Application to the Hypersonic Leading Edge," J. Comput. Phys., 9, No. 2, 1972, 339-364.

15. Caretto, L. S., Curr, R. M., and Spalding, D. B., "Two Numerical Methods for Three-Dimensional Boundary Layers," Comput. Methods Appl. Mech. & Eng., 1, No. 1, 1972, 39-57.

16. Curr, R. M., Sharma, D., and Tatchell, D. G., "Numerical Predictions of Some Three-Dimensional Boundary Layers in Ducts," Comput. Methods Appl. Mech. & Eng., 1, No. 2, 1972.

17. Patankar, S. V. and Spalding, D. B., "A Calculation Procedure for Heat, Mass and Momentum Transfer in Three-Dimensional Parabolic Flows," Int. J. Heat & Mass Transfer, 15, No. 10, 1972, 1787-1806.

18. Amsden, A. A. and Harlow, F. H., "The SMAC Method: A Numerical Technique for Calculating Incompressible Fluid Flows," LA-4370, Los Alamos Sci. Lab., Univ. of California, 1970.

19. Baker, A. J., "Finite Element Solution Theory for Three-Dimensional Boundary Flows," Comput. Methods Appl. Mech. & Eng., 4, No. 3, 1974, 367-386.

20. Launder, B. E. and Spalding, D. B., Lectures in Mathematical Models of Turbulence, Academic Press, Inc., 1972.

21. Patankar, S. V. and Spalding, D. B., Heat and Mass Transfer in Boundary Layers, Second Ed. Int. Textbook Co., Ltd., London, 1970.

22. "Free Turbulent Shear Flows," Vol. I - Conference Proceedings, NASA SP-321, 1973.

23. Wheeler, A. J. and Johnston, J. P., "An Assessment of Three-Dimensional Turbulent Boundary Layer Prediction Methods," Trans. ASME, Ser. I, J. Fluids Eng., 95, No. 3, 1973, 415-421.

24. Christian, J. W., Hankey, W. L., and Petty, J. S., "Similar Solutions of the Attached and Separated Compressible Laminar Boundary Layer With Heat Transfer and Pressure Gradient," ARL 70-0023, U.S. Air Force, 1970. (Available from DDC as AD 705 581.)

25. Schlichting, H. (J. Kestin, transl.), Boundary-Layer Theory, Sixth Ed. McGraw-Hill Book Co., Inc., 1968.

26. Russin, W. R., "Performance of a Hydrogen Burner to Simulate Air Entering Scramjet Combustors," NASA TN D-7567, 1974.

27. Eggers, J. M., "Composition Surveys of Test Gas Produced by a Hydrogen-Oxygen-Air Burner," NASA TM X-71964, 1974.

28. Launder, B. E., Reece, G. J. and Rodi, W., "Progress in the Development of a Reynolds-Stress Turbulence Closure," J. Fluid Mechanics, 68, Part 3, 1975, 537-566.

29. Launder, B. E. and Spalding, D. B., "The Numerical Computation of Turbulent Flows," Computer Methods in Applied Mechanics and Engineering, 3, 1974, 269-289.

30. Wassal, A. T., and Catton, I., "Calculation of Turbulent Boundary Layers over Flat Plates with Different Phenomenological Theories of Turbulence and Variable Turbulent Prandtl Number," Int. J. Heat and Mass Transfer, 16, 1973, 1547-1563.

31. Chung, P. M., "Performance of Turbulent Chemical Laser," AIAA J., 11, No. 7, 1040-1042.

32. Lorber, A. K. and Schetz, J. A., "Turbulent Mixing of Multiple, Co-Axial Helium Jets in a Supersonic Airstream," NASA CR-112292, March 1974.

Table 1

Sensitivity of Predictions to Various Parameters

A. Conditions Used in all Cases

q_r	1.0
d, in	.04
s/d	12.5
Distance from H_2 Injection Port to Opposite Wall	13.5 cm
Free Stream Mach Number	4.03
Stagnation Temperature (Primary), ^oK	300^o
Stagnation Temperature	300^o
Equivalence Ratio $(\dot{m}_{H_2}/\dot{m}_{air})/.0291$	< .01*
Type of Flow	Non Reacting

*Simulates H_2 Injection into an Infinite Air Stream

B. Purpose of Run

Case	Purpose
1-1	Evaluate mixing length theory
1-2	Double Discretization
1-3	Investigate effect of variations in turbulence constants λ and N_{Pr}^e
1-4	Evaluate effect of finite cross flow (u_3) velocity
1-5	Investigate effect of turbulent shear stress model using tensorial eddy viscosity
1-6	Evaluate two equation turbulence model
1-7	Evaluate turbulent Prandtl number model of ref. 30

Table 2

Data Used to Study Ability of Mixing Length Theory to Model H_2 Injection Data

A. Conditions Used in all Cases

Effective Prandtl Number	0.90
Equivalence Ratio	< 0.01
Free Stream Mach Number	4.03
Stagnation Temperature (H_2 and Air)	300°K
Type of Flow	Non Reacting

B. Cases Considered*

Case	q_r	s/d	Ref.
2-1	1	12.5	9
2-2	0.5	12.5	9
2-3	1.5	12.5	9
2-4	1.5	6.25	9
2-5	0.5	6.25	9
2-6	1.0	∞	8
2-7	0.5	∞	8
2-8	1.5	∞	8

*Note: Case q_r = 1.0, s/d = 6.25 not considered due to absence of symmetry in data.

Table 3a

Cases Used to Study (a) Virtual Source Concept (b) Reacting Flow (c) Ducted Flow†

Case	q_r	s/d	h/d	M_∞	ϕ	Mixing Model	Reaction Model*
3-1	1.0	12.5	∞	4.03	0.04	MLT	II (air)
3-2	1.0	12.5	∞	4.03	0.04	MLT	II (vitiated)
3-3**	-	8.93	10.0	2.25	0.60	MLT	II
3-4**	1.2	8.92	8.0	2.25	0.62	MLT	II
3-5	1.0	12.5	∞	4.03	0.04	k+d	I
3-6	1.0	12.5	∞	4.03	0.04	k+d	II
3-7	1.0	12.5	∞	4.03	0.04	k+d	III
3-8a	1.0	12.5	100	4.03	0.04	MLT	I
3-8b	1.0	12.5	100	4.03	0.04	MLT	II
3-9	1.0	12.5	18	4.03	0.50	MLT	II

†All cases used virtual source concept, cases 3-1 and 3-5 are non-reacting, cases 3-8 and 3-9 are ducted, all others have a free boundary.

*See Table 3b

**Case 3-3 is parallel injection from strut, case 3-4 is perpendicular injection; d is injector throat diameter (0.15 in. for 3-3, 0.187 for 3-4) otherwise d is sonic orifice diameter.

Table 3b

Reaction Models*

I.	Frozen Flow:	(a) H_2 + (b) O_2 → (a) H_2 + (b) O_2
II.A.	(b) ≥ (2a):	(a) H_2 + (b) O_2 → (a) H_2O + (b - $\frac{1}{2}$a) O_2
II.B.	(b) < (2a):	(a) H_2 + (b) O_2 → (2b) H_2O + (a - 2b) H_2
III.A.	(b) ≥ (2a):	(a) H_2 + (b) O_2 → (aR) H_2O + (b - $\frac{1}{2}$ aR) O_2 + (a(1-R)) H_2
III.B.	(b) < (2a):	(a) H_2 + (b) O_2 → (2bR) H_2O + (a - 2bR) H_2 + (b(1-R)) O_2

Notes: 1) ( ) represents number of moles

2) R is fraction of moles mixed on microscale and available for reaction

Table 4

Heat Flux Distribution at $x_1/d = 30$
for Virtual-Source Simulation*

x_3/d	Case 3-6 (Fully Reacted) $q_w/q_w)_r$	Case 3-7 (Rate Limited) $q_w/q_w)_r$
0	0.785	0.570
0.75	0.853	0.610
1.25	1.0	0.636
2.5	0.230	0.108
4.0	0.095	0.027
6.25	- 0.015	- 0.014

*Note:

(1) Fixed wall temperature, $T_w = 296.0^{\circ}K$

(2) $q_w)_r = 0.33$ Mw/m^2

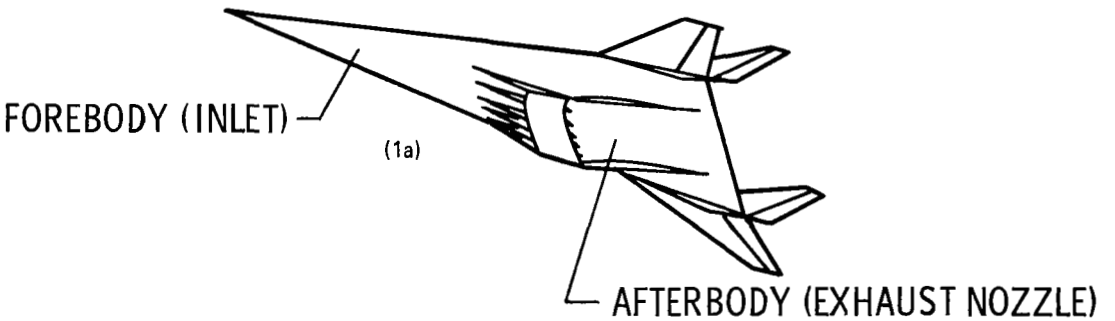

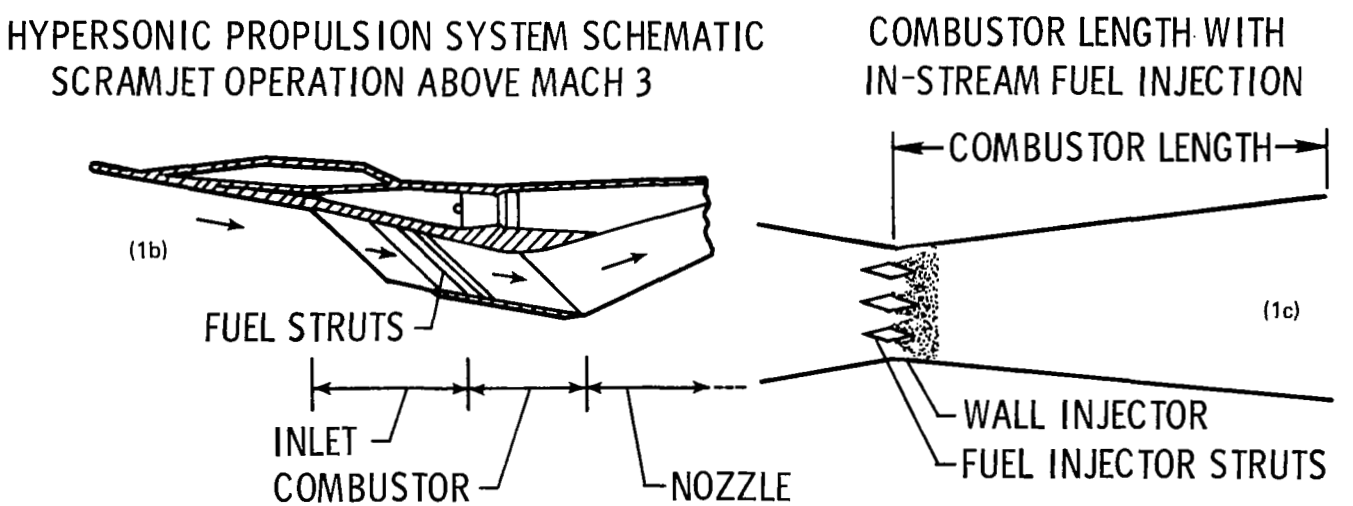

Figure 1. NASA Hypersonic Vehicle

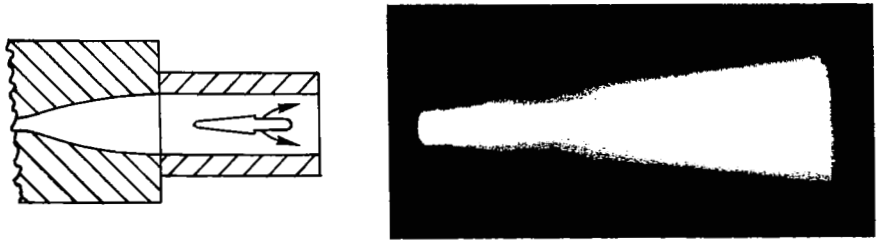

(a) Side view

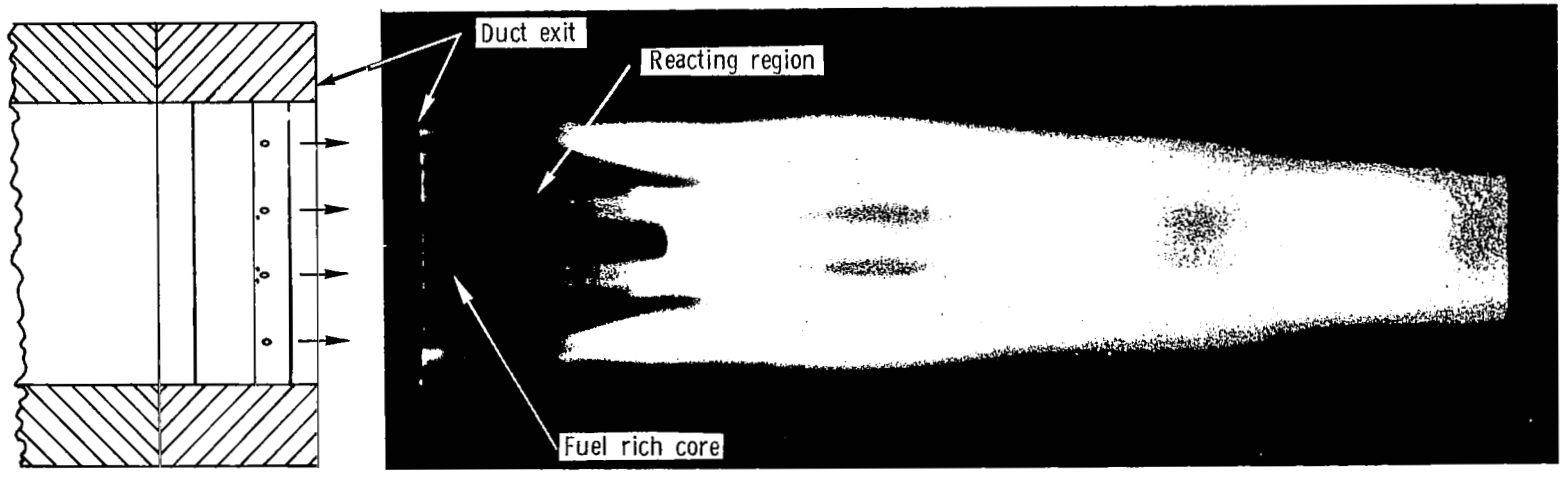

(b) Top view

Figure 2(a). Photographs of the Mixing-Reacting Flow Field of the Perpendicular-Injection Strut

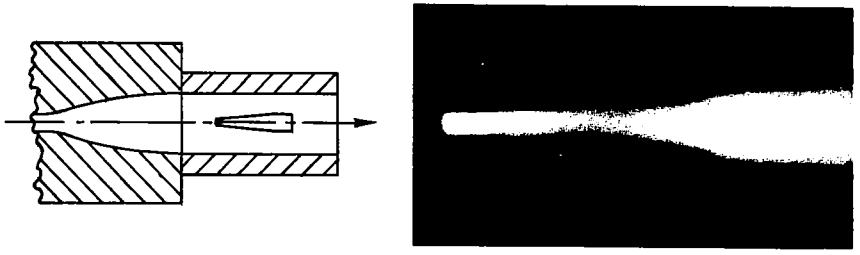

(a) Side view

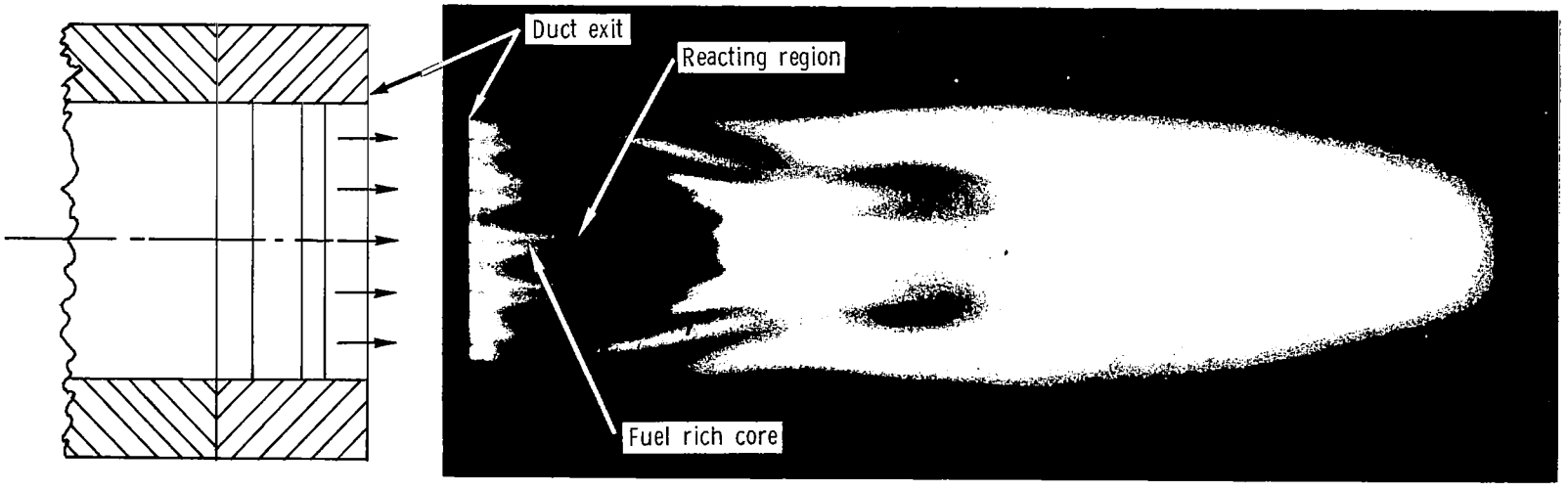

(b) Top view

Figure 2(b). Photographs of the Mixing-Reacting Flow Field of the Parallel Injection Strut

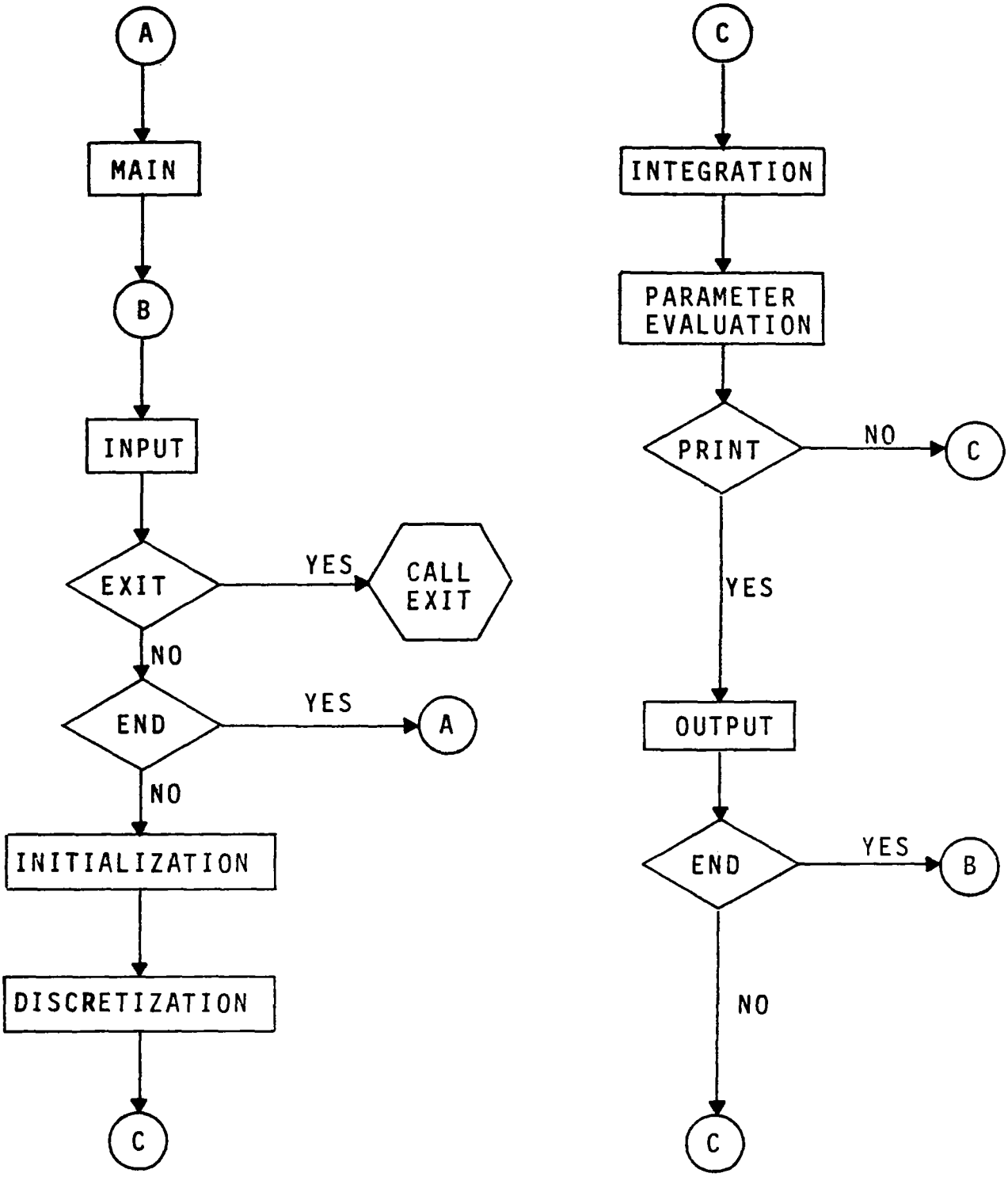

Figure 3. COMOC Macro-Structure

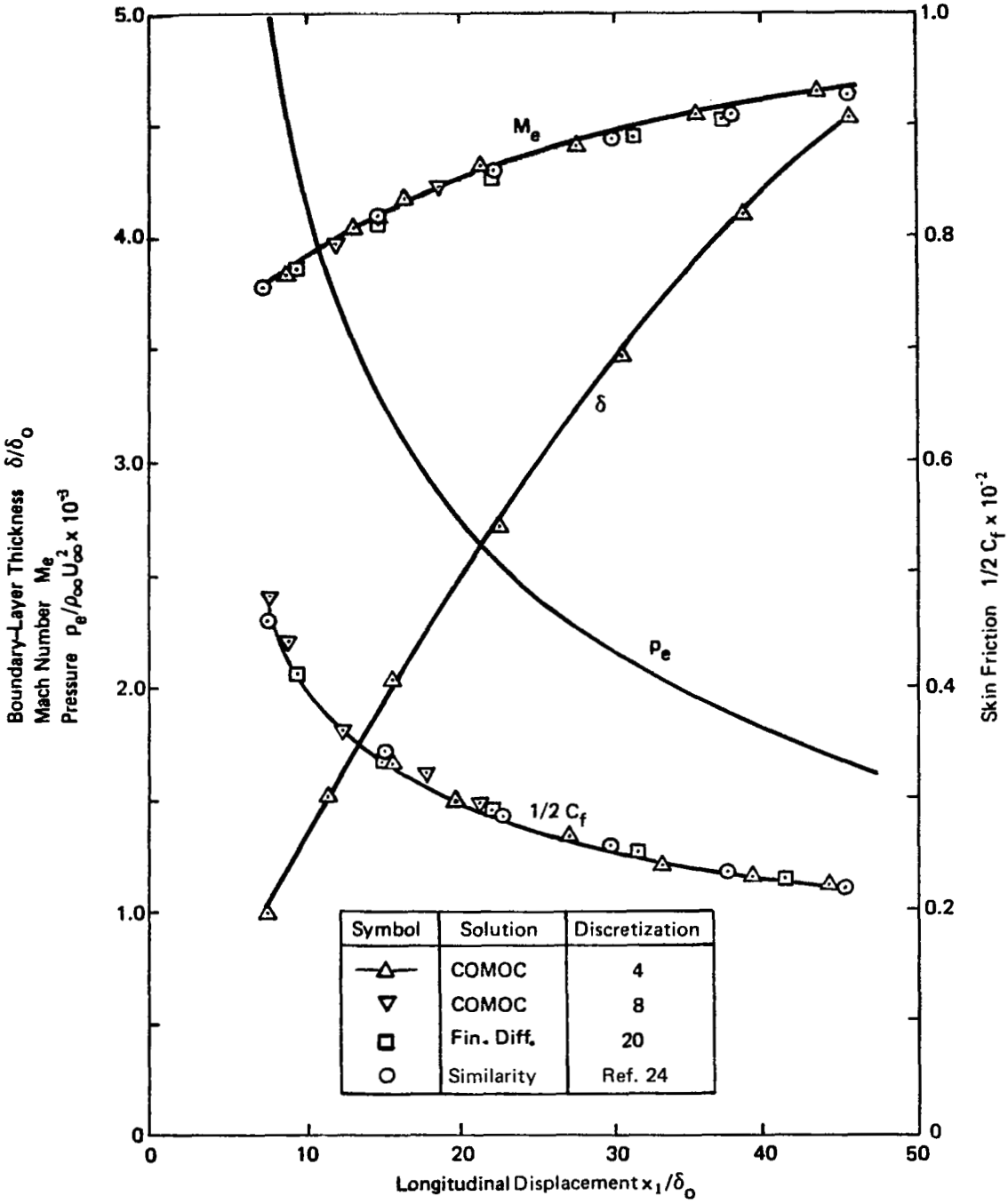

Figure 4. Computed Supersonic Boundary Layer Parameters, $M = 5$, $Re_x = 0.83(5)/m$, $\beta = 0.5$

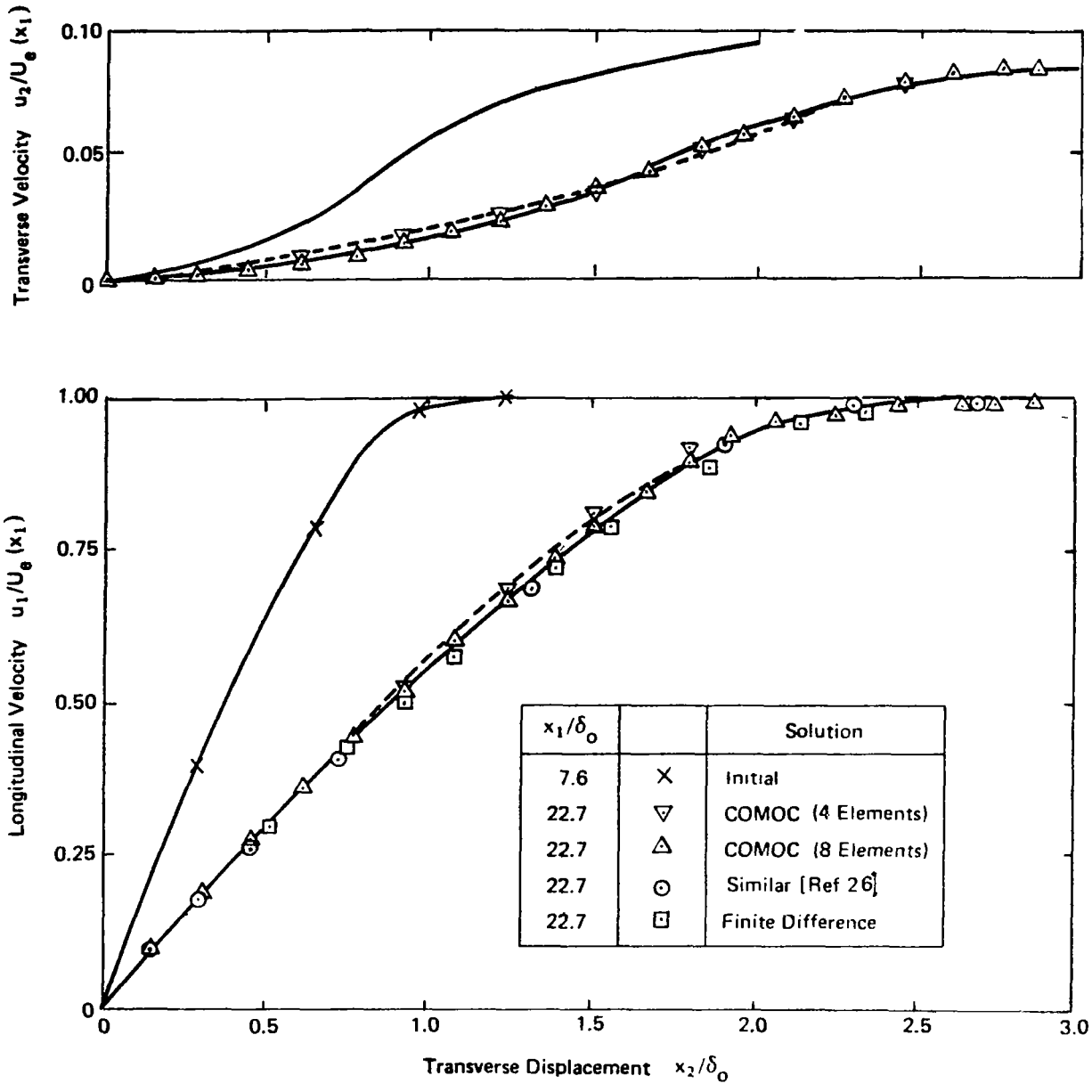

Figure 5. Computed Supersonic Boundary Layer Velocity M = 5, $Re_X = 0.83(5)/m$, $\beta = 0.5$

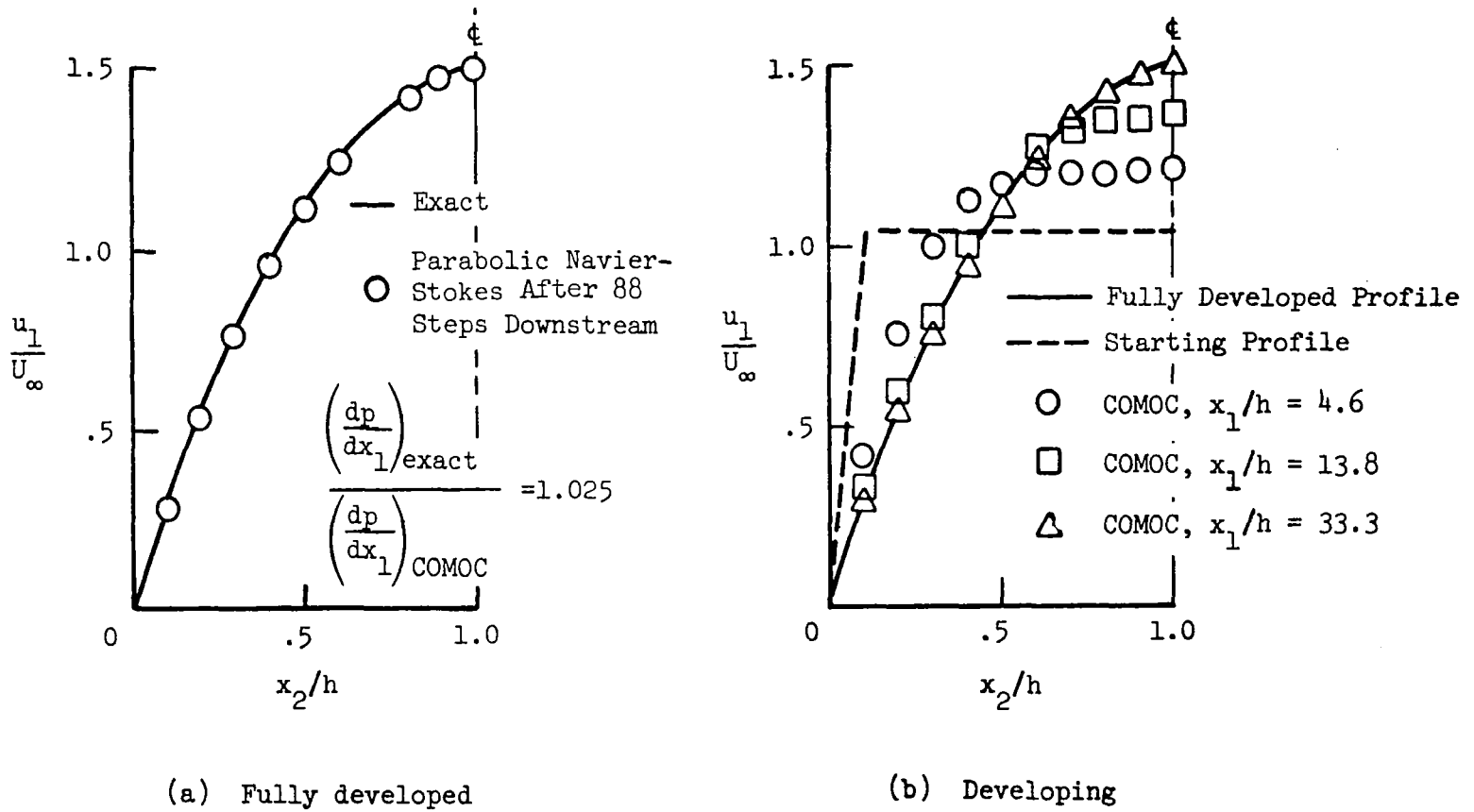

(a) Fully developed

(b) Developing

Figure 6. Channel Flow Solutions Computed with the Parabolic Navier-Stokes Variant Equations

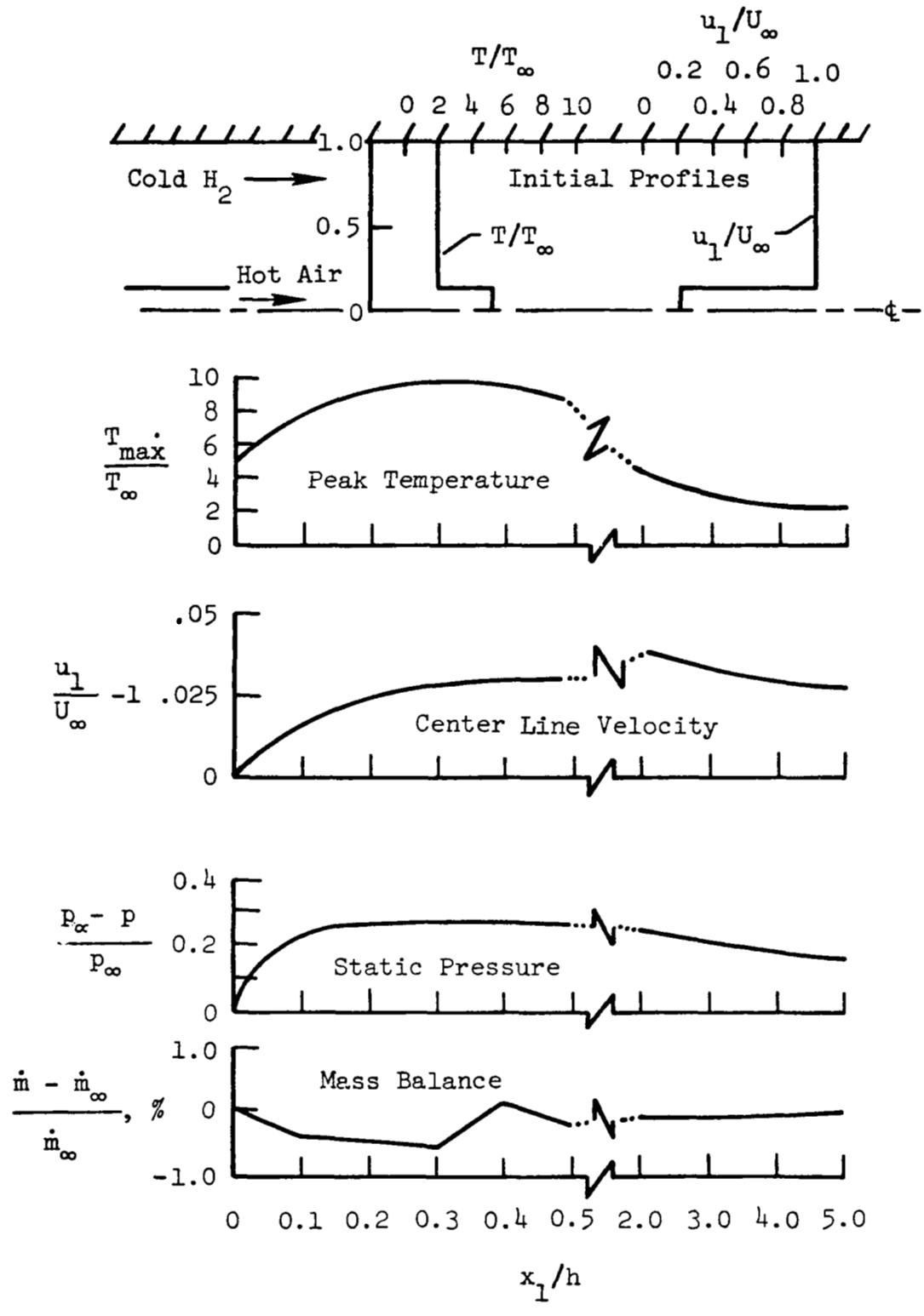

Figure 7. Mixing and Reacting Channel Flow. T_∞ = 400 K; U_∞ = 305 m/sec; h = 0.15 m

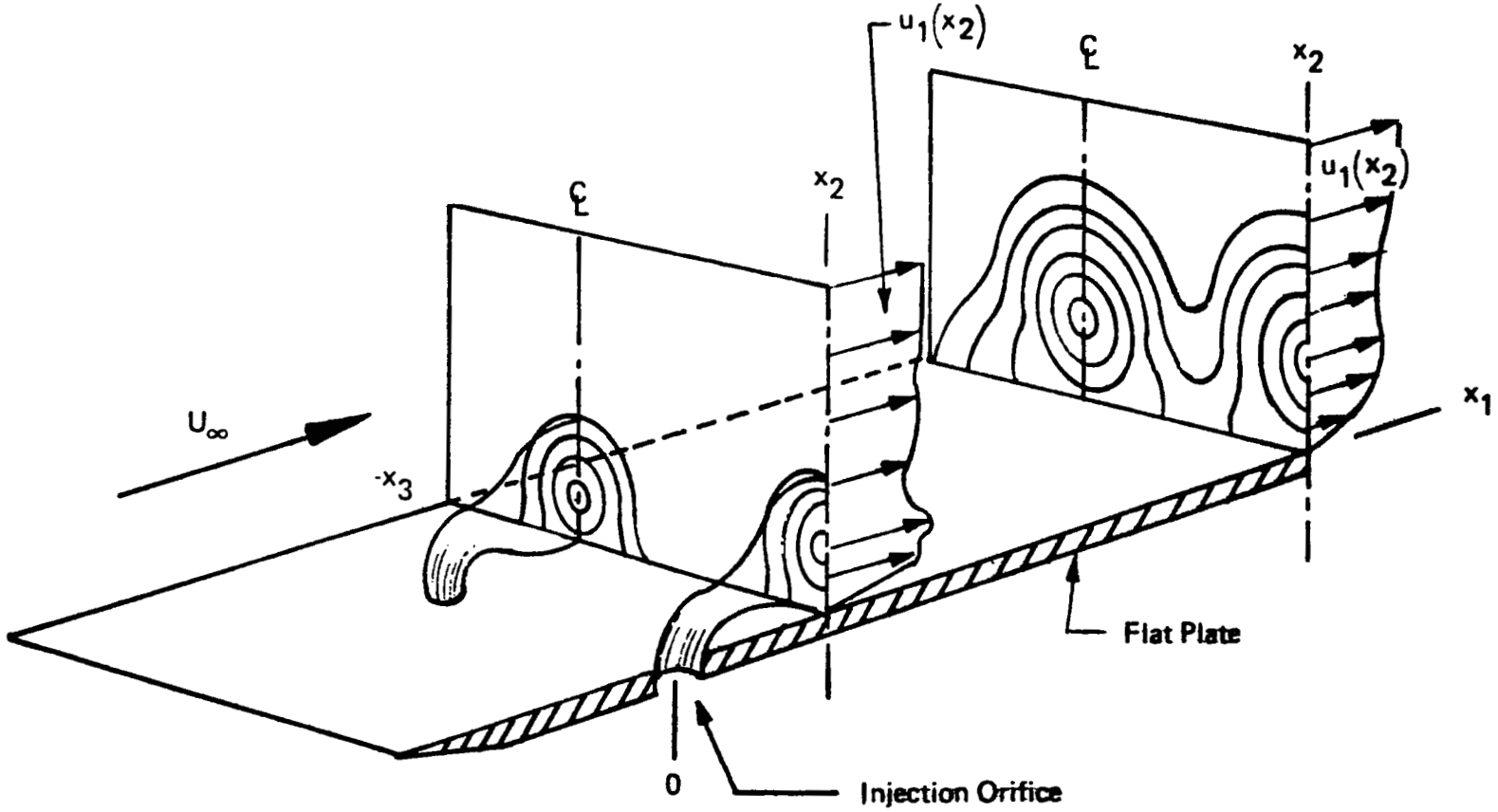

Figure 8. Three-Dimensional Flow Field Downstream of Transverse Injection from Discrete Orifices

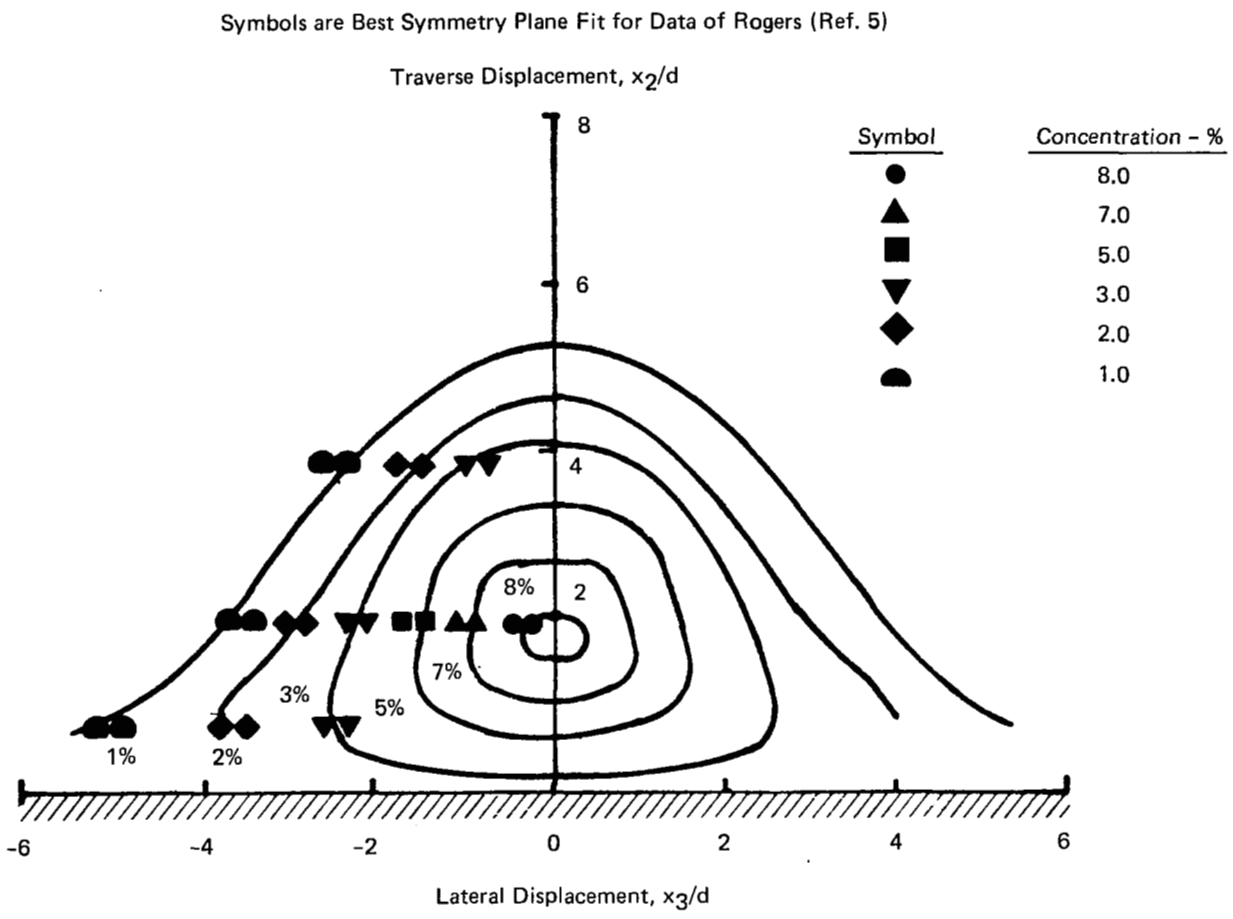

Figure 9. Cubic Spline Interpolated Hydrogen Mass Fraction Contours for Single-Jet, $q_r = 1.0$, $x/D = 30$

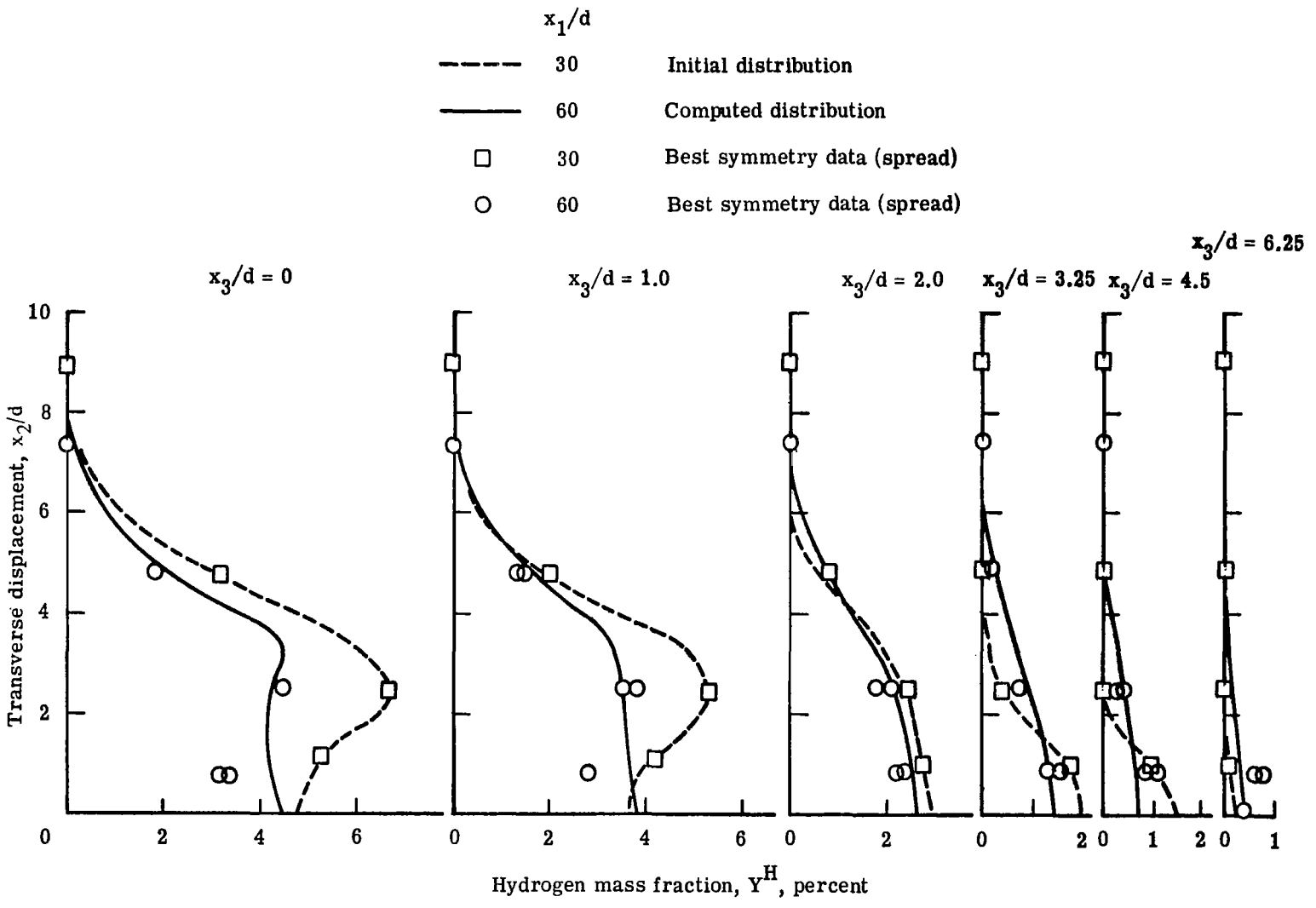

Figure 10. Comparison Between Experimental and Predicted H_2 Mass Fraction Profiles, Case 1-1.

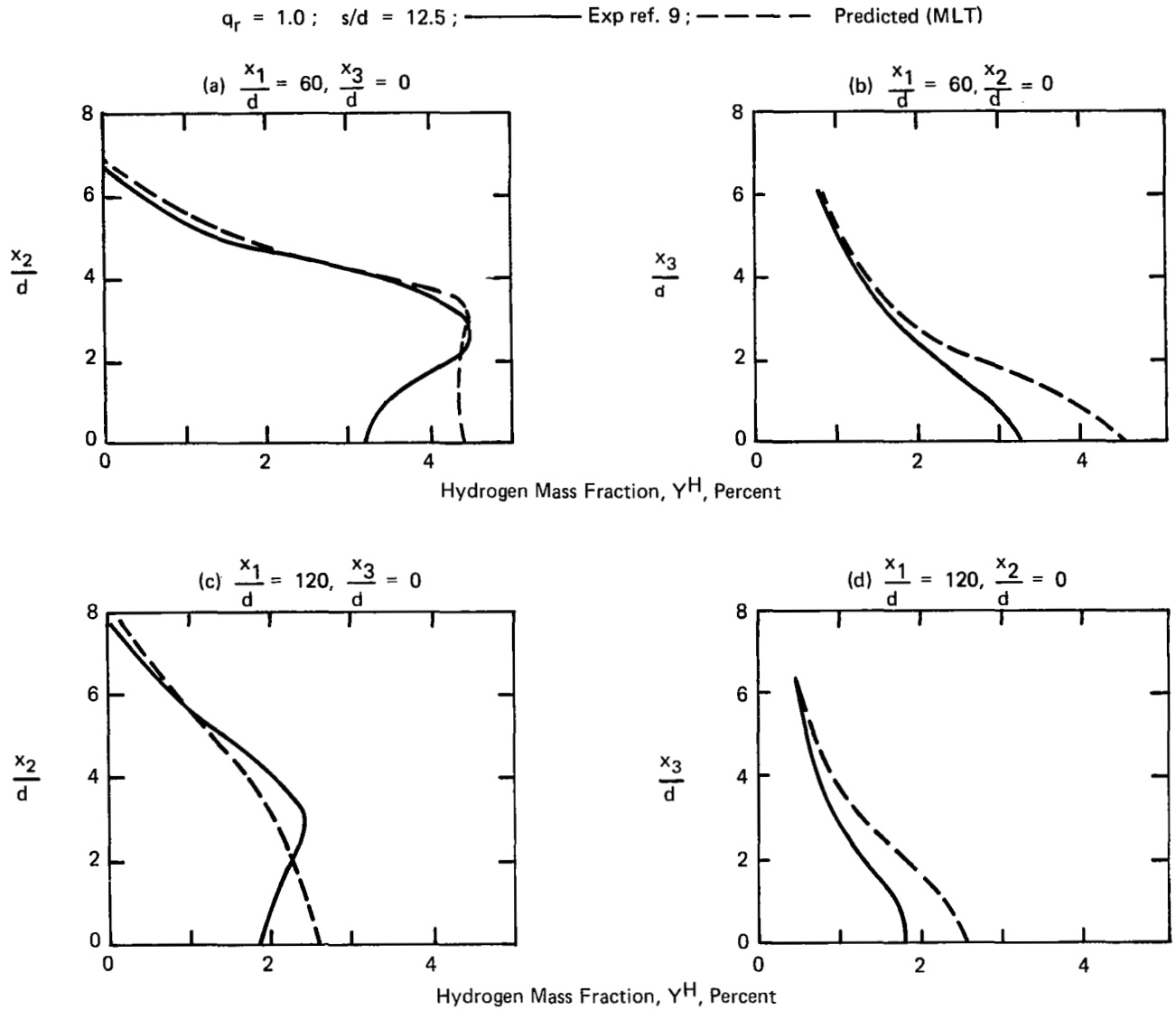

Figure 11. Comparison between Experimental and Predicted H_2 Mass Fraction Profiles, Case 1-1

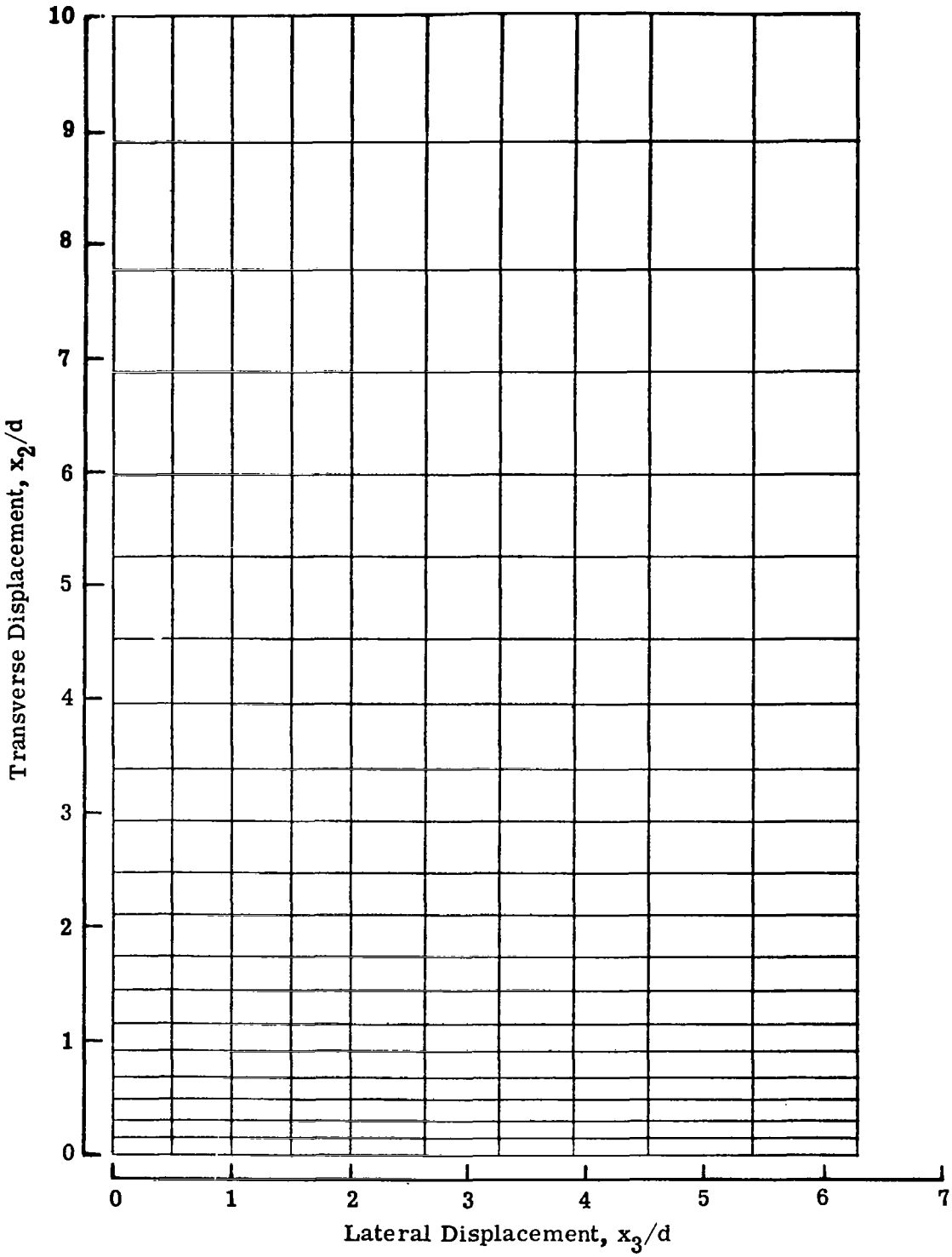

Figure 12. Finite Element Double Discretization of Injector Solution Domain

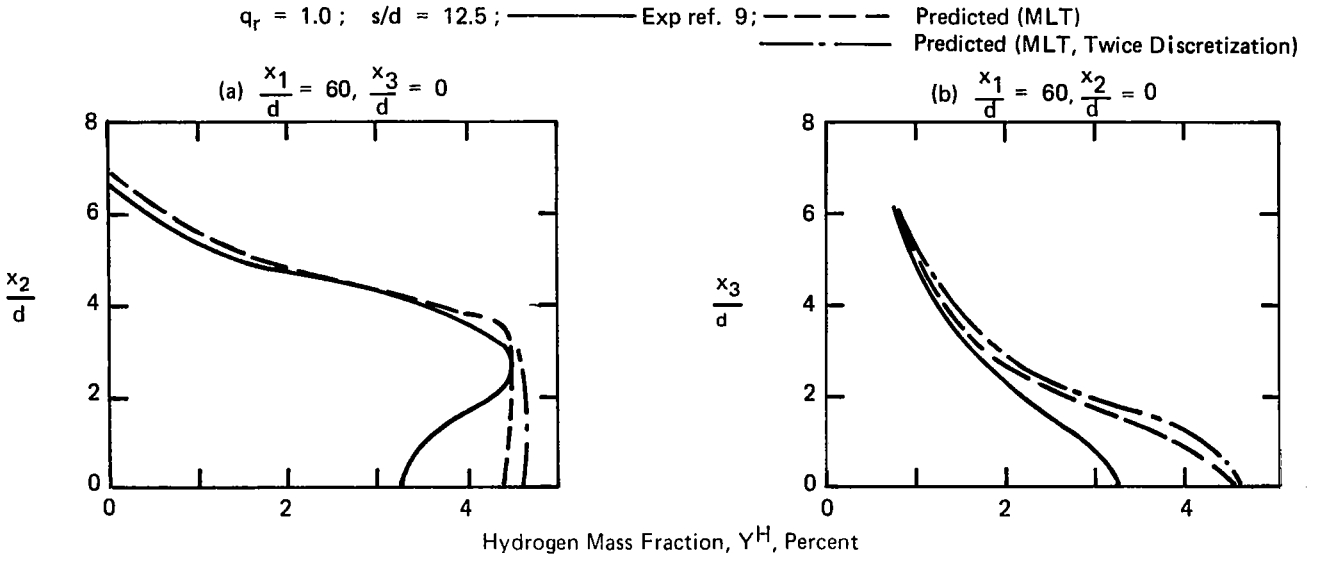

Figure 13. Comparison between Experimental and Predicted H_2 Mass Fraction Profiles along Center Plane ($x_3/d = 0$) and Wall ($x_2/d = 0$). Showing Effect of Doubling Discretization, Case 1-2

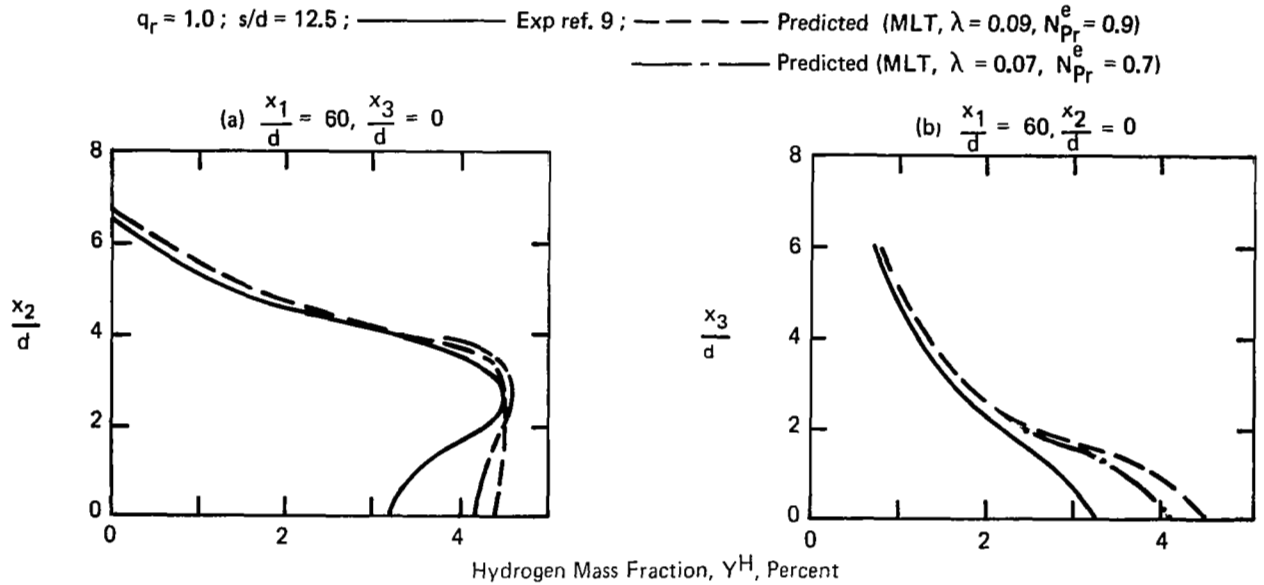

Figure 14. Comparison between Experimental and Predicted H_2 Mass Fraction Profiles along Center Plane ($x_3/d = 0$) and Wall ($x_2/d = 0$). Showing Sensitivity of Predictions to Turbulence Model Constants, Case 1-3

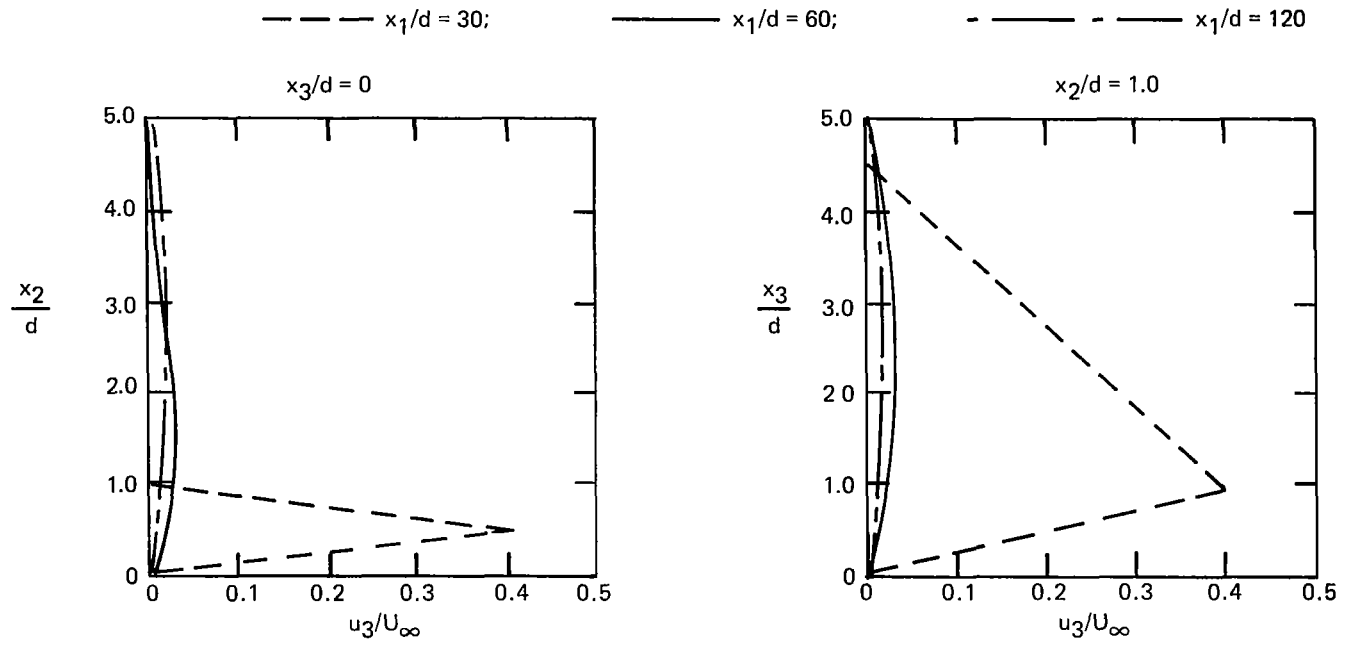

Figure 15. Initial Cross-Stream Velocity Distribution ($x_1/d = 30$) and Computed Distributions at $x_1/d = 60$ and 120

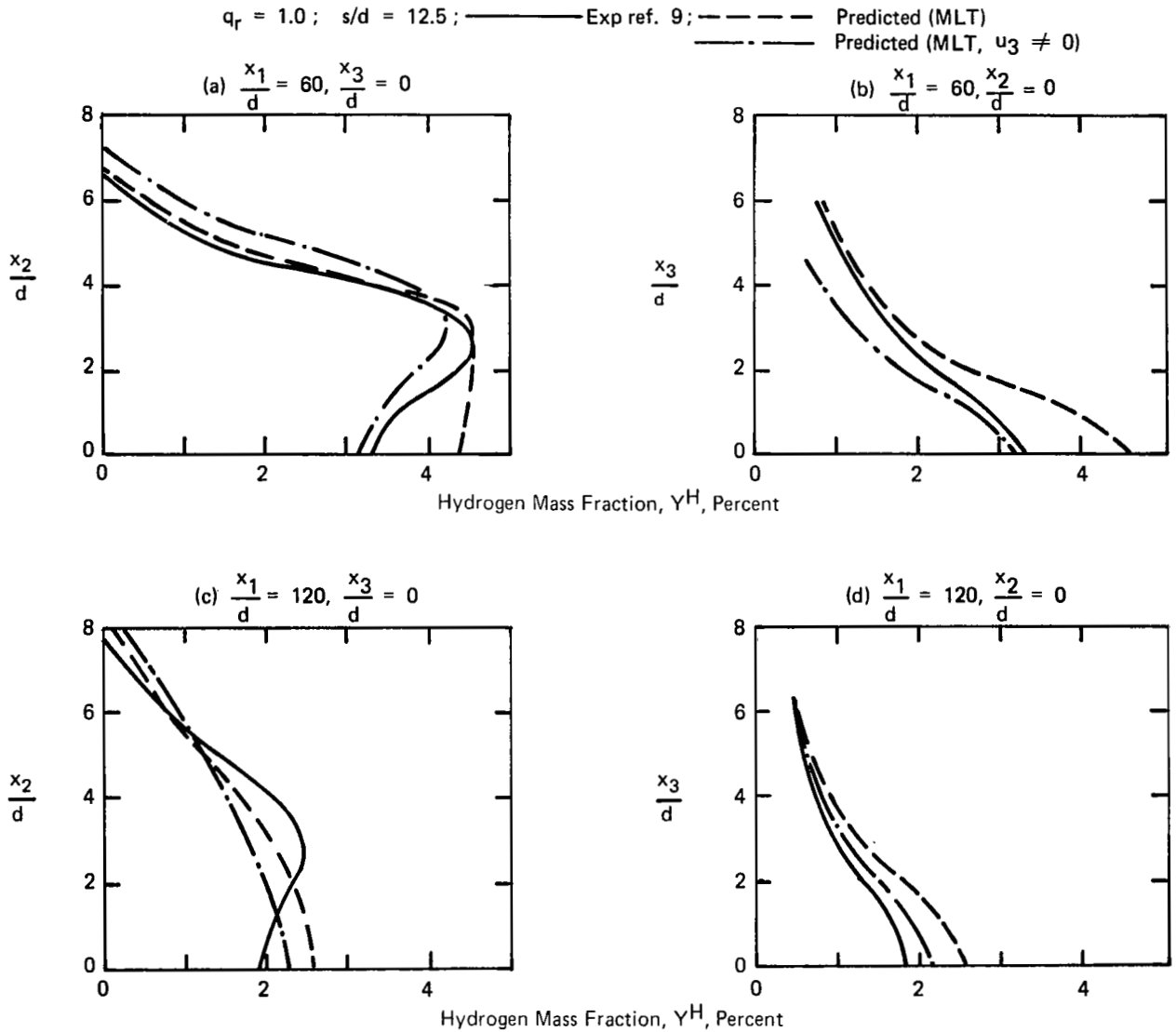

Figure 16. Comparison between Experimental and Predicted H_2 Mass Fraction Profiles along Center Plane ($x_3/d = 0$) and Wall ($x_2/d = 0$). Showing Effect of Including Transverse Velocity, u_3, Case 1-4

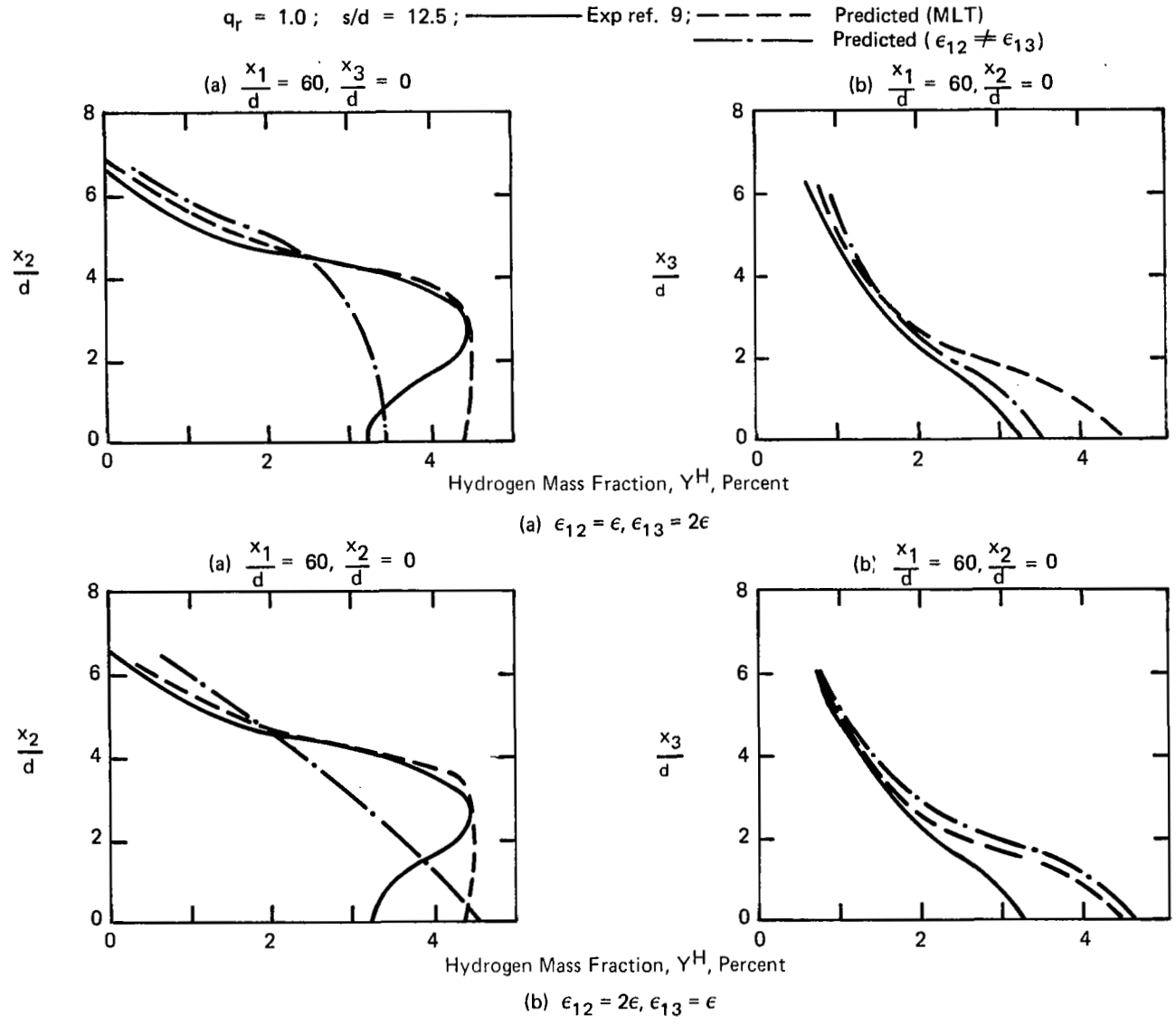

Figure 17. Comparison between Experimental and Predicted H_2 Mass Fraction Profiles along Center Plane ($x_3/d = 0$) and Wall ($x_2/d = 0$). Showing Effect of Tensorial Eddy Viscosity, Case 1-5

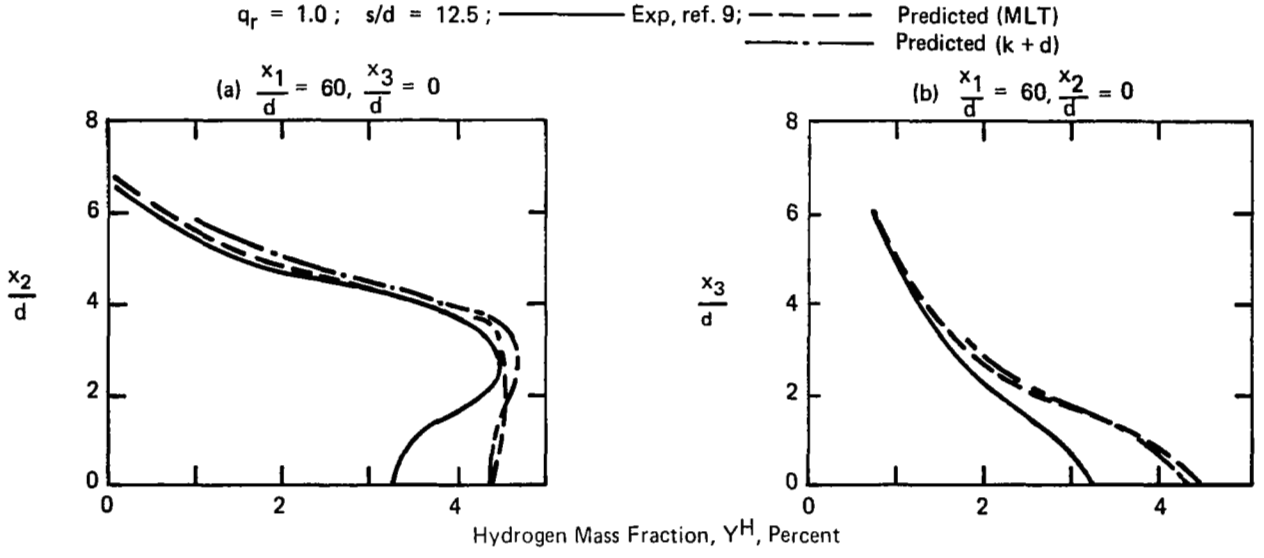

Figure 18. Comparison between Experimental and Predicted H_2 Mass Fraction Profiles along Center Plane ($x_3/d = 0$) and Wall ($x_2/d = 0$), using 2 Equation Turbulence Model, Case 1-6

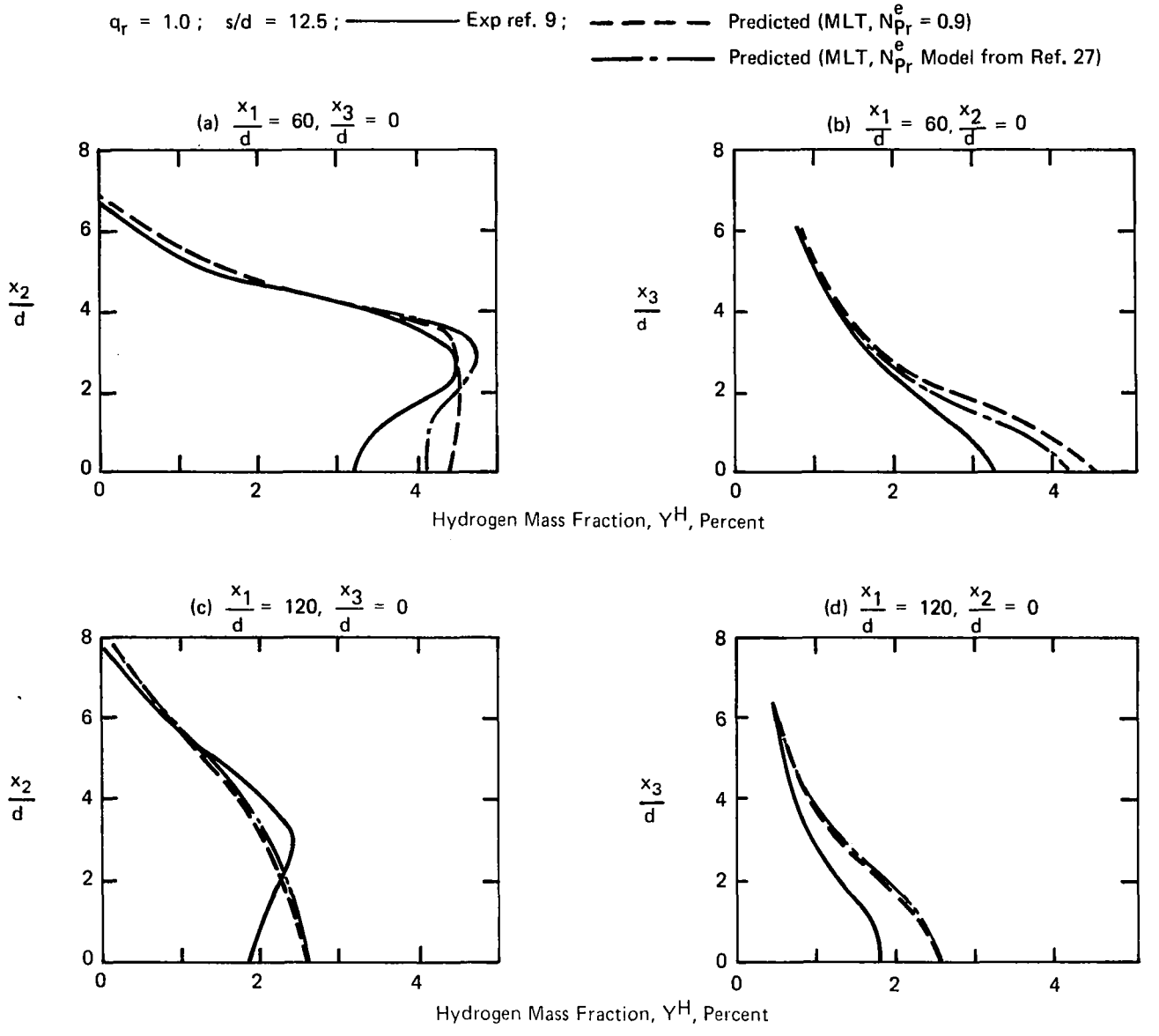

Figure 19. Comparison between Experimental and Predicted H_2 Mass Fraction Profiles along Center Plane ($x_3/d = 0$) and Wall ($x_2/d = 0$). Case 1-7: MLT, N^e_{Pr} Model from Ref. 27

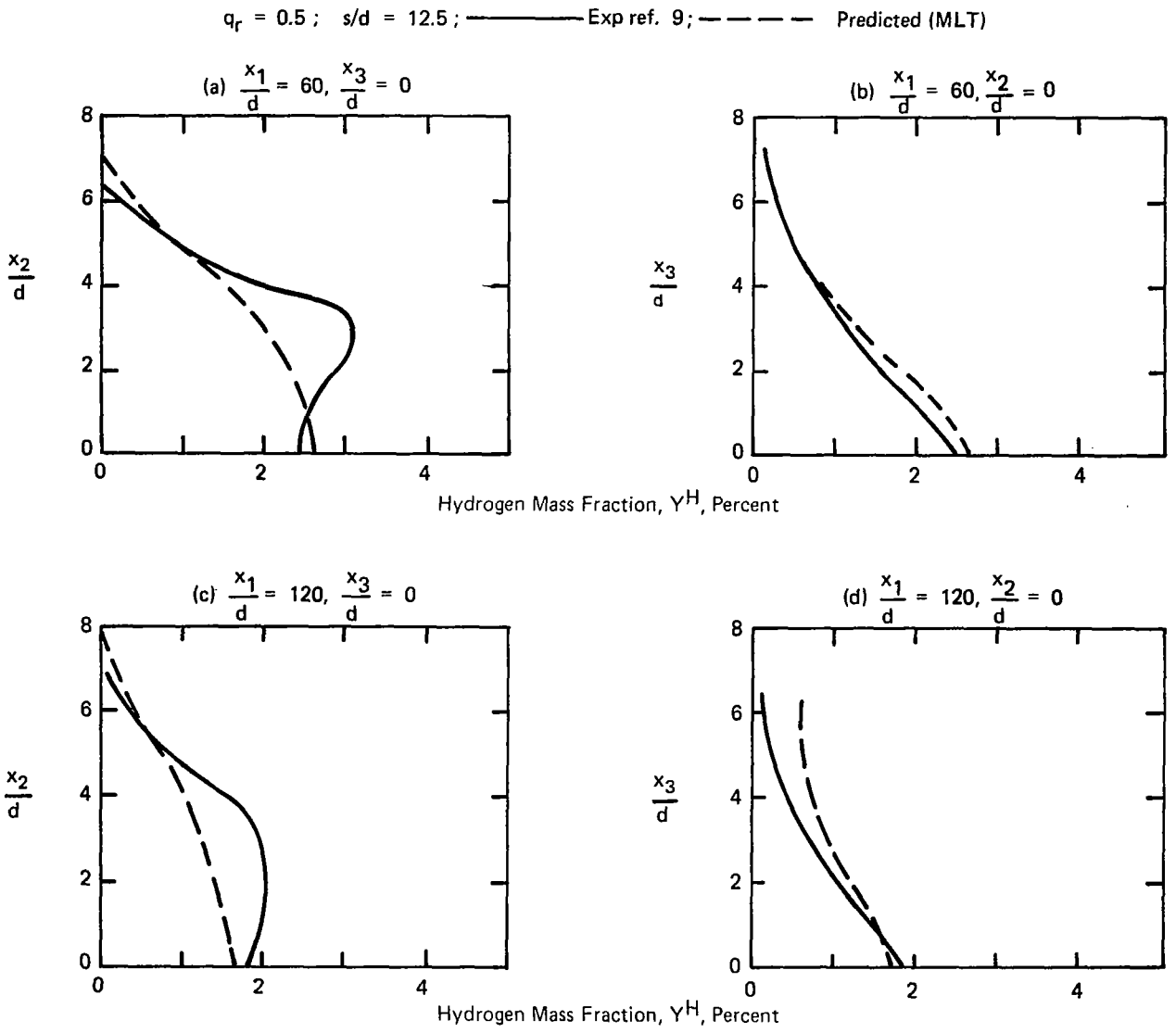

Figure 20. Comparison between Experimental and Predicted H_2 Mass Fraction Profiles along Center Plane ($x_3/d = 0$) and Wall ($x_2/d = 0$). Case 2-2, MLT, $N^e_{Pr} = 0.9$

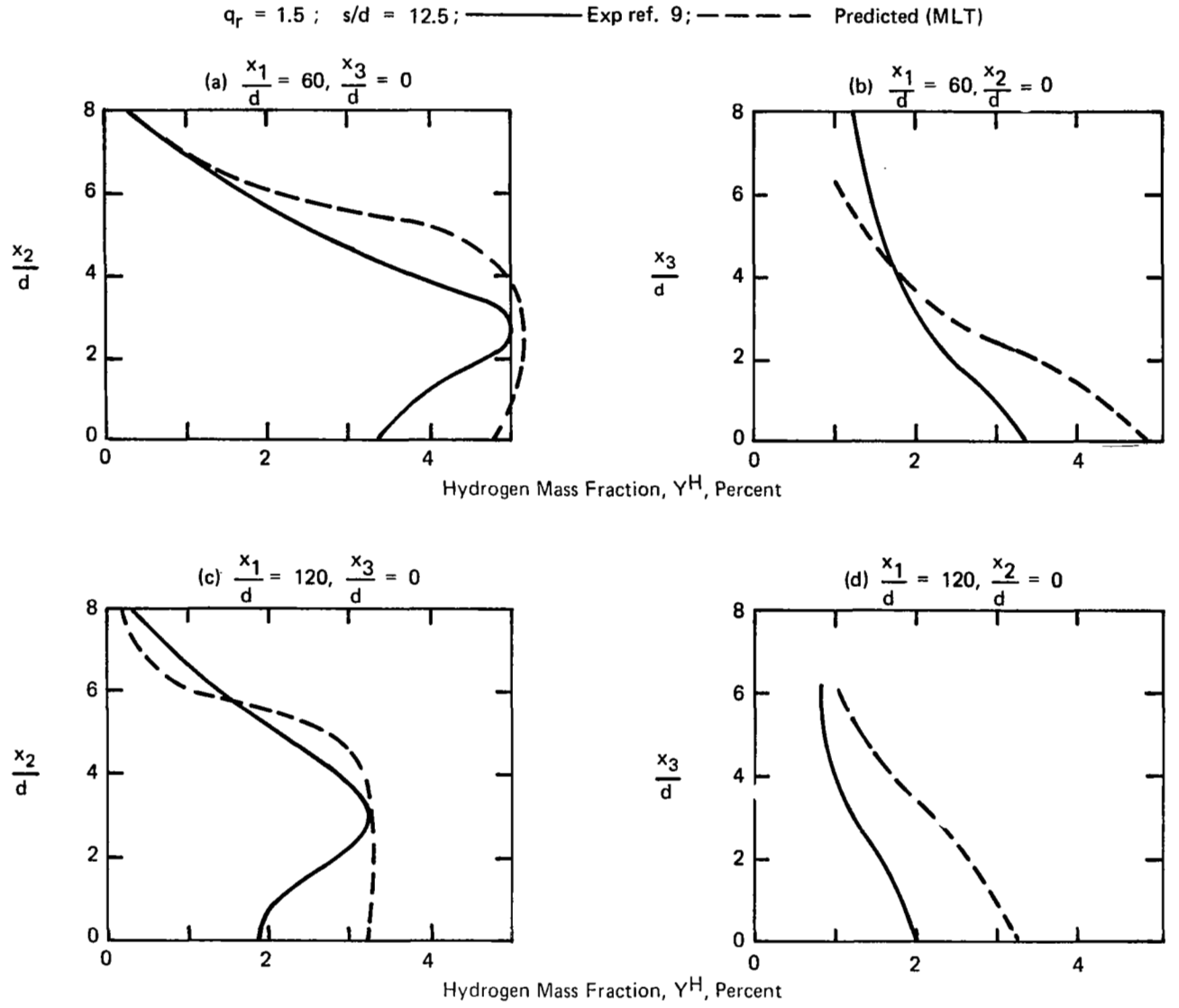

Figure 21. Comparison between Experimental and Predicted H_2 Mass Fraction Profiles along Center Plane ($x_3/d = 0$) and Wall ($x_2/d = 0$). Case 2-3, MLT, $N^e_{Pr} = 0.9$

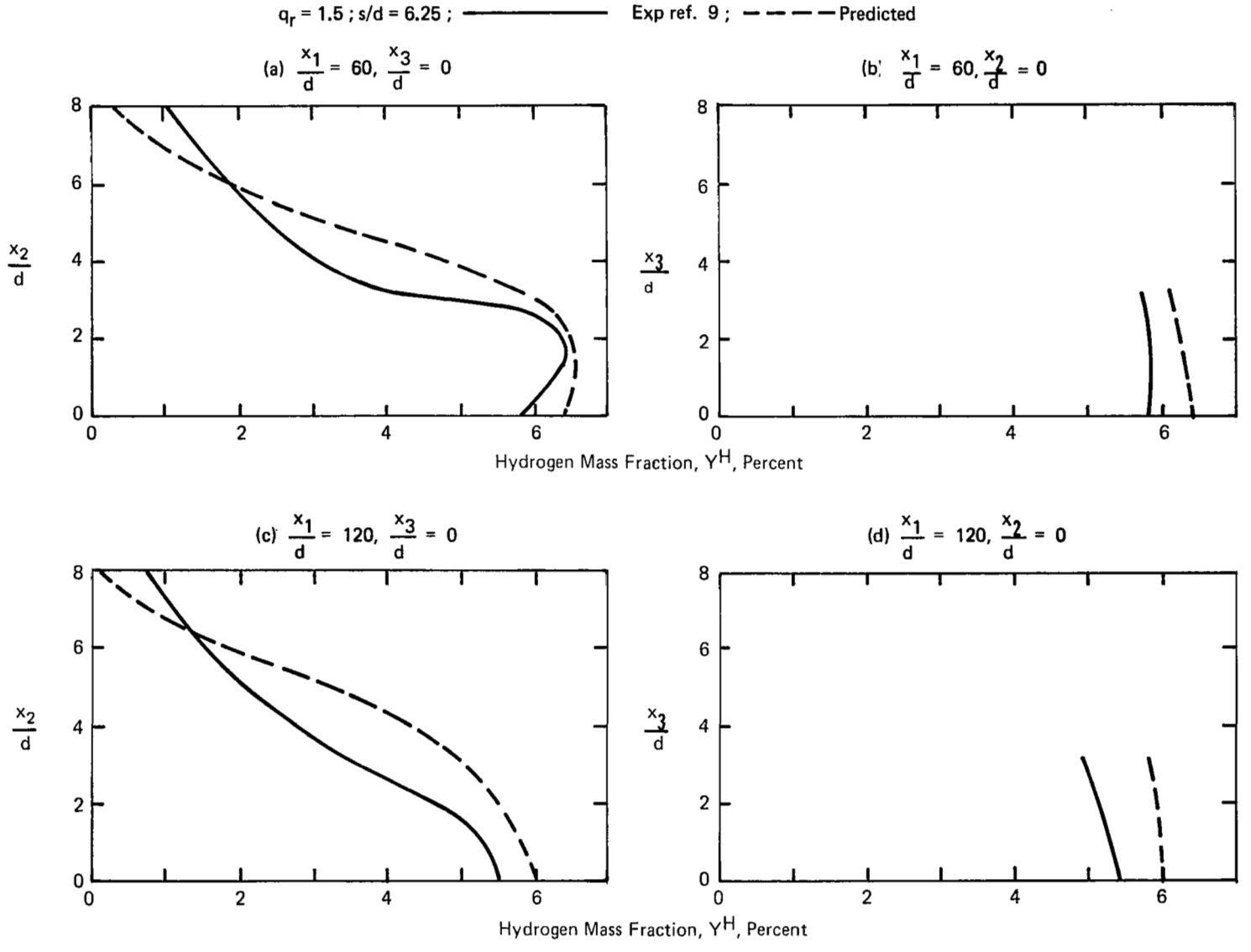

Figure 22. Comparison between Experimental and Predicted H_2 Mass Fraction Profiles along Center Plane ($x_3/d = 0$) and Wall ($x_2/d = 0$). Case 2-4, MLT, $N^e_{Pr} = 0.9$

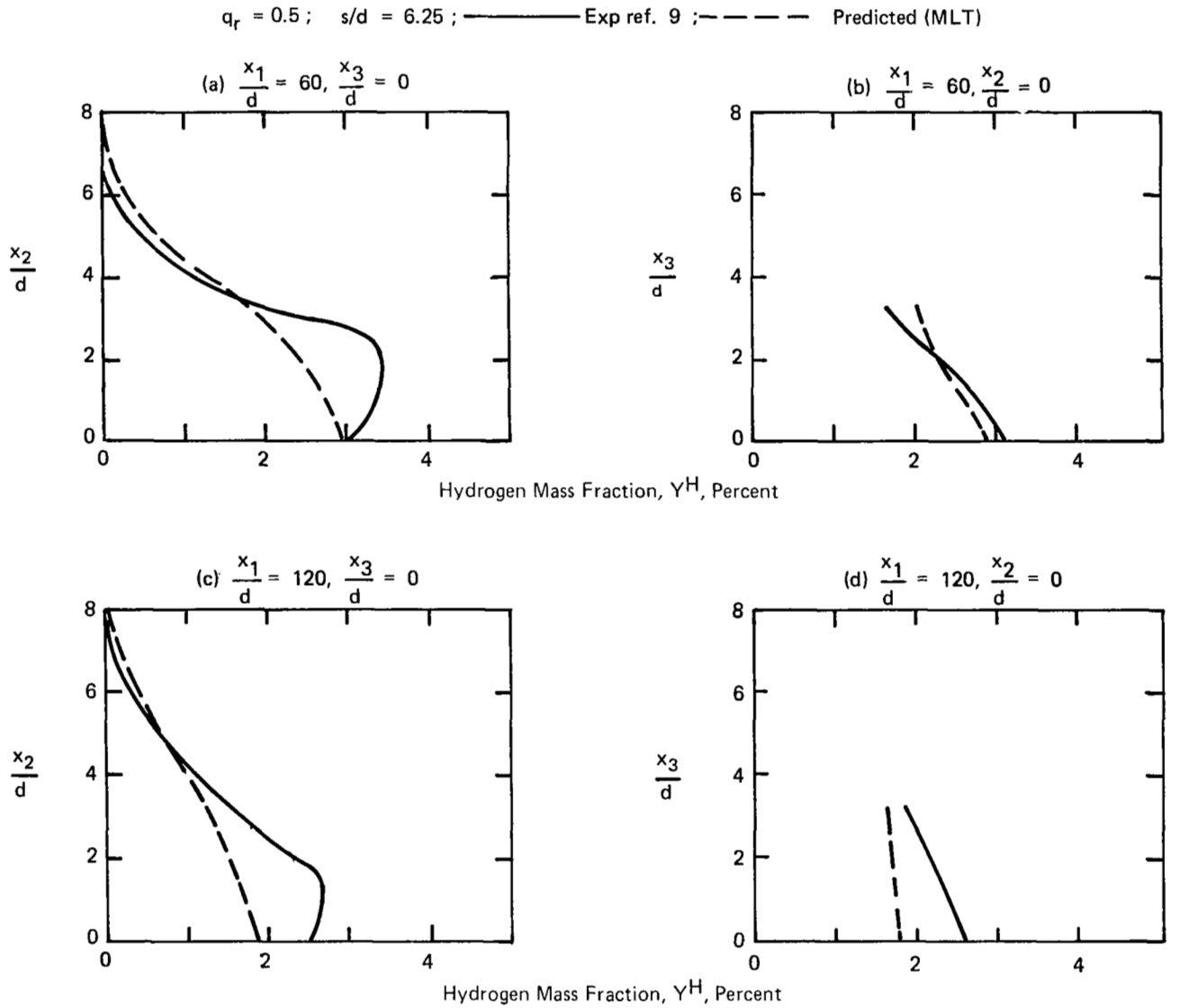

Figure 23. Comparison between Experimental and Predicted H_2 Mass Fraction Profiles along Center Plane ($x_3/d = 0$) and Wall ($x_2/d = 0$). Case 2-5, MLT, $N^e_{Pr} = 0.9$

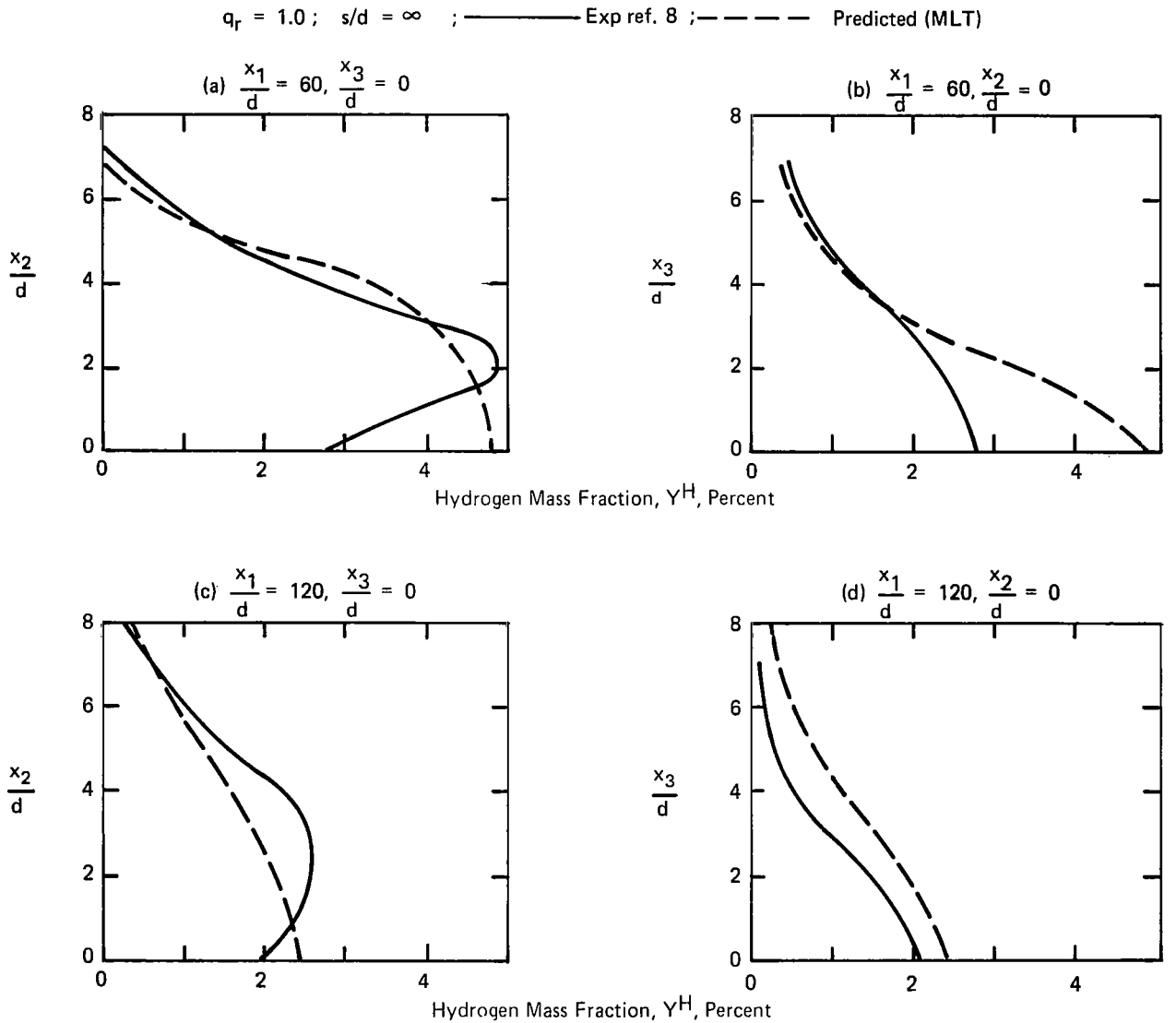

Figure 24. Comparison between Experimental and Predicted H_2 Mass Fraction Profiles along Center Plane ($x_3/d = 0$) and Wall ($x_2/d = 0$). Case 2-6, MLT, $N^e_{Pr} = 0.9$

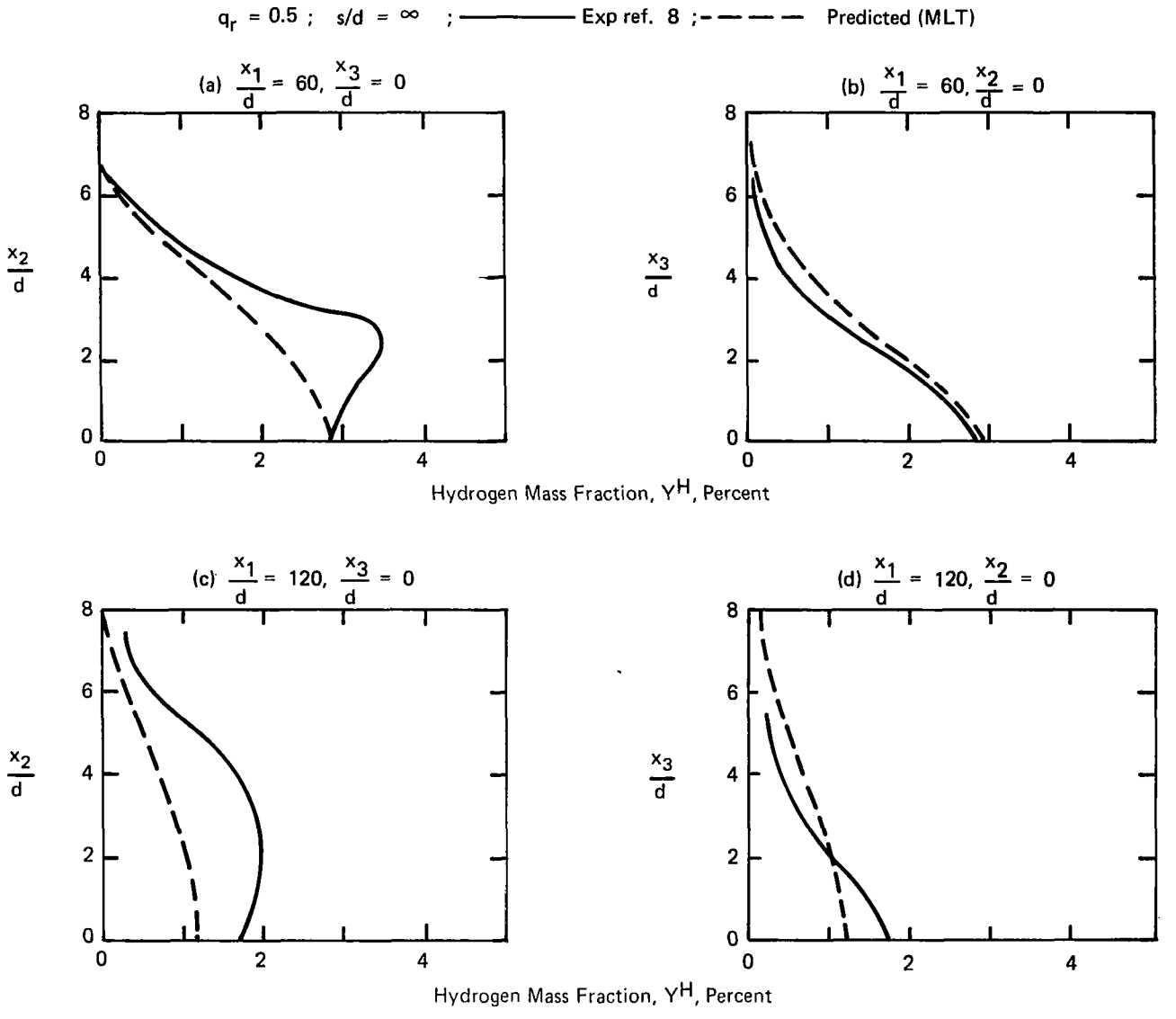

Figure 25. Comparison between Experimental and Predicted H_2 Mass Fraction Profiles along Center Plane ($x_3/d = 0$) and Wall ($x_2/d = 0$). Case 2-7, MLT, $N^e_{Pr} = 0.9$

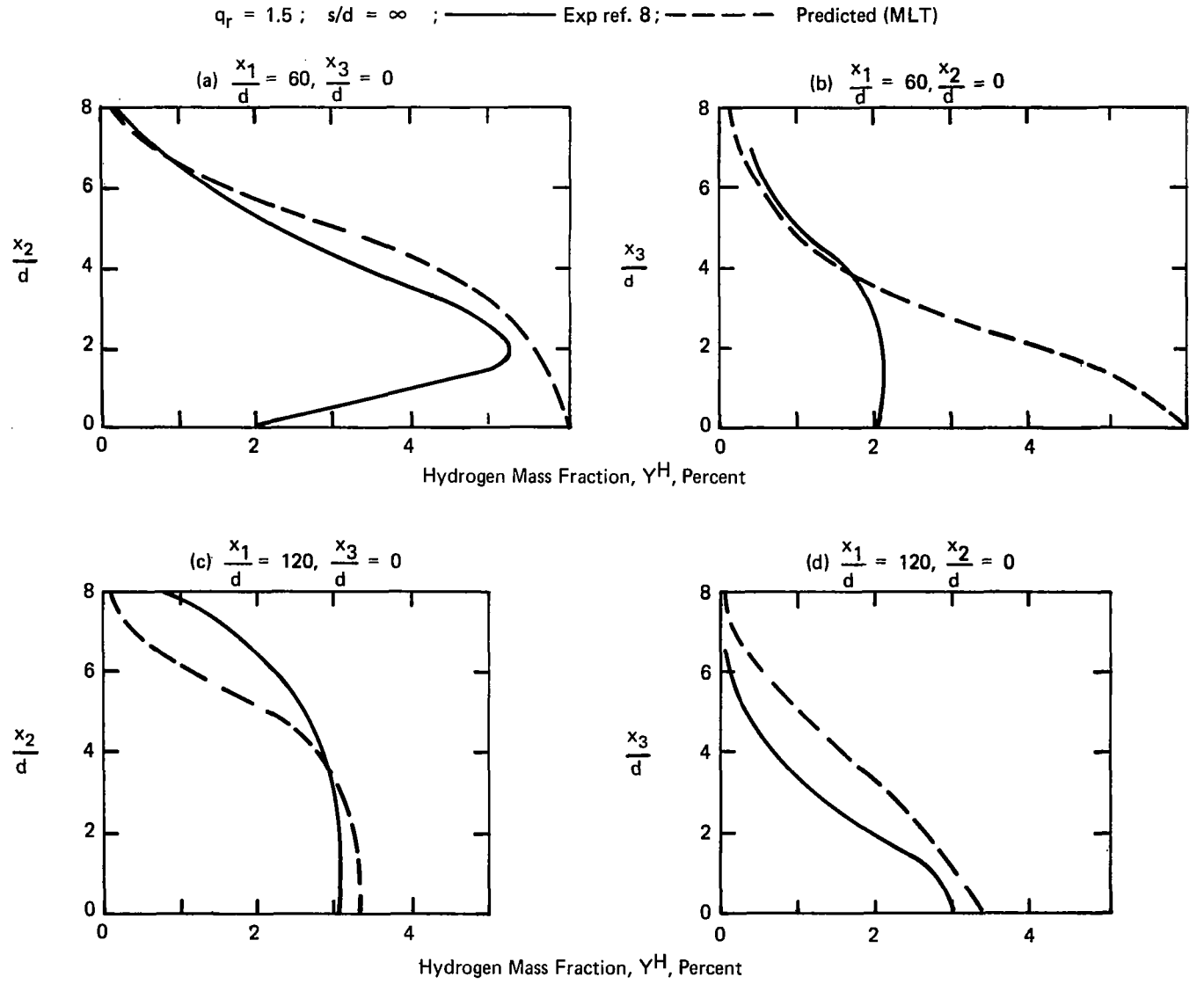

Figure 26. Comparison between Experimental and Predicted H_2 Mass Fraction Profiles along Center Plane ($x_3/d = 0$) and Wall ($x_2/d = 0$). Case 2-8, MLT, $N^e_{Pr} = 0.9$

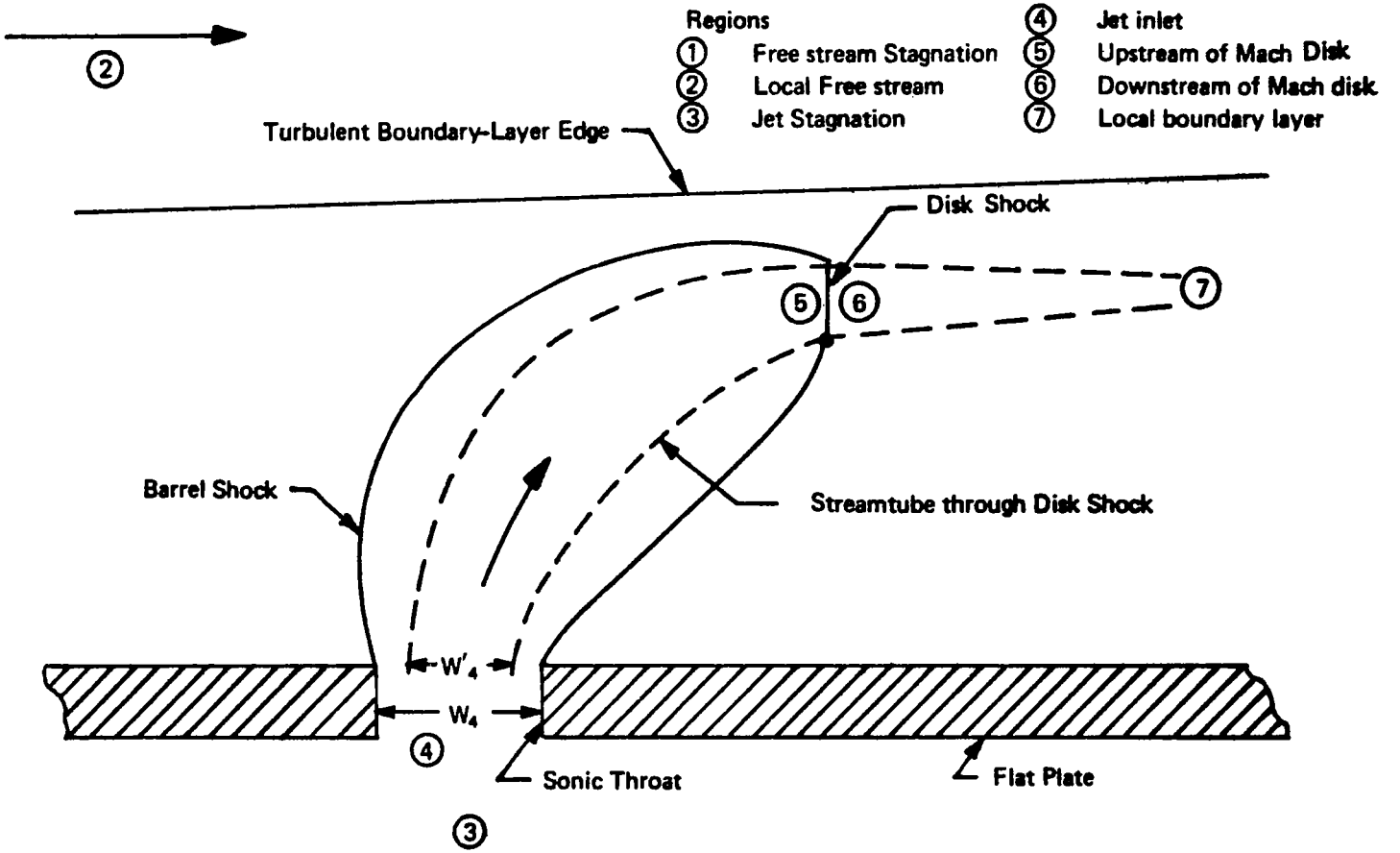

Figure 27. Transverse Injection into a Turbulent Boundary Layer

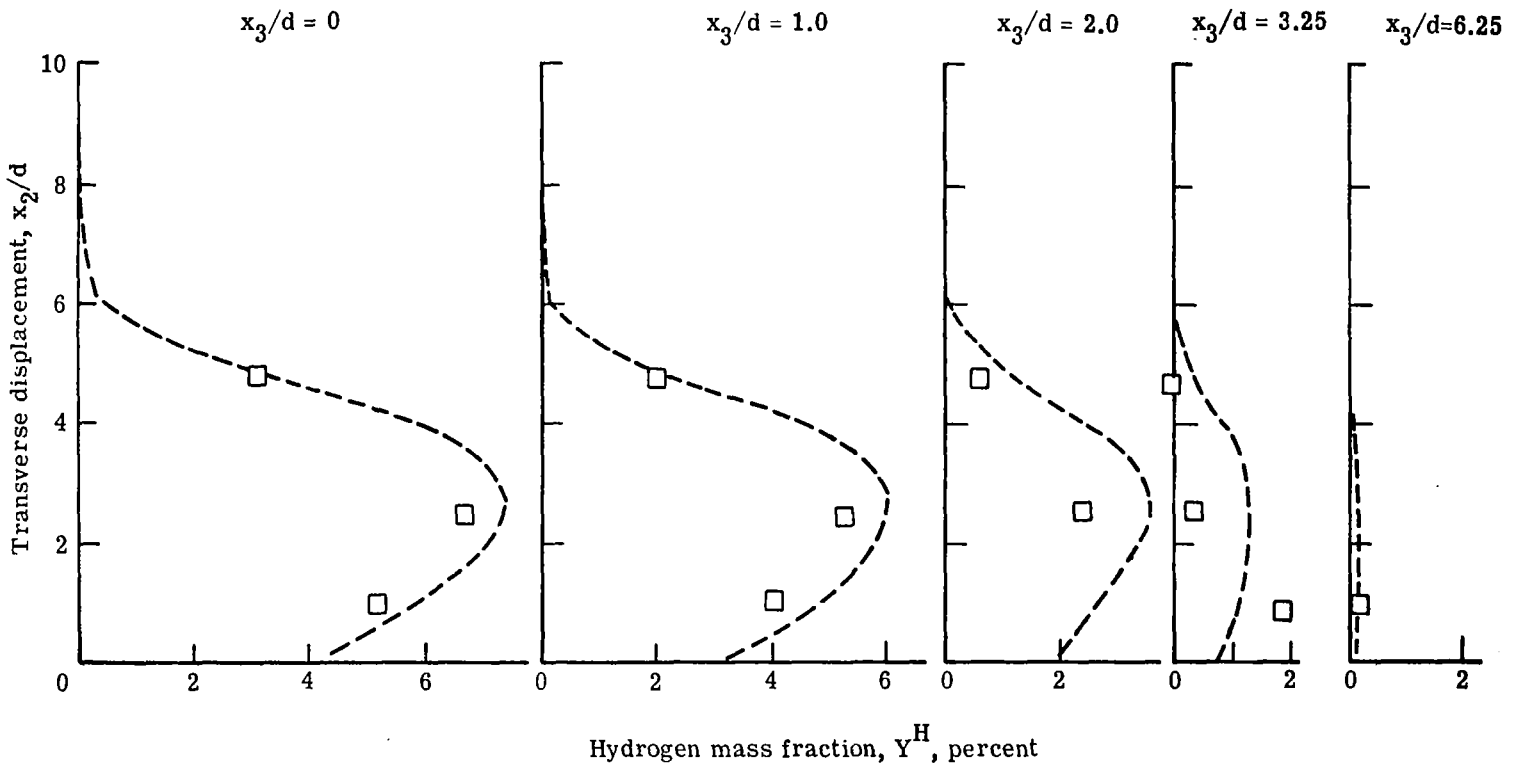

Figure 28. Comparisons between Experimental and Predicted H_2 Mass Fraction Profiles at x_1/d = 30 and Various x_3/d Stations. Virtual-Source Concepts used to Start Calculations at x_1/d = 0

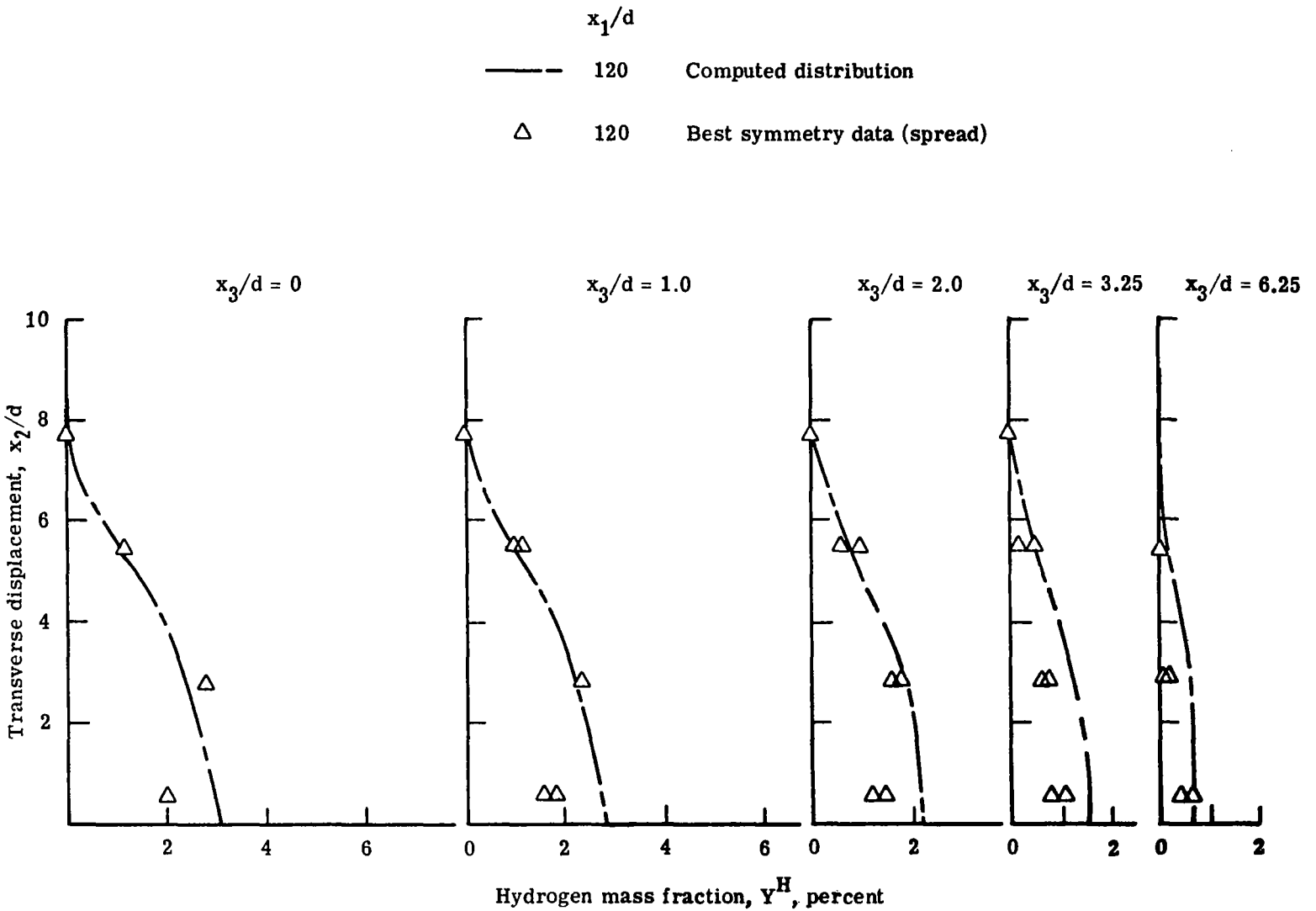

Figure 29. Comparisons between Experimental and Predicted H_2 Mass Fraction Profiles at x_1/d = 120 and Various x_3/d Stations. Virtual-Source Concept used to Start Calculations at x_1/d = 0

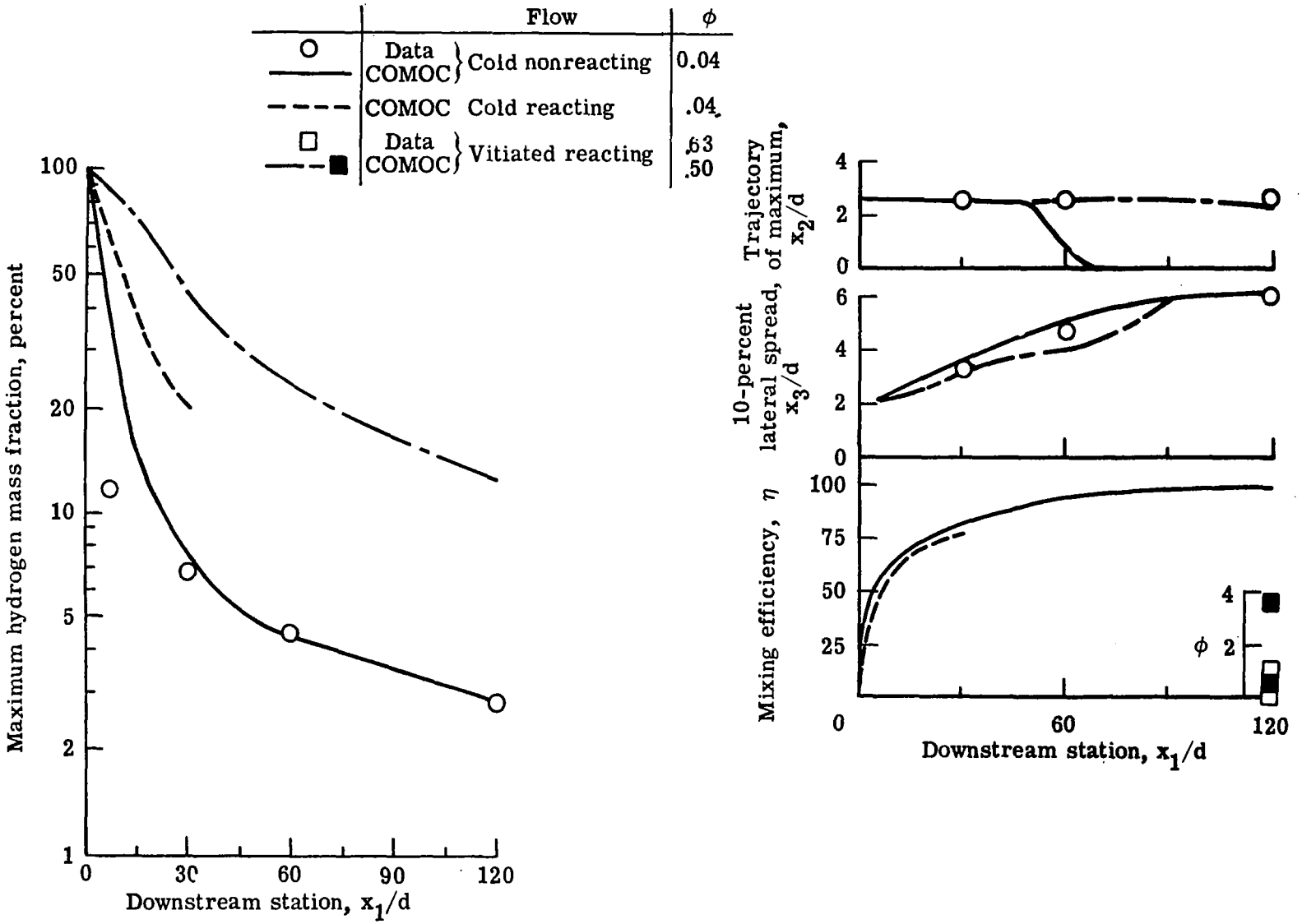

Figure 30. Transverse Cold Hydrogen Injection with Virtual-Source Simulation ($q_r = 1.0$; s/d = 12.5 of Reference 9). Vitiated Reacting Flow Data of Reference 10 does not Exactly Correspond to these Conditions since $q_r = 1.26$, s/d = 10.5, $\phi = 0.63$

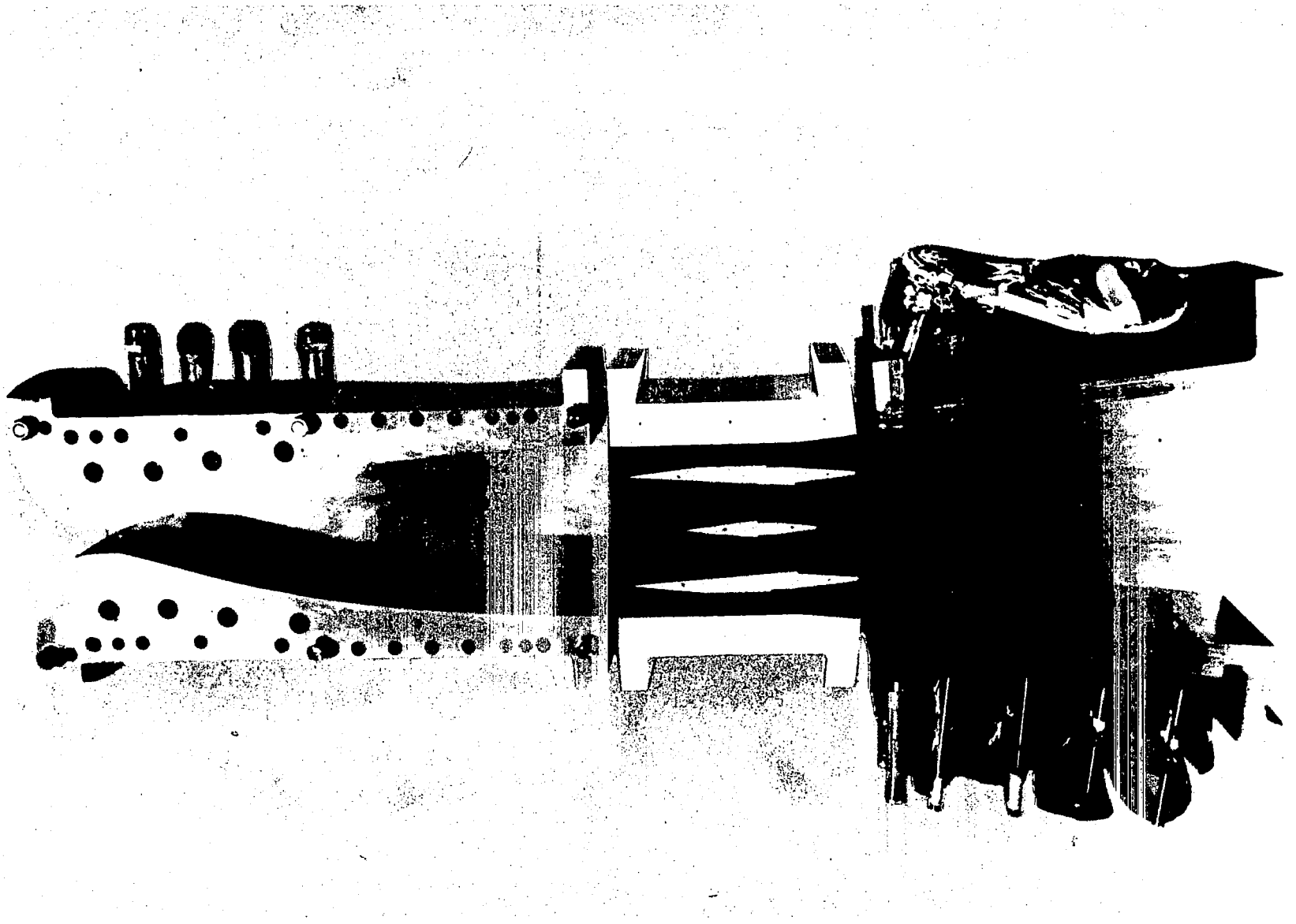

Figure 31. Scramjet Combustor Model

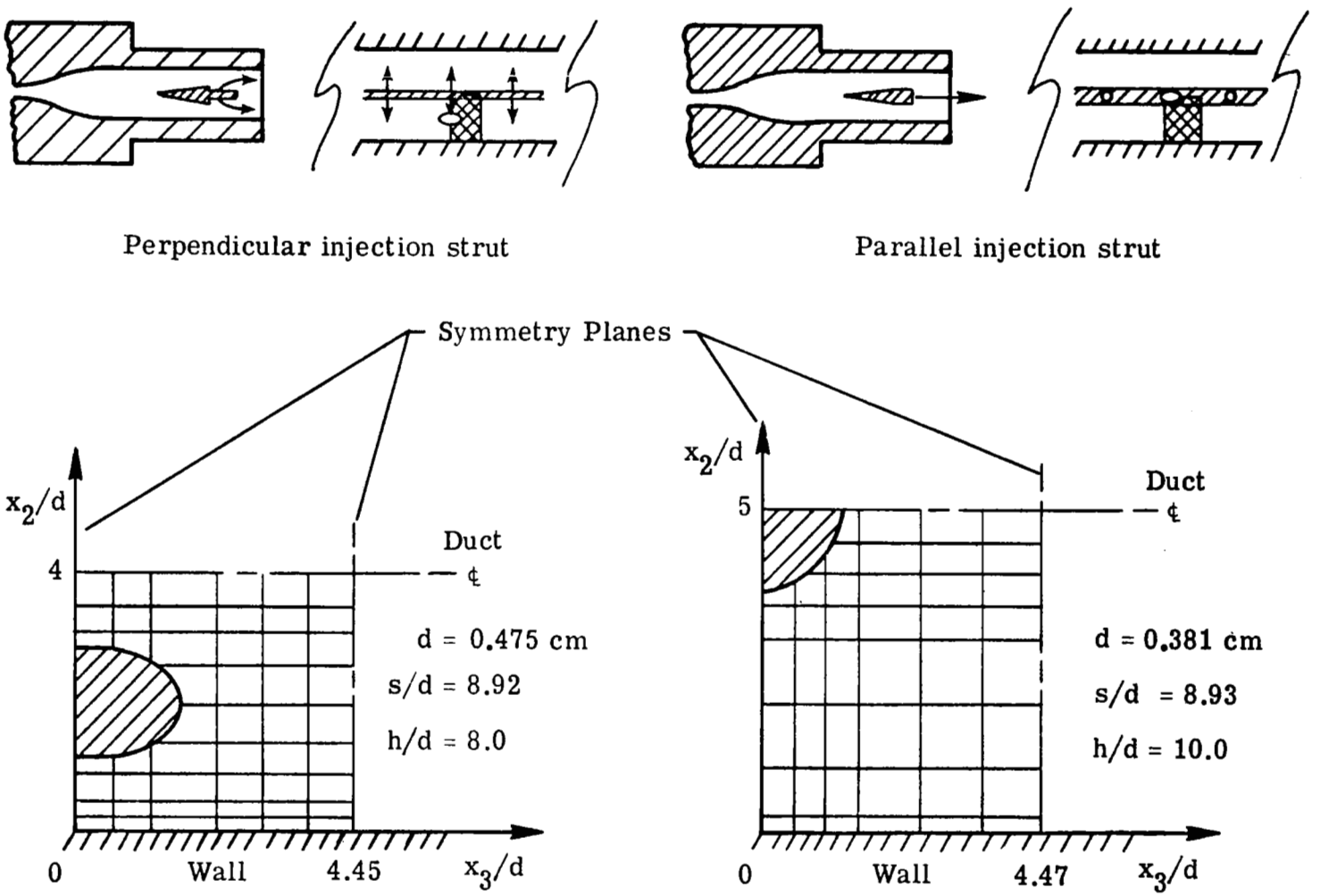

Figure 32. Two Fuel Injector Struts (Ref. 11) for Supersonic Combustion, with Virtual-Source Simulation

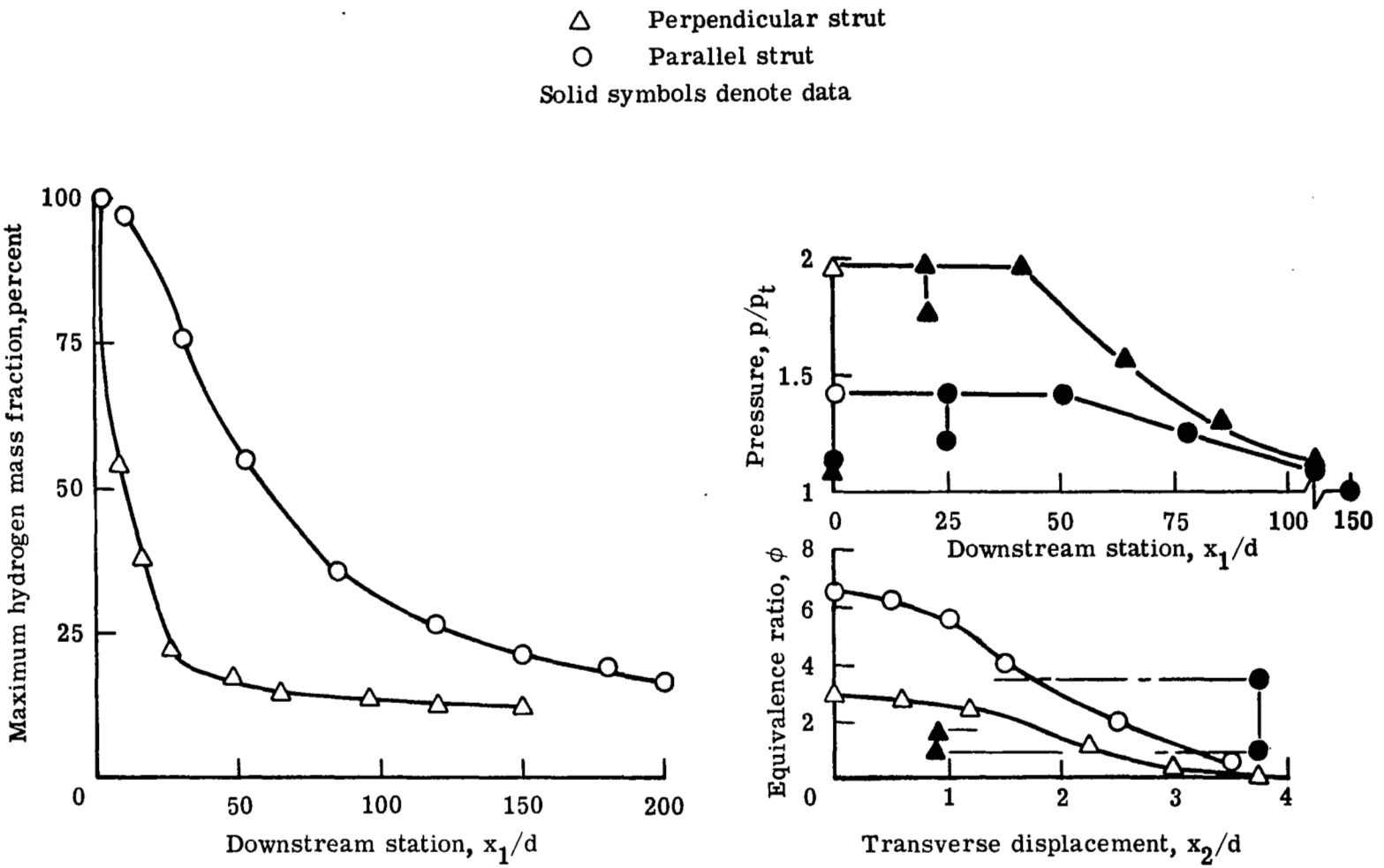

Figure 33. Analytical Evaluation of Two Supersonic Strut Injectors from Virtual-Source Simulation. $\eta = 3$; $\phi = 0.6$; s/d = 9